DE HAAGSE HOGESCHOOL

Nikhef

Characterizing the electrical and mechanical behavior of the Electro-Thermal Actuators of the Nikhef accelerometer MEMS design

Internship report

12-07-2017

Author:
Jerry Kamer (14059002)

Internship supervisor:
Dhr. E. Hennes

The Hague University Internship coordinator:
Dr. R. Buning

Preface

Nikhef is the Dutch national institute for Subatomic Physics. This institute is a collaboration of five universities and the Netherlands Organization for Scientific Research (NWO). Nikhef explores the world of elementary particles, the forces acting on them and tries to understand the structure of space and time. Nikhef focusses on particle- and astroparticle physics and is involved in three large experiments at the Large Hadron Collider (LHC) at CERN. And contributes to the construction, installation and operation of the detectors for neutrinos, dark matter particles and high energetic cosmic radiation. In addition, Nikhef is active in the research of gravitational waves with the Virgo detector.

First and foremost, I would like to express my gratitude to my supervisor Eric Hennes for providing me an opportunity to do my internship at Nikhef, always having an answer to my questions and making helpful, insightful comments.
Besides Eric, I would like to thank Boris Boom for making the photo processing module and destroying the Front ETA.
Last but not least, I would like to thank Berend Munneke for repairing the vacuum pump.

Abstract

The sensitivity of future gravitational wave detectors is limited by Newtonian noise between $2\ \mathrm{Hz}$ and $20\ \mathrm{Hz}$. Newtonian noise effects can be predicted by measuring seismic vibrations around the detector, using a grid of accelerometers. These accelerometers require a high sensitivity of $< 1\ \mathrm{ng}/\sqrt{\mathrm{Hz}}$ at the indicated frequencies. This can be achieved by tuning the accelerometer to a low resonance frequency. A low frequency, low cost accelerometer may be accomplished by using a MEMS (Micro Electro Mechanical System) accelerometer equipped with anti-spring technology.

Any accelerometer consists of a mass-spring oscillator. The displacement of the mass, due to seismic vibrations, is a measure for the frame acceleration. In the MEMS all mechanical parts are etched in its thin silicon device layer (the x,y-plane). The mass is suspended to the frame by four sets of curved cantilever springs, such that it oscillates in, say, the y-direction. By compressing these springs in the x-direction, the stiffness and, with it, the resonance frequency of the oscillator can be reduced, which is called the "Anti-spring effect". The compression is obtained from so-called Electro Thermal Actuator (ETA) beams. These V-shaped beams expand due to Joule heating, when a current is sent through them. The moving beam tip is pushing the spring into its designed compressed position. Its design should meet the required displacement and spring force.

In this project the electro-thermal and mechanical characteristics of the present ETAs are measured and modeled in order to get a better understanding of their behavior, which may help to improve future MEMS accelerometer designs. Both quasi-static and dynamic (pulsed) actuation of the ETAs delivered useful information for this goal.

Using an electro-thermal quasi-static numerical model, the resistivity of the highly boron doped silicon ($\sim 6 \cdot 10^{18}\ \mathrm{carriers/cm^3}$) as a function of temperature up to $1123\ \mathrm{K}$ is estimated, based on the measurement of the ETA resistance as a function of the electrical power in air. This estimation requires knowledge of the thermal conductivity of both silicon and air as a function of temperature, which were taken from literature. The resulting resistivity curve shows a peak at $971\ \mathrm{K}$, and fits well within corresponding curves for other doping levels, obtained from literature. The modeled and measured resistance in vacuum have a maximum difference of about $40\ \Omega$. From the voltage step response, thermal time constants in air and vacuum are obtained, which agreed and disagreed with the estimated thermal time constants respectively.

Quasi-static and dynamic actuation results in the tip displacement of both single and dual (parallel) actuated ETA systems as a function of applied power, both for unloaded and a range of increasing spring-loaded ETAs, up to the beam its plasticity and buckling limits. Below these limits the results match fairly well the analytical Thermo-mechanical model. The model requires knowledge of the Young's modulus and thermal expansion coefficient of silicon as a function of temperature, which were taken from literature. Several types of limiting behavior has been observed and understood: several buckling modes, plastic deformation and melting.

MEMS designers can benefit from this knowledge when optimizing the ETAs, anti-reverse system and pumping mechanism.

Several aspects of this report are promising and require further research.

List of symbols

Symbol	Description	Unit
$\Delta\phi_b$	Phase shift of the light beams	$-$
$\Delta\omega$	Angular bandwidth $= \frac{D_a}{m_a}$	s^{-1}
ΔL_ε	Beam expansion or compression	m
ΔL_m	Test mass displacement	m
ΔT	Temperature increase	K
α	Thermal expansion coefficient	K^{-1}
α_0	Chosen initial angle between horizontal and spring base	$-$
α_s	Correction factor for the spring curvature	$-$
δ	Tip displacement of the beam	m
ε	Strain	$-$
ε_b	Bending strain	$-$
ε_R	Emissivity of silicon	$-$
ε_s	Stretching strain	$-$
ε_T	Thermal strain	$-$
θ	Angle between horizontal and neutral beam axis	$-$
θ_0	Angle between horizontal and spring base	$-$
θ_R	Angle of the arc	$-$
$\theta(l)$	Angle between horizontal and spring along the l-axis	$-$
κ_0	Rotational spring constant	Nm
λ	Wavelength of the beam	m
ρ	Resistivity of silicon	$\Omega\mathrm{m}$
ρ_d	Silicon density	kgm^{-3}
σ	Stefan-Boltzmann constant	$\mathrm{Wm}^{-2}\mathrm{K}^{-4}$
τ	Thermal time constant	s
ϕ	Angle between spring base and tip	$-$
ω	Angular frequency	s^{-1}
ω_0	Natural angular frequency $= \sqrt{\frac{k_a}{m_a}} = 2\pi f_0$	s^{-1}
a	Acceleration	ms^{-2}
A	Surface area of the cross-section	m^2
A_p	Cross-section area of the added silicon piece	m^2
C_1, C_2	Differential constants	m
C_s	Specific heat of silicon	$\mathrm{Jkg}^{-1}\mathrm{K}^{-1}$
d_x	Spring compression distance	m
d_m	Molecule diameter	m
D_a	Damping constant of the accelerometer	kgs^{-1}
E	Young's modulus	Pa
f_0	Natural frequency	s^{-1}
F	Force	N

F_v	Vertically applied force on the beam	N
F_x	Horizontal force acting on the spring	N
F_y	Vertical force acting on the spring	N
$F_{y,0}$	Vertical force acting on the spring in uncompressed state	N
$F_{y,1}$	Vertical force acting on the spring in compressed state	N
F_{NN}	Force caused by Newtonian noise	N
g	Distance between beam and substrate	m
g_s	Gap size between the sub-beams	m
G	Gravitational constant	$\mathrm{Nm^2kg^{-2}}$
h	Beam height	m
h_s	Gravitational wave strain amplitude	$-$
I	Current	A
I_x	Second moment of area	$\mathrm{m^4}$
I_s	Source current	A
J	Current density	$\mathrm{Am^2}$
k	Eigenvalue $= \sqrt{\frac{P_0}{EI_x}}$	$\mathrm{m^{-1}}$
k_a	Spring constant of the accelerometer	$\mathrm{Nm^{-1}}$
k_{air}	Thermal conductivity of air	$\mathrm{Wm^{-1}K^{-1}}$
k_b	Beam stiffness	$\mathrm{Nm^{-1}}$
k_B	Boltzmann constant	$\mathrm{JK^{-1}}$
k_s	Thermal conductivity of silicon	$\mathrm{Wm^{-1}K^{-1}}$
k_y	Spring constant in the y-direction	$\mathrm{Nm^{-1}}$
$k_{y,0}$	Uncompressed spring constant in the y-direction	$\mathrm{Nm^{-1}}$
$k_{y,1}$	Compressed Spring constant in the y-direction	$\mathrm{Nm^{-1}}$
l_{mfp}	Mean free path	m
L	Half-span of the beam	m
L_ε	Initial beam length	m
L_b	Fixed-fixed beam length	m
L_i	Length of the interferometer arm	m
L_l	Total spring length	m
L_p	Length of the added silicon piece	m
L_R	Arc length of a circle	m
L_s	Horizontal length of the spring	m
$L(y)$	Arc length at y from the neutral axis	m
m	Mass	kg
m_a	Accelerometer mass	kg
m_s	Mass of ‘seismic motion particle’	kg
m_t	Mass of the test mass	kg
M_0	Moment acting on fixed beam end	Nm
M_L	Moment acting on the spring tip	Nm
M_s	Moment at spring base	Nm

$M(l)$	Moment along the l-axis	Nm
O	Effective surface area of beam segment	m^2
p	Pressure	Pa
P	Horizontally applied force on the beam	N
P_0	Inline force at fixed beam end	N
P_{ETA}	Power dissipated in the ETA	W
r	Distance between test mass and particle	m
R	Resistance	Ω
R_{back}	Resistance of Back ETA	Ω
$R_{c,n}$	Resistance of contact n	Ω
R_{ETA}	Resistance of an ETA	Ω
R_{front}	Resistance of Front ETA	Ω
R_p	Resistance of the added silicon piece	Ω
R_R	Radius of a circle	m
S	Shape conduction factor	–
$T(x)$	Temperature	K
T_0	Transversal force acting on fixed beam end	N
T_∞	Substrate temperature	K
T_n	Temperature at x_n	K
$u(x)$	Longitudinal displacement of the beam at x	m
U	Voltage	V
U_s	Source voltage	V
w	Beam width	m
w_1	Middle sub-beam width	m
w_a	Total ETA beam width	m
w_e	Effective ETA beam width	m
$w(x)$	Transversal displacement of the beam at x	m
x	x-coordinate along the x-axis	m
x_f	Frame displacement	m
$\hat{x}_f$	Complex amplitude of frame displacement	m
x_L	x-coordinate at the end of the l-axis	m
x_m	Mass displacement	m
x_{rel}	Relative mass displacement $= x_m - x_f$	m
$\hat{x}_{rel}$	Complex amplitude of relative mass displacement	m
$x(l)$	x-coordinate along the l-axis	m
y	Vertical distance from neutral beam axis	m
y_L	y-coordinate at the end of the l-axis	m
y_s	Vertical position of spring tip	m
$y(l)$	y-coordinate along the l-axis	m
z_1, z_2, z_c	Differential constants	K

Table of Contents

1 Introduction 1
1.1 Virgo 1
1.2 Effect of seismic motion on the detector signal 2
1.3 Nikhef MEMS accelerometer project 3
2 Theory, models and MEMS design 5
2.1 Accelerometer theory 5
2.2 Lay-out of the Nikhef MEMS design 6
2.3 Anti-spring theory and modeling 12
2.4 Electro-Thermal Actuator theory and modeling 15
2.5 Material properties 22
3 Measurement setup and methods 24
3.1 Quasi-static ETA resistance measurement 24
3.2 Pulsed ETA resistance measurement 26
3.3 ETA mechanical behavior measurement 27
3.4 Vacuum setup 28
4 Measurement results 30
4.1 Resistance measurements 30
4.2 Displacement measurements 37
4.3 Model comparison 41
5 Further observations 43
5.1 ETA beam vibration 43
5.2 Local buckling 43
5.3 Unactuated Back ETA displacement 44
5.4 ETA beam glowing 44
6 Conclusions 45
7 Discussion and suggestions 46
8 References 47
A Appendix: Derivations 50
B Appendix: Material properties 61
C Appendix: Thermal time constant estimation 66
D Appendix: Modeling parameters 69
E Appendix: Vacuum setup pictures 70
F Appendix: Shuttle locking pictures 71
G Appendix: Model operation 72

1 Introduction

The concept of gravitational waves has been proposed by Albert Einstein in 1916 [1], based on his theory of General Relativity. This theory describes gravity as a curvature of space-time. An asymmetric spinning mass or a binary system of masses creates a ripple of space-time, which propagates outwards into space as a wave, see figure 1.

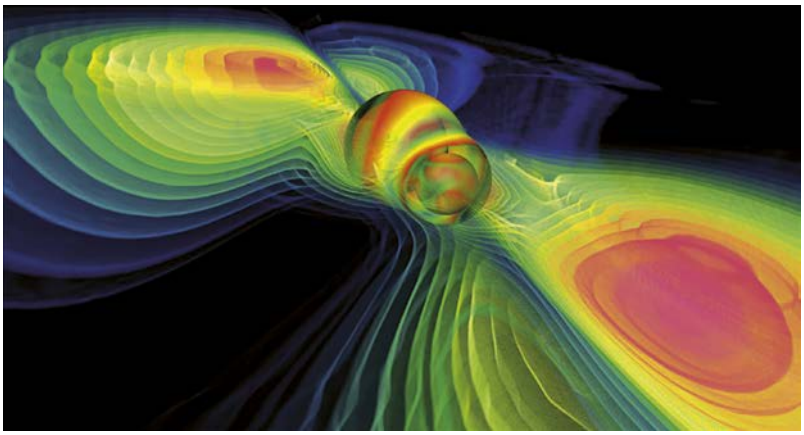

Figure 1. Computer simulation of the gravitational waves caused by a collision of two black holes. [2]

This wave can curve space-time, altering the gravity, hence the name gravitational wave. The amplitude of gravitational waves depends on the strength of the 'source' and the distance traveled by the wave. Rotation speed, mass, degree of asymmetry and mutual distance (binary system) determine the strength of the 'source'. As the gravitational wave travels through space-time, the amplitude decreases linearly with the traveled distance. On 14 September 2015 [3] the first gravitational wave has been detected. This date marks the start of gravitational wave astronomy, enabling us to observe gravitational phenomena in the universe, including black holes and events form the early universe, beyond the cosmic background radiation limit.

1.1 Virgo

Virgo is one of the existing gravitational wave detectors. It is essentially a Michelson interferometer with two long arms of three kilometer each, sited in Italy, near Pisa, see figure 2.

Figure 2. Left: Aerial view of the Virgo interferometer. [4] Right: Schematic of the Virgo interferometer. [5]

In a Michelson interferometer a laser beam is split by a beam splitter into two beams. The two beams both reflect back, on so-called test mass mirrors, to the beam splitter. Both beams are split back into the laser and into the photodiode. The photodiode measures the intensity of the incident

beam. If one (or both) of the test mass mirrors has a displacement ΔL_m, there will be an optical path difference between the beams, ensuring a phase difference. As the beams interfere with a phase difference, the intensity of the incident beam will become less. This is a measure for the difference in distance traveled by the two light beams. On top of a standard Michelson interferometer does the one used by Virgo contain a so-called input mirror in every arm and a recycling mirror. The input mirror reflects some of the photons in an arm back to the test mass mirrors. This ensures that a photon receives a bigger phase difference, for it travels the same distance several times in this cavity. The optical length of the arms is extended to $100\ \mathrm{km}$ [5], when using the input mirrors. The recycling mirror sends the beam that is split, from the beam splitter, into the laser back to the beam splitter. Adding the input and recycling mirrors can increase the power of the beams in the cavity up to $50\ \mathrm{kW}$.

The phase difference is given by:

$$\Delta\phi = \frac{8\pi \cdot \Delta L_m}{\lambda} \tag{1.1}$$

Where ΔL_m is the relative displacement of the two test masses, $\frac{\Delta L_{m,1} - \Delta L_{m,2}}{2}$ and λ the wavelength of the beam. Gravitational waves cause a relative displacement of the test masses. For a given gravitational wave strain amplitude, h_s, the resulting displacement is:

$$\Delta L_m = \frac{h_s \cdot L_i}{2} \tag{1.2}$$

Where L_i is the arm length of the interferometer. The expected strains are in the order of 10^{-22}. This means Virgo must be able to measure a displacement of $\Delta L_m \approx 10^{-19}\ \mathrm{m}$. Substituting formula (1.2) in (1.1) gives an expression for the phase difference and the strain caused by the gravitational wave:

$$\Delta\phi = \left(\frac{4\pi \cdot L_i}{\lambda}\right) \cdot h_s \tag{1.3}$$

In 2011 the upgrade of the Virgo detector started. The new “Advanced Virgo” will be ten times more sensitive than Virgo, giving it the opportunity to measure strains in the order of 10^{-23}. This would mean that gravitational waves with lower amplitudes can be measured, thus extending the reach of the detector. A bigger reach provides more detectable events and data to be obtained.

1.2 Effect of seismic motion on the detector signal

For an accurate measurement of gravitational waves, the test masses must be suspended in such a way that they do not move. Because the strains that will be measured by Advanced Virgo are in the order of 10^{-23}, even the smallest seismic motion would have a huge negative effect on the accuracy of the measurement, this is called seismic noise. To reduce the seismic noise, mechanical filters are used that attenuate the seismic noise for frequencies above a few Hz. Therefore, the test masses will not move by direct mechanical interaction with the ground.
Besides seismic noise, seismic motion also creates another type of noise called Newtonian noise. This noise is caused by the gravitational attraction between masses, given by Newton’s law of gravitation:

$$F_{NN} = G \cdot \frac{m_s \cdot m_t}{r^2} \tag{1.4}$$

Where m_s is the mass of a 'seismic motion particle', m_t is the mirror mass, r the distance between them. When a seismic wave passes the test mass, it will swing due to the attraction of the particles coming closer to the test mass, see figure 3.

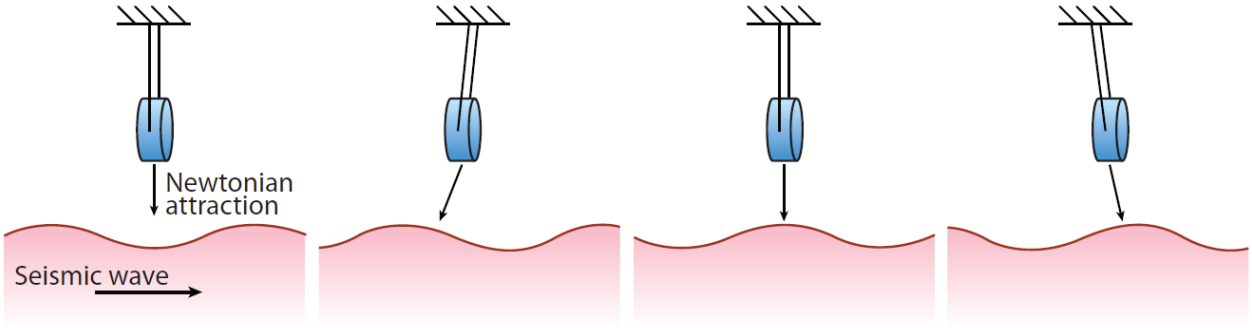

Figure 3. Illustration of the Newtonian noise effect on a test mass when a seismic wave passes by. [6]

The swing of the test mass suggests that a gravitational wave is measured, though this is not the case.
The sensitivity of the Virgo detector is too low to be effected by the Newtonian noise but, Advanced Virgo has a higher sensitivity, and Newtonian noise is expected to have effect on the detector signal during bad weather conditions. The sensitivity curve of Advanced Virgo is presented in figure 4. It shows that at high seismic activity the sensitivity of Advanced Virgo will be limited by Newtonian noise, between 2 Hz and 20 Hz.

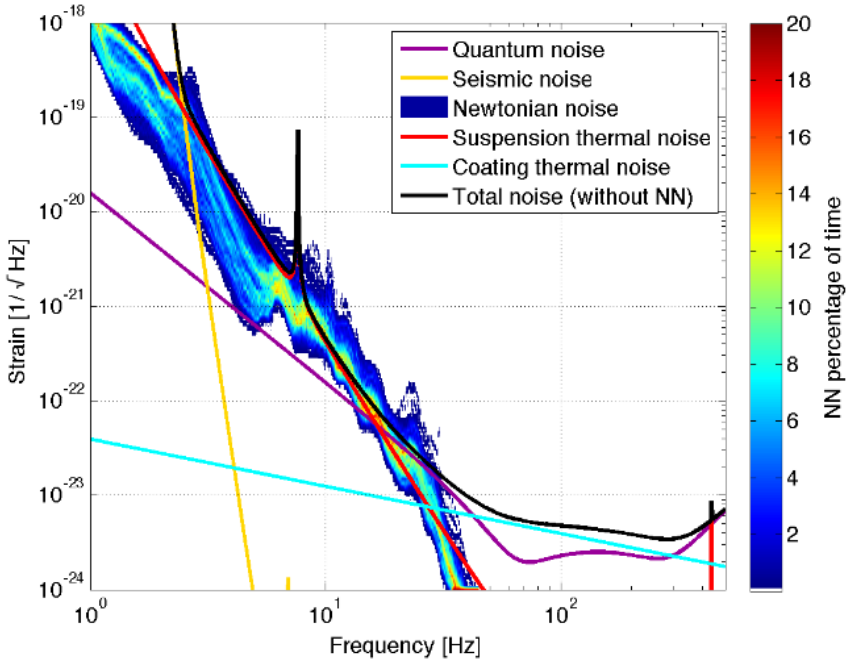

Figure 4. The estimated noise for Advanced Virgo. At high seismic activity will the sensitivity of Advanced Virgo be limited by the Newtonian noise. [6]

1.3 Nikhef MEMS accelerometer project

To tackle the Newtonian noise problem of Advanced Virgo, a large grid of accelerometers could be placed around the interferometer. The seismic data retrieved from these accelerometers can be used to predict the Newtonian noise effect on the gravitational wave measurement, and correct for it, such that this noise effect is decently cancelled. This requires the accelerometers to be sensitive at

low frequency ($2\ \mathrm{Hz}$ - $20\ \mathrm{Hz}$). Because a large number of accelerometers is required they need to be low in price.
A Micro Electro Mechanical System (MEMS) accelerometer may be a valuable option. This is an accelerometer on a silicon chip of a few millimeters in size. These accelerometers require a high sensitivity of $< 1\ \mathrm{ng}/\sqrt{\mathrm{Hz}}$ at the indicated frequencies. To achieve this sensitivity, the accelerometer requires a low-frequent, low-damped mass-spring system. This is achieved by including negative stiffness in the system and by operating it in vacuum. The negative stiffness is obtained using so-called Anti-spring technology. In the MEMS all mechanical parts are etched in its thin silicon device layer (the x-y plane). The mass is suspended to the frame by four sets of curved cantilever springs, such that it oscillates in, the y-direction. By compressing these springs in the x- direction, the stiffness and, with it, the resonance frequency of the oscillator can be reduced, which is called the “Anti-spring effect”. For the Anti-spring effect to work, the springs must be compressed. The compression is obtained from so-called Electro Thermal Actuator (ETA) beams, the subject of this report.

For the next generation MEMS designs, is it desirable to know the electro-thermal and mechanical characteristics of the ETAs on the present MEMS accelerometer chips, both at atmospheric pressure and in vacuum, for a better understanding of their behavior, which may help to improve future MEMS accelerometer designs. The electrical characteristics can be determined by measuring the resistance of the ETA, because it is a measure for the ratio of the voltage and current and, moreover, is the best measure for the temperature of the ETA. The resistance will be plotted as a function of power, for this also is a measure for the ratio of the voltage and current and the ETA displacement is connected to the dissipated power. The mechanical characteristics are determined by measuring the displacement of the ETA by certain amounts dissipated power and establishing the buckling behavior. These measurements will show the (maximum) capabilities of the ETA. This information could help improve the design of new compression systems.

2 Theory, models and MEMS design

This chapter will describe the mathematical representation of an accelerometer response. Furthermore, will this chapter show two Nikhef MEMS designs, which are used in the measurements. Finally, a short derivation of the used models for estimation and comparison is included in this chapter, together with some properties of silicon used in the models.

2.1 Accelerometer theory

An accelerometer consists of a mass suspended to a frame, by a spring or set of springs, and a sensor which measures their relative displacement. If the frame gets accelerated, the mass will be delayed in accelerating due to its inertia. The delay causes a relative displacement between the mass and the frame, which is a measure of the acceleration of the frame below the resonance frequency. An accelerometer can be modelled by a mass m_a, with a viscous damper D_a, which is attached to a frame by a spring with stiffness k_a, see figure 5.

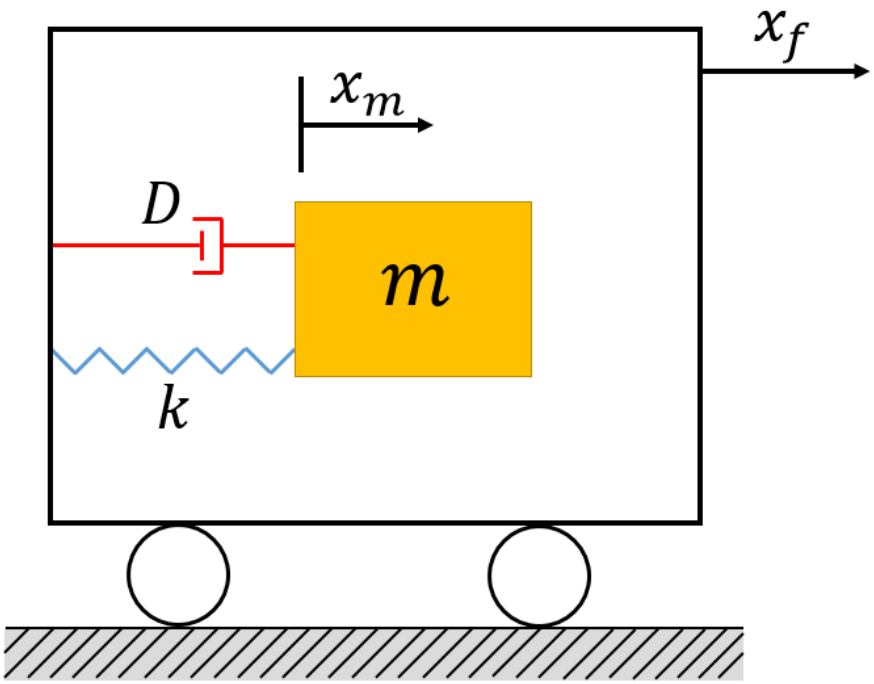

Figure 5. Schematic representation of an accelerometer.

This mass can be moved by the acceleration of the frame. The relative displacement x_{rel} of the mass can be described as the displacement of the frame x_f subtracted from the displacement of the mass x_m: $x_{rel} = x_m - x_f$. A mathematical description can be set up by summing all the forces acting upon the mass:

$$m_a \ddot{x}_m = -k_a x_{rel} - D_a \dot{x}_{rel} \tag{2.1}$$

This is just the equation of motion of the mass. For a harmonic motion, $x = \hat{x} \cdot e^{i\omega t}$, it can be solved giving the transfer function:

$$\left|\frac{\hat{x}_{rel}}{\hat{\ddot{x}}_f}\right| = \frac{1}{\omega_0^2} \cdot \frac{1}{\sqrt{\left(1-\frac{\omega^2}{\omega_0^2}\right)^2 + \left(\frac{\omega \cdot \Delta\omega}{\omega_0^2}\right)^2}} \tag{2.2}$$

Where ω_0 and $\Delta\omega$ are the natural angular frequency and angular bandwidth respectively and $\hat{x}_{rel}$ and $\hat{\ddot{x}}_f$ the complex relative displacement amplitude and the complex frame acceleration amplitude respectively. The angular bandwidth is the interval between the intersection at $\frac{1}{\sqrt{2}}$ under the resonance peak. The derivation of equation (2.2) can be found in appendix A.1

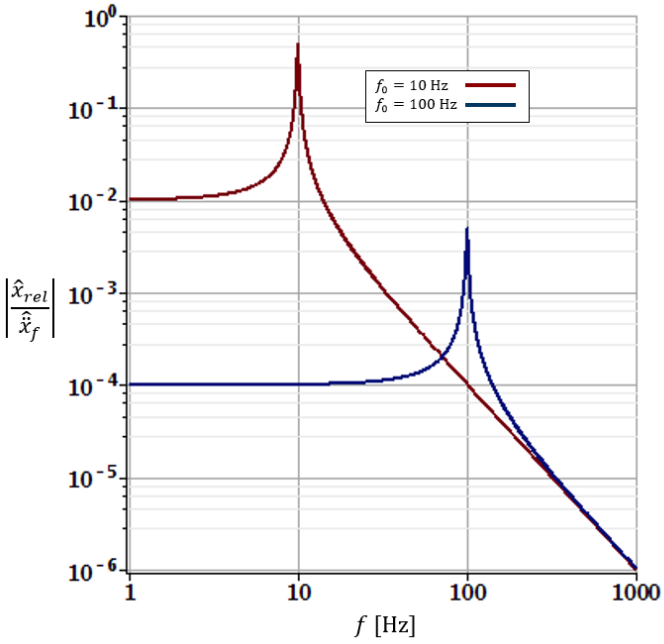

Figure 6. Illustration of the response of the accelerometer at $f_0 = 10$ Hz and $f_0 = 100$ Hz, with $\Delta\omega = 0{,}01$ Hz. The response for $f < f_0$ increases with $\frac{1}{{f_0}^2}$.

The sensitivity is dependent on the natural frequency of the mass-spring system, as illustrated by equation (2.2). If the natural frequency decreases, the sensitivity will become higher for all frequencies below the natural frequency, as shown in figure 6.

2.2 Lay-out of the Nikhef MEMS design

Nikhef has chosen to make the accelerometers on MEMS chips, which are relatively cheap and can be made quite accurate and fast. Two MEMS accelerometer designs are available, each with different ETA actuation possibilities. The Nikhef MEMS design has a flat square mass that is suspended to the frame by four sets springs, each on every corner. The relative displacement of the mass is measured with sensing comb capacitors pairs.

The Nikhef accelerometer MEMS devices are etched out of Silicon-on-Insulator (SOI) wafers, at MESA+. This wafer consists of a silicon substrate (or handle) wafer of 400 µm and a silicon device layer wafer of 50 µm with between them a layer of silicon oxide (BOX layer) of 4 µm. The silicon wafer is highly doped ($\sim 6 \cdot 10^{18}$ carriers/cm^3 [7]) with Boron (p-type), which makes the silicon a conductor. All the structures present in the MEMS design are etched out of the device layer. The silicon oxide layer beneath the device layer is removed underneath the structures that are intended to move. These structures have a perforated design, so the etching fluid can reach all the silicon oxide. Structures that are designed to be stuck to the substrate layer (anchored), will not contain the

perforation. The mass is etched out of all the three layers, such that at the end of the etching process the mass is only suspended by the springs. A schematic of the cross section of the accelerometer MEMS is shown in figure 7.

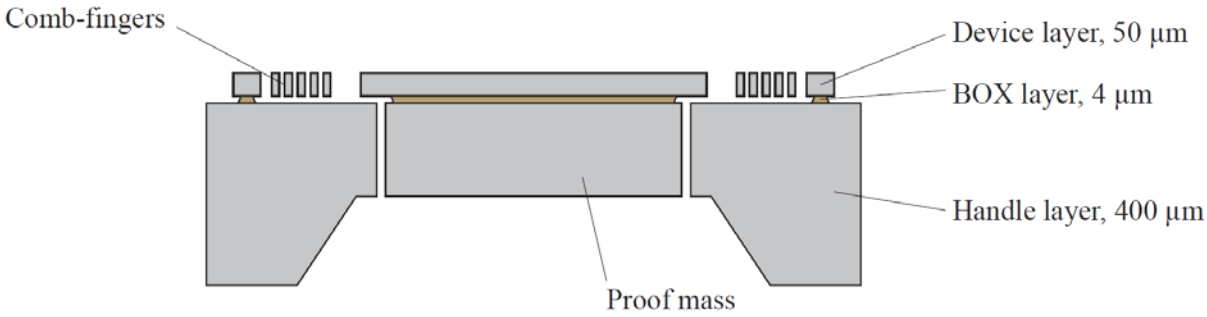

Figure 7. Schematic cross-sectional view of the accelerometer design. [8]

2.2.1 G1.4 MEMS design

The G1.4 MEMS design consist of a mass of 30 mg, suspended by 16 curved cantilever springs (four on each corner). Each of these spring have a total length of 1762,53 µm, a width of 8,66 µm and are designed to have an arc angle of 1 rad. A schematic of the complete G1.4 MEMS design is shown in figure 8. The quadrants are indicated with a 'Q' followed by a number.

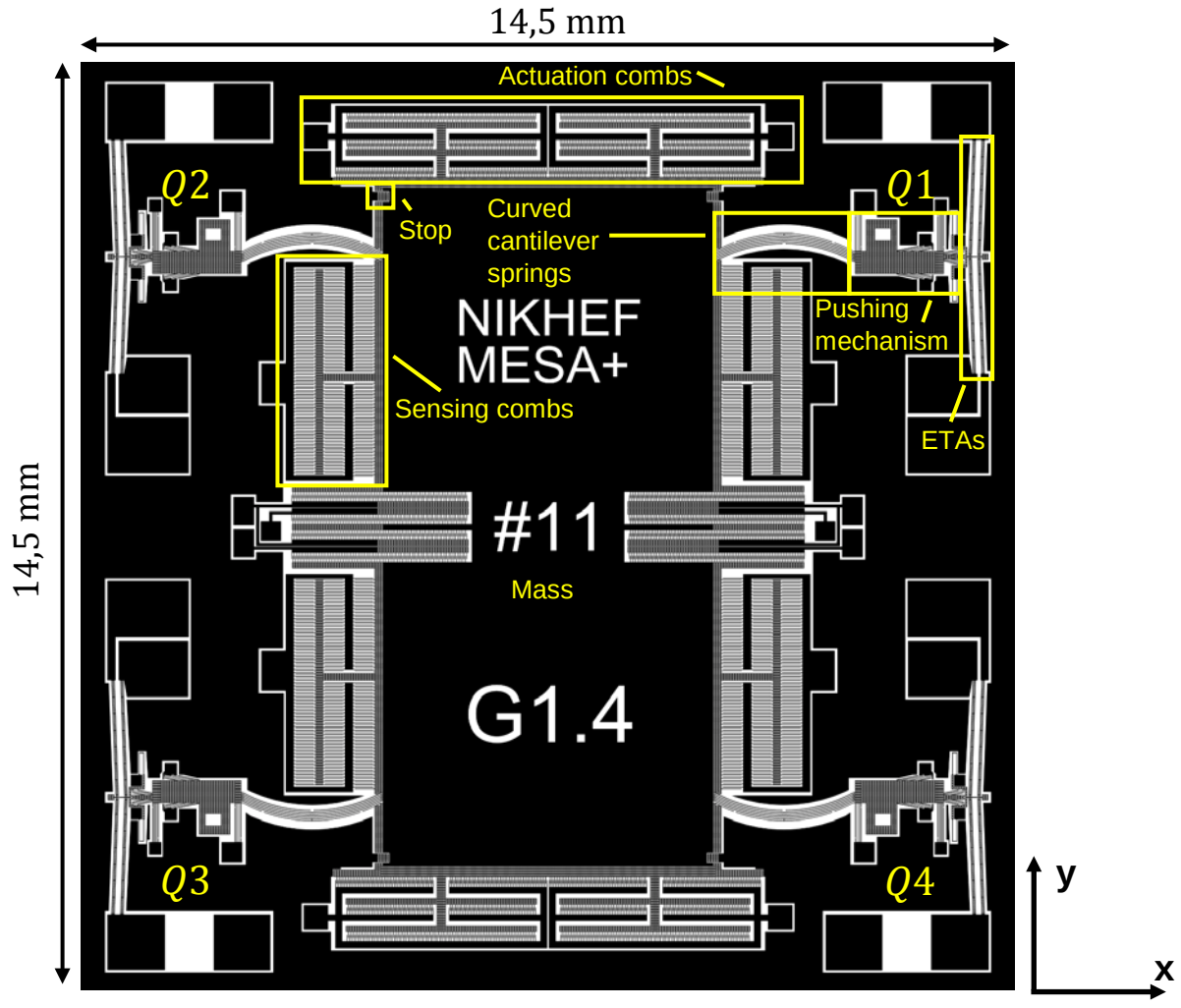

Figure 8. Schematic of the G1.4 MEMS design.

The mass position can be readout using sensing capacitor comb pairs. The sensing combs, shown in figure 9, are variable gap capacitors, which measure the mass displacement in the y-direction. Any mass displacement will change the distance between each pair of opposing comb fingers, causing a change in capacitance, which is measured continuously.

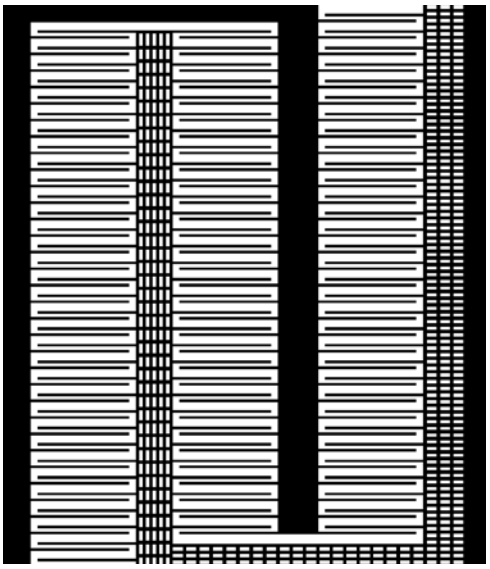

Figure 9. Schematic of the upper half of the sensing combs on the top left side of the mass.

The actuation combs can be used to apply a force on the mass in y-direction. The variable area actuation combs are shown in figure 10. By applying a DC voltage over the actuation combs, the two opposing combs attract each other, with a force proportional to the square of the voltage. One of the actuation combs is attached to the mass and the other to the substrate, so a force will act on the mass when the actuation combs are actuated.

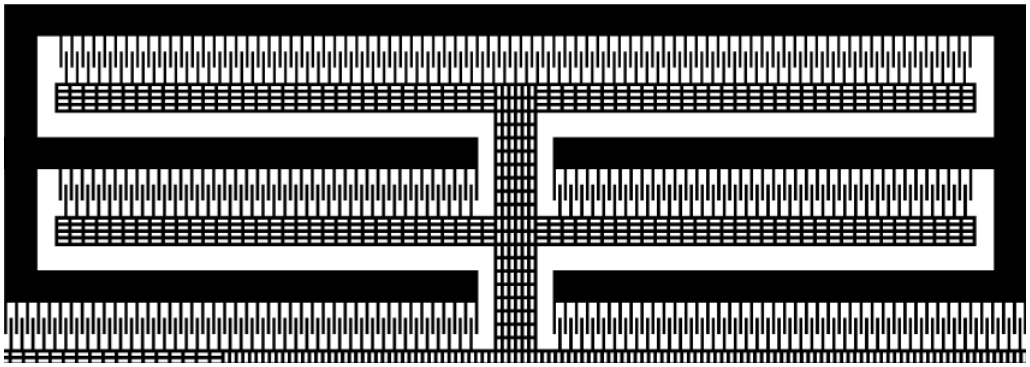

Figure 10. Schematic of the left half of the actuation combs on the upper side of the mass.

To prevent the capacitor combs from sticking together by Van der Waals bonding, the mass has been limited in its maximum displacement, both x- and y-direction. This limitation is achieved by the use of so-called stops, see figure 11. The stops restrict the in-plane displacement of the mass to $4\ \mu\mathrm{m}$, such that the capacitor combs will not touch each other. The stops are designed with the smallest possible contact area, so the mass will not stick to the stops by Van der Waals bonding.

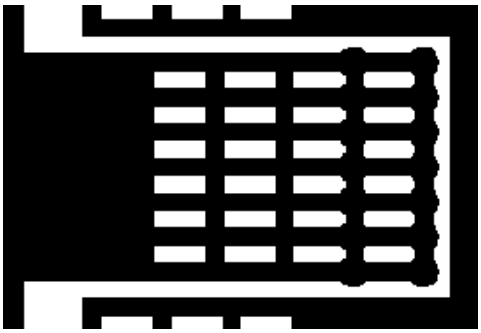

Figure 11. Schematic of a stop at the top left corner.

The Shuttle, shown in figure 12, is connected to the curved cantilever springs. Manually, the Shuttle can be moved in the direction of the springs, using a small needle in the hole in the Shuttle. This compresses the springs, which subsequently function as Anti-springs.

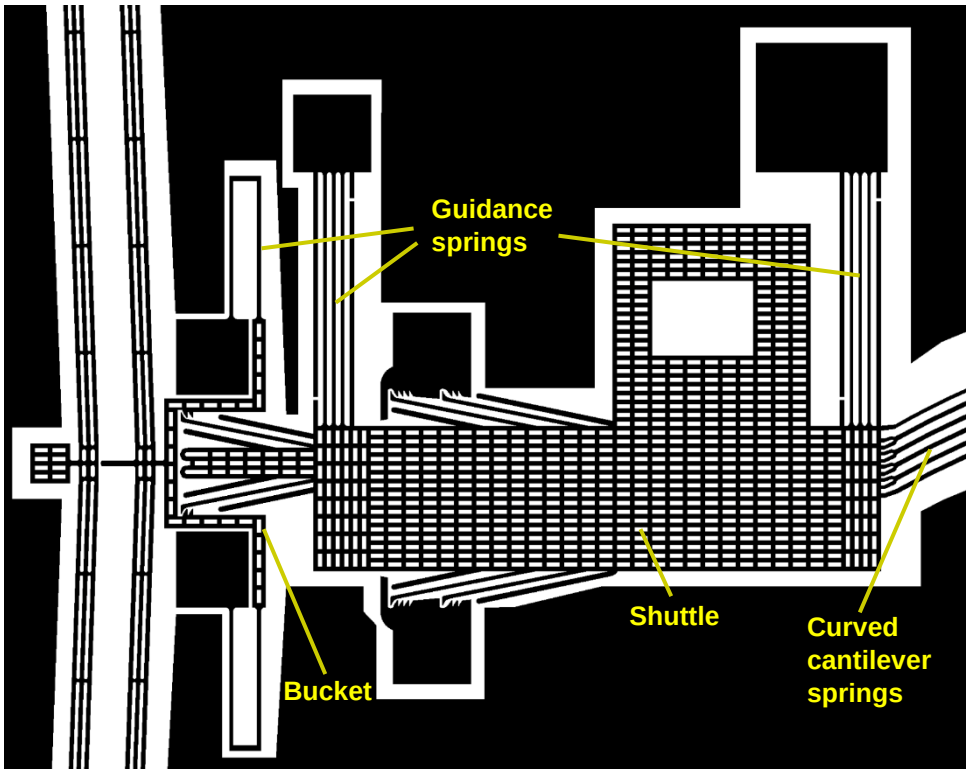

Figure 12. Schematic of the G1.4 pushing mechanism.

The Anti-spring effect only lasts if the springs stay in their compressed state. In order to maintain the compressed state, an anti-reverse system is implemented in the pushing mechanism, see figure 13. If a hook, connected to the shuttle, passes a tooth during the movement of the Shuttle, it cannot go back over the tooth, due to the shape of the tooth. This prevents the shuttle from going back to its initial state, thus keeping the spring compressed. The anti-reverse system has five teeth, so a maximum of five locked spring compressions can be achieved, see appendix F for all Shuttle locks. When the Shuttle is in its fifth lock, the springs are compress about $35\ \mu m$. The forces required for each Shuttle lock are shown in figure 16.

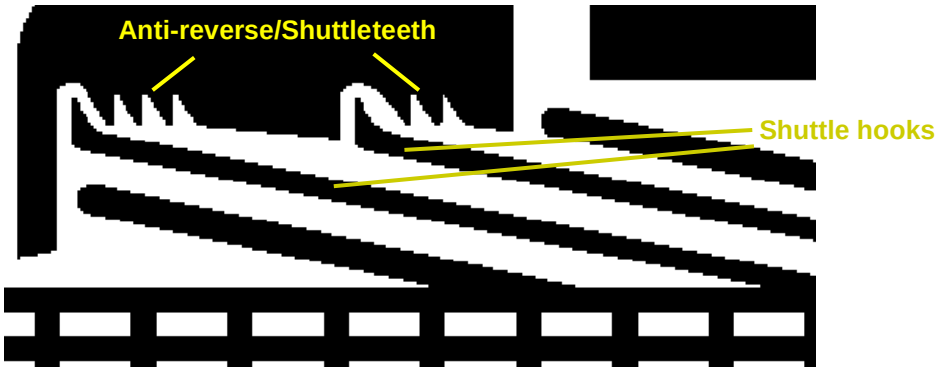

Figure 13. Schematic of the anti-reverse system.

The final MEMS design will be in vacuum and produced in great numbers, so it is impossible to manually compress all the curved cantilever springs. Therefore, two V-shaped ETAs are used to compress the curved cantilever springs, see figure 14, which can be actuated separately. Actuation of the ETAs is done by applying a current through the beam. Due to the current the ETA heats up, causing it to expand and compress the springs. The ETAs consist of three $2{,}9\ \mathrm{mm}$ long sub-beams placed under an angle of 2°. These beams are connected with perpendicular placed reinforcing beams. The three sub-beams combined, including perforation, give the ETA a width of $38{,}1\ \mu\mathrm{m}$. The reinforcing beams prevent buckling of the sub-beam, enabling a stronger actuation force. The ETA closest to the mass, the so-called Front ETA, is connected to the Bucket, see figure 15, of the pushing mechanism of the MEMS. Behind the Front ETA is the so-called Back ETA. The Back ETA helps the Front ETA push the shuttle, so the Front ETA is less likely to buckle because force is divided over two ETAs. If the Back ETA expands it touches the protrusion of the Front ETA, see figure 14, thus pushing the Front ETA towards the shuttle.

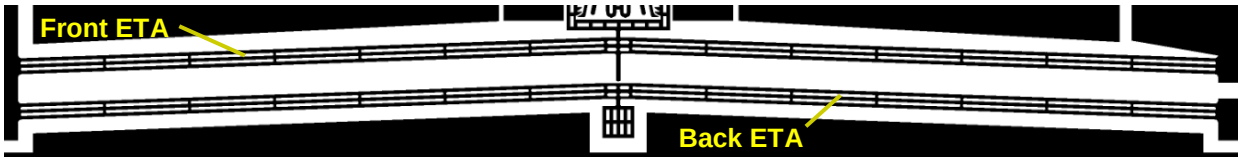

Figure 14. Schematic of the G1.4 thermal actuators.

Due to the force of the springs acting on the ETA and the thermal limit of silicon, the ETAs have a maximum displacement which they are capable to reach. Unfortunately, the fifth anti-reverse tooth cannot be reached by the maximum ETA displacement. To reach it, a pumping mechanism is implemented in the pushing mechanism, see figure 15.

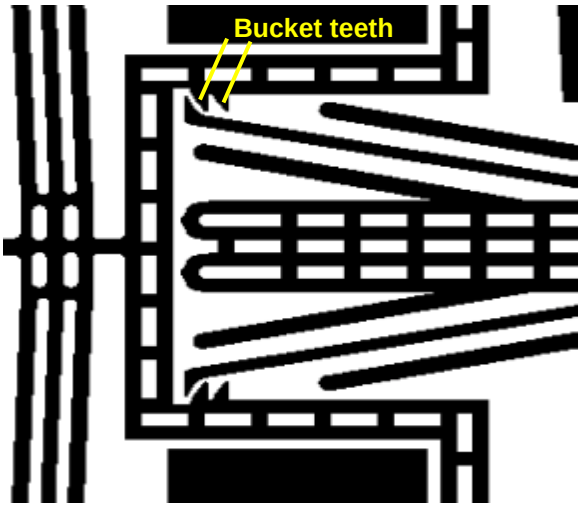

Figure 15. Schematic of the pumping mechanism.

When the first anti-reverse tooth of the Shuttle is reached, it will stay at that position (first locked shuttle state), even when the Front ETA is deactivated. The Front ETA is connected to the bucket, so when the Front ETA relaxes it withdraws the bucket. During this withdraw, the shuttle hook will pass the first Bucket tooth. When the Front ETA is actuated again, the bucket will now push the shuttle using the first tooth rather than the bucket side. Therefore, the shuttle can be pushed further for the same Front ETA expansion. The pumping mechanism has two teeth. The first bucket tooth is locked after the first Shuttle state is reached, the second bucket tooth is locked after the third Shuttle state is reached.

The guidance and curved cantilever springs apply a force to an expanding Front ETA, due to the stiffness of the springs. The stiffness of the curved cantilever springs can be modeled using the spring profile model (see chapter 2.3 and appendix G.1). The fixed-fixed beam stiffness formula can be used for estimating the stiffness of the guidance springs:

$$k_b = \frac{12EI_x}{{L_b}^3} \tag{2.3}$$

Where E is the Young's modulus, I_x the second moment of area and L_b the fixed-fixed beam length.

The Shuttle guidance springs consist of, in total, six parallel fixed-fixed beams with $L_b = 490$ µm and $w = 6$ µm per spring. This means that equation (2.3) needs to be multiplied by 6 to estimate the total stiffness of the Shuttle guidance springs. The two Bucket guidance springs are two fixed-fixed beams in series with $L_b = 277$ µm and $w = 7$ µm per spring. This reduces the stiffness of the springs by a factor 2, meaning equation (2.3) needs to be dived by 2 to estimate the stiffness of one Bucket guidance spring. The total Bucket guidance spring stiffness is 2 times equation (2.3) divided by 2. Knowing the stiffness of the present springs, the load lines (force that is needed for a certain displacement) of the five Shuttle locks can be estimated. The Electro-thermal (see chapter 2.4.1 and appendix G.2) and Thermo-mechanical model (see chapter 2.4.2 and appendix G.3) can give an estimation of the loaded ETA tip displacement at a certain electric power. The load lines and loaded tip displacements are presented in figure 16. For example, if a curved cantilever spring compression of 17 µm is required in Shuttle lock 0 (blue solid line), an electrical power of 499 mW (pink dashed line) needs to be applied to the ETA, for at that point the force applied on and delivered by the ETA is the same.

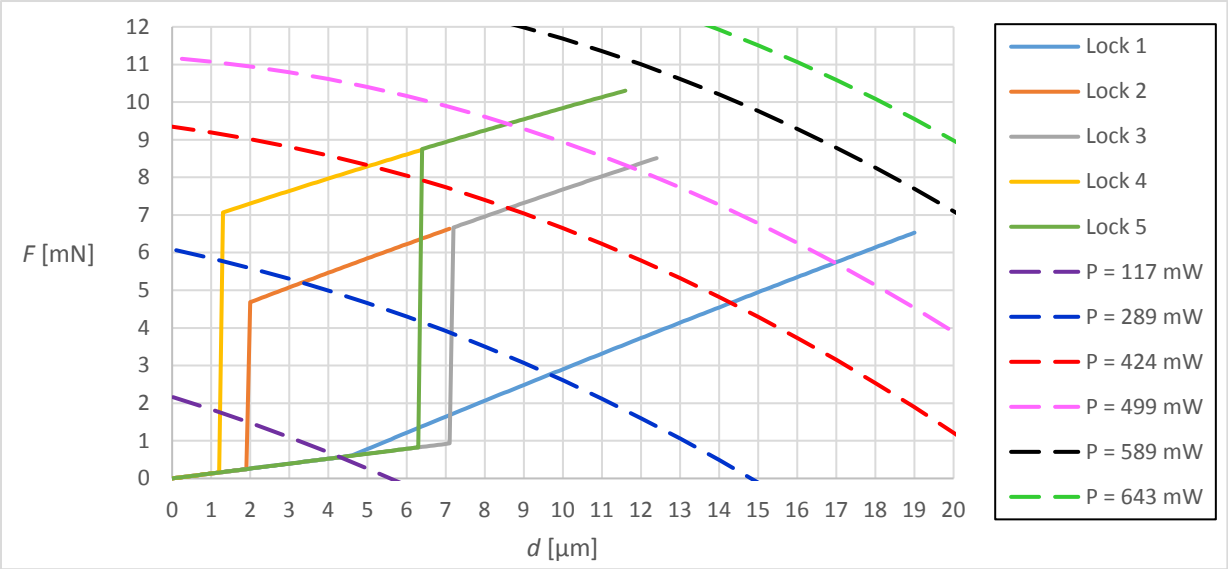

Figure 16. Load lines of the five Shuttle locks accompanied with the loaded tip displacements of a single ETA, at atmospheric pressure. The vertical rises of the solid lines are the point where the Bucket touches the Shuttle. The end of the solid lines is the point where the Shuttle is in the lock shown in the legend.

2.2.2 G1.5 MEMS design

The principle of the G1.5 MEMS design is the same as the G1.4: a centered mass of 10 mg is suspended by 16 curved cantilever beams, which can be compressed by V-shaped ETAs, lowering the spring constant in the y-direction. The biggest differences between the G1.5 MEMS design and the G1.4 MEMS design are: the size and the number of capacitor combs, the shape of the mass, the shape of the stops and the combined ETA actuation. In the G1.5 MEMS design both ETAs are connected to the same bonding pads. Therefore, they cannot be actuated separately.

2.3 Anti-spring theory and modeling

The accelerometer MEMS is designed to measure low frequency (2 – 20 Hz) seismic noise so, the sensitivity must be as high as possible for low frequencies. As shown by equation (2.2), this can be done by lowering the natural angular frequency, $\omega_0 = \sqrt{\frac{k}{m}}$, namely by decreasing the spring constant and/or increasing the mass. The mass is limited by the size of the MEMS chip, so it is tried to lower the spring constant of the system with Anti-springs, see figure 17.

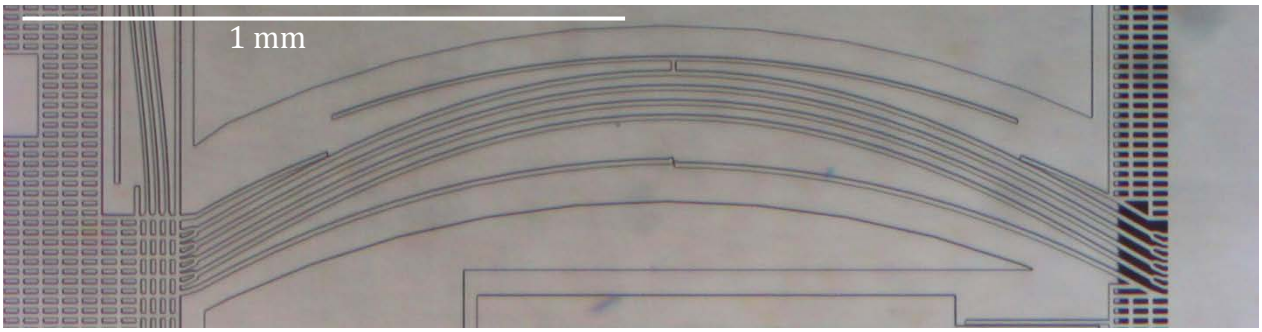

Figure 17. Microscope picture of the curved cantilever beam springs used in the G1.4 accelerometer MEMS with the Shuttle on the left side and the mass on the right side.

Figure 18 shows a sketch of the forces and moment acting on a single curved cantilever spring, both uncompressed and compressed. This sketch will be used for deriving a formula to show the working principle of the Anti-springs.

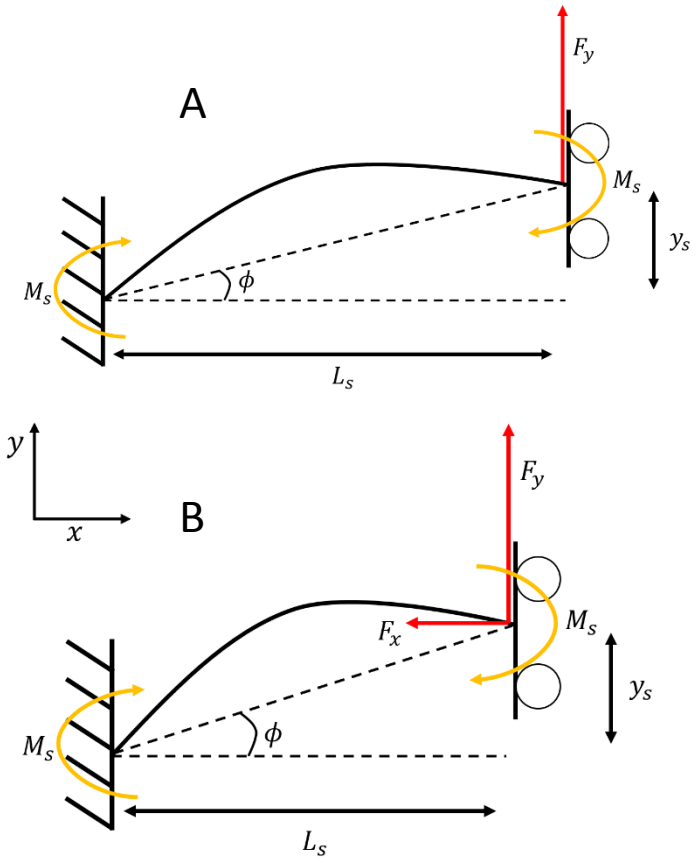

Figure 18. A single curved cantilever spring with forces and moments acting upon it.. A: the initial, uncompressed state of the spring. B: the compressed state of the spring.

The spring constant in the y-direction, k_y, of the curved cantilever spring is:

$$k_y = \frac{F_y}{y_s} \approx \frac{12EI_x}{{L_s}^3} \tag{2.4}$$

Where F_y is the vertical force acting the spring, y_s the vertical position of the spring tip and L_s the horizontal length of the spring. The sum of the forces and moments acting on the spring base for an uncompressed spring is:

$$2M_s - F_{y,0}L_s = 0 \tag{2.5}$$

Where M_s is the moment acting on the spring base and tip and $F_{y,0}$ the vertical force acting on the spring in the uncompressed state. The spring bending due to the moments acting on the spring is inhibited by the rotational stiffness, κ_0, at the clamping of the spring, for the spring base holds:

$$\kappa_0 = \frac{M_s}{\phi} \tag{2.6}$$

Where ϕ the angle between spring base and tip. For small angles holds that $\phi \approx \frac{y_s}{L_s}$, combining this with the substitution of equation (2.4) and (2.5) in (2.6) gives:

$$\kappa_0 = k_{y,0}{L_s}^2 \approx \frac{6EI_x}{L_s} \tag{2.7}$$

Where $k_{y,0}$ is the uncompressed spring constant in the y-direction. Equation (2.7) shows that for very small spring compressions the rotational stiffness barely changes and therefore the moments will not change. If the curved cantilever is compressed in the x-direction direction, by a horizontal force, F_x, The sum of the forces and moments acting on the spring base for a compressed spring is:

$$2M_s - F_{y,1}L_s - F_x y_s = 0 \tag{2.8}$$

Where $F_{y,1}$ is the vertical force acting on the spring in compressed state. Substituting equation (2.6) and (2.7) in (2.8) gives:

$$k_{y,0}{L_s}^2 = \frac{F_{y,1}{L_s}^2}{y_s} + F_x L_s \tag{2.9}$$

Rewriting equation (2.9) gives an expression for the compressed spring constant, $k_{y,1}$:

$$k_{y,1} = k_{y,0} - \frac{F_x}{L_s} \tag{2.10}$$

Equation (2.10) shows that the spring constant in the y-direction of a curved cantilever spring can be decreased by applying a compression in the x-direction.

Equation (2.10) does not tell us what spring compression distance, d_x, is needed to reach the required horizontal compression force, F_x. d_x depends on the springs initial curvature. The precise description of the deformed profile of the spring can be set up by considering the balance of moments in every point l along the spring, where l is the curvilinear coordinate, running from the spring base ($l = 0$) to the tip ($l = L_l$), see figure 19:

$$M(l) = -F_y \cdot \big(x_L - x(l)\big) + F_x \cdot \big(y_L - y(l)\big) - M_L \tag{2.11}$$

Where $M(l)$ is the moment along the l-axis, x_L and y_L are the x-coordinate and y-coordinate, respectively, at $l = L_l$, $x(l)$ and $y(l)$ are the x-coordinate and y-coordinate, respectively, along the l-axis and M_L the moment acting on the spring tip.

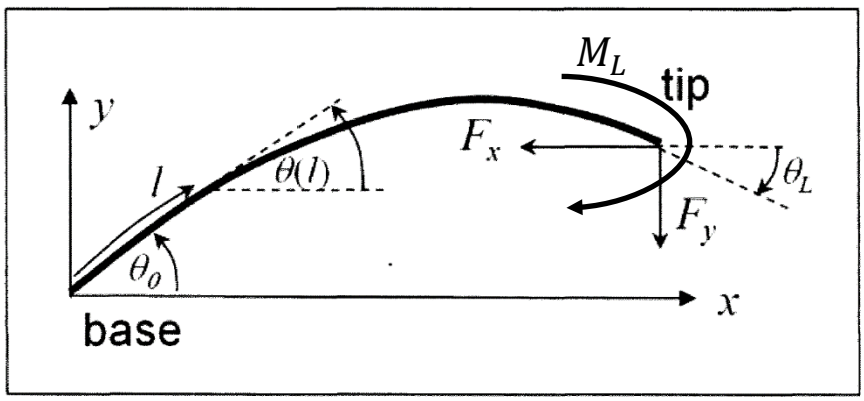

Figure 19. Schematic of a curved cantilever spring. [9]

Equation (2.11) can be rewritten as a second order differential equation in the local angle, $\theta(l)$, along the l-axis:

$$\frac{d^2\theta(l)}{dl^2} = \frac{F_y \cdot \cos\big(\theta(l)\big) - F_x \cdot \sin\big(\theta(l)\big)}{EI_x} \tag{2.12}$$

The derivation of equation (2.12) can be found in appendix A.2.

Equation (2.12) is numerically solved using Excel, with boundary conditions $\theta_0 = -\theta(L) = \alpha_0$ where α_0 is the chosen initial angle between horizontal and spring base. This results in a certain tip displacement, given the load forces. Use of the built-in Solver capabilities of Excel gives the possibility to evaluate the vertical spring constant and horizontal force after any horizontal compression, see figure 20.

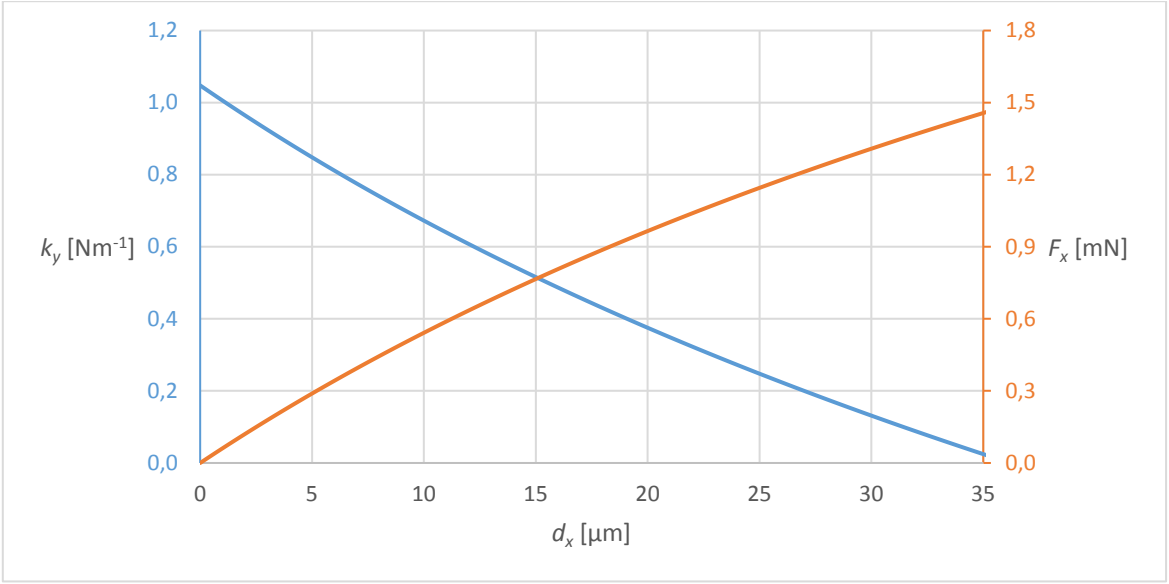

Figure 20. Spring constant in the y-direction of, and horizontal force on a curved cantilever spring versus the compression in x-direction of a single spring.

The initial radius of curvature of the spring is chosen such that the required spring constant reduction is obtained at a compression of about $35\ \mu m$.

2.4 Electro-Thermal Actuator theory and modeling

The compression of the curved cantilever springs is done using an Electro-Thermal Actuator beam. A voltage can be applied over this beam, which generates a current due to the resistance of the beam. The current flowing through the beam generates a power in the beam, causing the beam to heat up (Joule heating). The high temperature forces the anchored beam to expand, but because the beam is anchored internal stress will be created inside the beam. If the internal stress is high enough the beam will buckle in the first mode, see figure 21.

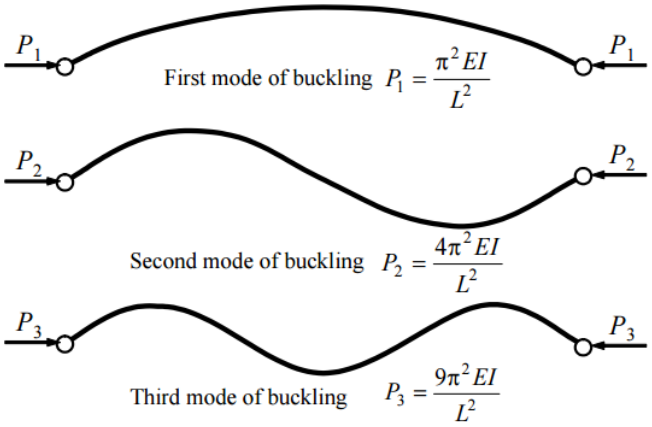

Figure 21. Schematics of the first 3 modes of buckling accompanied with the corresponding formula for the critical load. [10]

The direction of buckling can be chosen by giving the beam a slight offset in the preferred direction. Due to the first mode buckling of the beam, the apex is pushed outwards, which exerts a force that can compress the curved cantilever springs, as illustrated in figure 22.

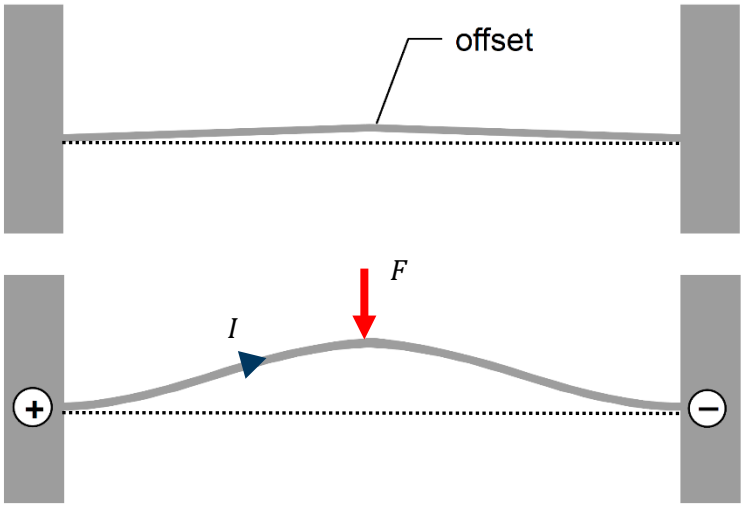

Figure 22. Working principle of a V-shaped ETA.
Top: The initial state of the ETA with a slight offset to control the direction of first mode buckling. Bottom: The apex is pushed outward due to Joule heating caused by the applied voltage over the beam. [11]

By compressing the springs, more force will act on the tip of the ETA, causing the inline force of the beam to become larger. When the inline force is larger than the critical load, the ETA will buckle in the second mode. The critical load of a single ETA can be estimated by using the equation for second mode of buckling in figure 21. At room temperature this gives $P_2 = 149\ \mathrm{mN}$.

The mathematical analysis of the working principle of the V-shaped ETA beam can be split into 2 parts: the Electro-Thermal part, with the current as input and the temperature as output, and the Thermo-Mechanical part, with the average temperature increase as input and the beam tip displacement as output. Both of these parts are described by [11] and [12] respectively. Their description will be used as inspiration for the modelling of the ETA.

A schematic zoom in of an ETA shows three sub-beams connected by reinforcing beams, see figure 23. The three sub-beams all have their own width and are separated mutually by gaps. The Thermo-mechanical model, that will be described below, requires the knowledge of the second moment of

area, I_x, of a simple solid beam. The ETA has a for more complex beam structure, so an effective I_x needs to be determined for the model. This can be done by calculating I_x for the entire width, subtracting I_x for the middle sub-beam with the gaps and adding the I_x of the middle sub-beam. Formula wise the effective second moment of area, $I_{x,eff}$, can be calculated by:

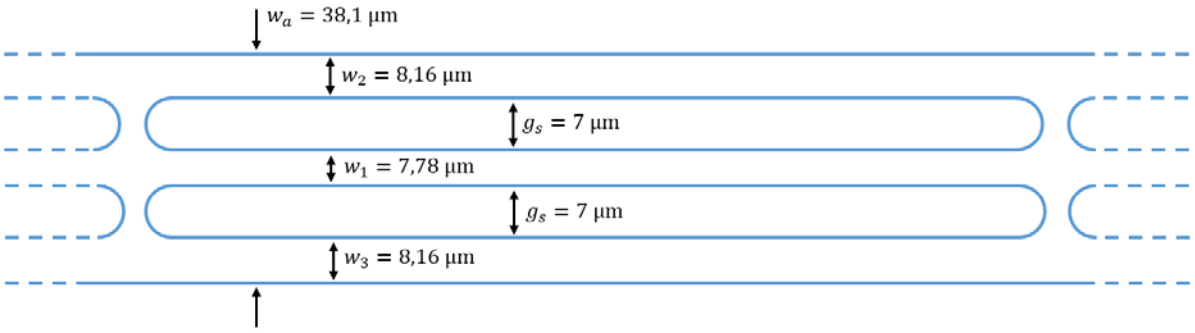

Figure 23. A schematic zoom in of an ETA accompanied with the sub-beam and gap widths.

$$I_{x,eff} = \frac{h}{12} \cdot ({w_a}^3 - (w_1 + 2 \cdot g_s)^3 + {w_1}^3) \tag{2.13}$$

Where h the beam height, w_a the total ETA beam width, w_1 the middle sub-beam width and g_1 the gap size between the sub-beams. The Electro-thermal model uses the effective width, w_e, which is the summed width of the three sub-beams, w_1, w_2 and w_3.

2.4.1 Electro-Thermal model

The heat transfer in a stationary beam in thermal equilibrium is described schematically in figure 24. It shows a section of a solid beam and a nearby substrate, with mutual distance g. The beam is divided into three small segments, with the middle segment having a length of $\Delta x = x_2 - x_1$ and temperature T. Joule heating and a conduction in silicon at the positive temperature slope at x_2 cause the heat generation of the middle segment. Convection to the substrate through air, conduction in silicon at the negative temperature slope at x_1 and radiation contribute to the heat loss of the middle segment. This model considers the quasi-static case, where the temperature is independent of time and only a function of x. Energy conservation results into equation (2.14).

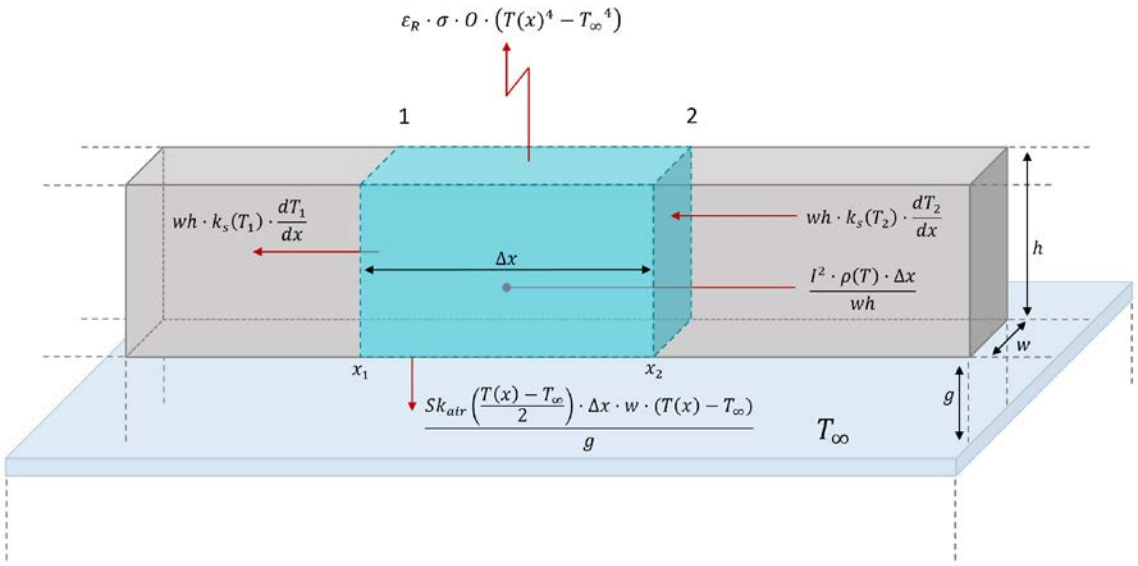

Figure 24. Heat transfer of a small beam segment Δx.

$$wh\left(k_s(T_2)\frac{dT_2}{dx} - k_s(T_1)\frac{dT_1}{dx}\right) + \Delta x\left[\frac{I^2\rho(T)}{wh} - wSk_{air}\left(\frac{T(x)+T_\infty}{2}\right)\frac{T(x)-T_\infty}{g} - \varepsilon_R\sigma O\left(T(x)^4 - T_\infty{}^4\right)\right] = 0 \qquad (2.14)$$

Where k_s and k_{air} are the thermal conductivity of silicon and air respectively, T_n is the temperature at x_n, I the current, S the shape factor, $T(x)$ the temperature of the middle segment of the beam, T_∞ the substrate temperature, g the distance between beam and substrate, h the beam height, w the beam width, ε_R the emissivity of silicon, σ the Stefan-Boltzmann constant and O the effective surface area of the middle segment. Between the beam and the substrate there is a temperature gradient. This means that k_{air} will change along the gradient. It is chosen to use the average of k_{air} at $T(x)$ and T_∞ in equation (2.14), for k_{air} as function of temperature can assumed to be linear (see appendix B.2). Dividing equation (2.14) by Δx and taking the limit for $\Delta x = 0$, results into this second order differential equation:

$$\frac{d^2T(x)}{dx^2} = \frac{1}{k_s(T)}\left(\frac{(T(x)-T_\infty)Sk_{air}\left(\frac{T(x)+T_\infty}{2}\right)}{gh} + \frac{\varepsilon_R\sigma O\left(T(x)^4 - T_\infty{}^4\right)}{wh} - \frac{I^2\rho(T)}{(wh)^2} - \left(\frac{dT(x)}{dx}\right)^2 \cdot \frac{dk_s(T)}{dT}\right) \qquad (2.15)$$

This equation can be solved numerically, given the boundary conditions $T(0) = T_\infty, \frac{dT(L)}{dx} = 0$.The numerical equation (2.15) is discussed in appendix A.3.1. The equation is implemented in an Excel worksheet. A typical model result from temperature profile of a beam half in air and in vacuum, with the same maximum temperature, is shown in figure 25.

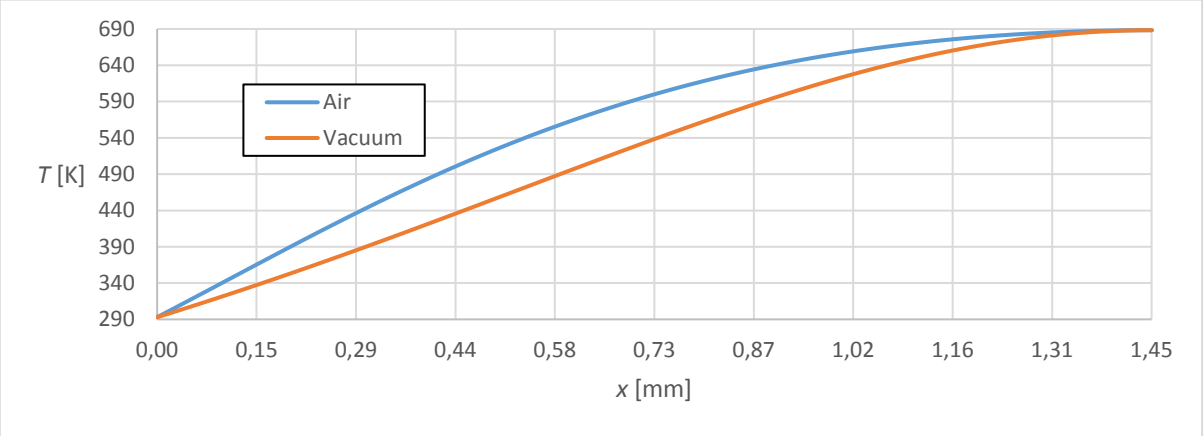

Figure 25. A typical model result from Electro-thermal model of the temperature profile of a beam half in air and in vacuum. The figure shows the temperature as function of the x-coordinate of the beam.

Besides a temperature profile can the model also predict the resistance behavior as function of power of a single beam. A typical model result from this in air an vacuum is shown in figure 26.

This model is inspired by [11], in which the material properties k_s, k_{air} and ρ are assumed to be independent on temperature. In that case, in absence of radiation ($\varepsilon_R = 0$), equation (2.15) simplifies to:

$$\frac{d^2T(x)}{dx^2}k_s - \frac{(T(x)-T_\infty)\cdot Sk_{air}}{gh} + \frac{I^2\rho}{(wh)^2} = 0 \qquad (2.16)$$

Using the boundary conditions $T(0) = T(2L) = T_\infty$, this has the analytical solution: (see appendix A.3.2):

$$T(x) = T_\infty + \frac{J^2\rho}{k_s\, b^2} \cdot \left(1 + \frac{e^{-2bL} - 1}{e^{2bL} - e^{-2bL}} \cdot e^{bx} - \frac{e^{2bL} - 1}{e^{2bL} - e^{-2bL}} \cdot e^{-bx}\right) \qquad (2.17)$$

Where, $b = \sqrt{\frac{Sk_{air}}{k_s gh}}$. Equation (2.17) is used to verify the numerical scheme mentioned above.

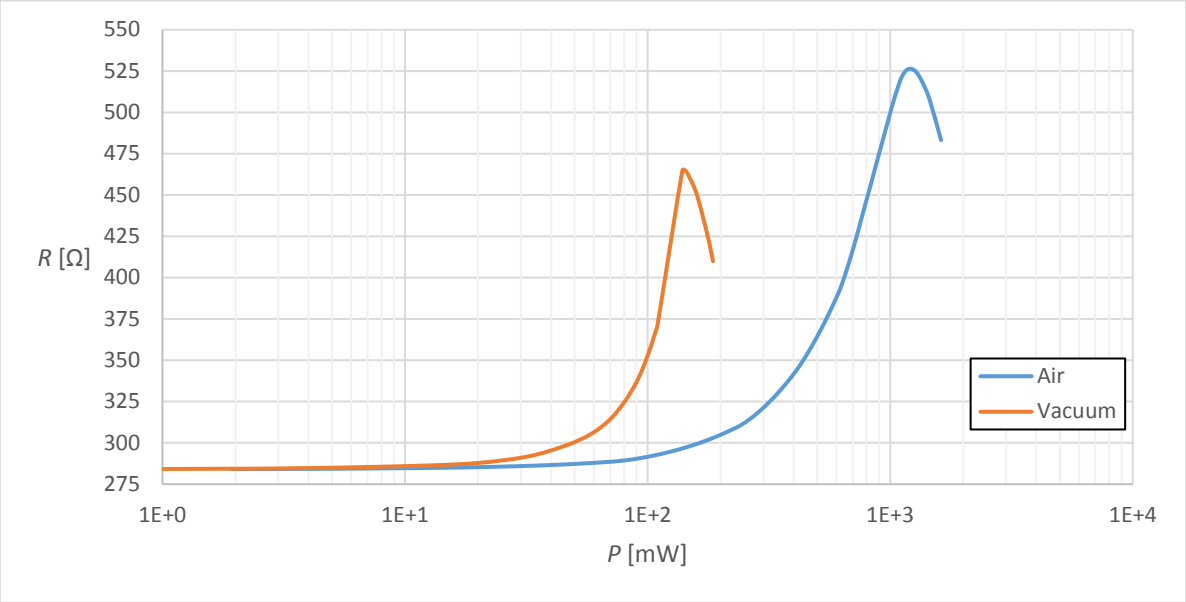

Figure 26. A typical model result from Electro-thermal model of the resistance as function of power of a single beam in air and in vacuum.

2.4.1.1 Shape factor

The heat conduction through air to the substrate is not only done via the bottom of the beam (figure 27A), but also the sides (figure 27B). Moreover, neighboring ETA sub-beams make the heat conduction even more complex (figure 27C). It is quite difficult to find an analytic expression for the heat conduction through air via the sides. So, the conduction from the sides is accounted for by a shape conduction factor $S > 1$, which can be calculated using 2D or 3D finite element modeling.

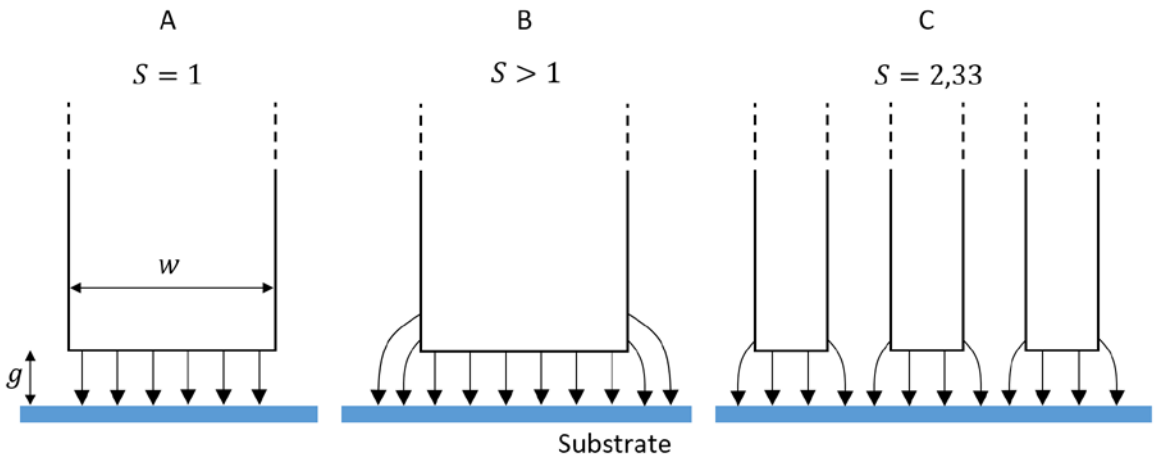

Figure 27. Illustration of the heat conduction through air to the substrate at $S = 1$ and $S > 1$.
A: The heat conduction to the substrate at $S = 1$ is completely through the bottom of the beam. B: At $S > 1$, is the heat conduction to the substrate partially via the side. The higher S, the more heat conduction via the side. C: Schematic cross-section view of the accelerometer MEMS used ETA beam. With FEM modelling is determined that $S = 2{,}33$.

For the three-beam ETA, S is determined by a 2D FEM model (done by Eric Hennes), with result $S = 2{,}33$. It is assumed that the reinforcing beams have no effect on S and S is independent on temperature, thus making S constant over the entire beam.

2.4.2 Thermo-Mechanical model

The analytical ETA beam model described in [12] is adopted. A sketch of the geometry and symbols used is shown in figure 28. Because of the symmetry, only half the beam needs to be modelled.

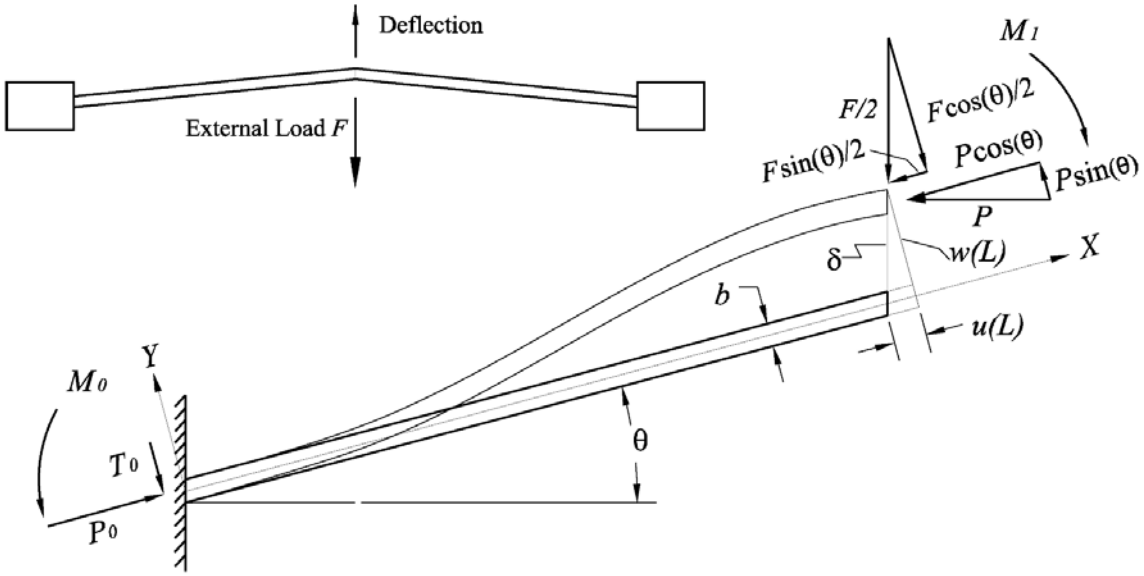

Figure 28. The geometry and loads of a V-shaped beam actuator. [12]

There are 3 strains which play a role in the ETA beam analysis: bending strain, ε_b, total inline strain, ε_s, and thermal strain, ε_T:

$$\varepsilon_b = y \cdot \frac{d^2 w(x)}{dx^2} \tag{2.18}$$

Where y is the vertical distance from neutral beam axis and $w(x)$ the transversal displacement of the beam along the neutral x-axis.

$$\varepsilon_s = \frac{du(x)}{dx} + \frac{1}{2} \cdot \left(\frac{dw(x)}{dx}\right)^2 \tag{2.19}$$

Where $u(x)$ is the longitudinal displacement of the beam along the neutral x-axis. The thermal strain is given by:

$$\varepsilon_T = \alpha(T) \cdot \Delta T(x) \tag{2.20}$$

Where α is the thermal expansion coefficient, which is dependent on temperature (see appendix B.1.3) and ΔT the temperature increase, which is dependent on the x-coordinate on the beam. To use equation (2.20) in the model, the average of all the ε_T along the beam will be used as input. The derivation of the strains can be found in appendix A.4.1.

Equation (2.18) shows that in the center of the beam, there is no effect of the bending strain. At the top the beam the bending strain is the largest and positive thus giving an expansion. At the bottom of the beam the bending strain is the smallest and negative thus giving a compression.

Considering the forces and moment acting on the beam shows that the beam base exerts an inline force P_0 on the beam, that counters the force that is caused when the free expansion of the beam is inhibited. The strain due to P_0 equals $-\frac{P_0}{EA}$, where A is the surface area of the cross-section. For $y = 0$, this gives a connection between the total average strain, the external force and the average thermal strain:

$$\varepsilon_s = -\frac{P_0}{EA} + \overline{\alpha \cdot \Delta T} \tag{2.21}$$

Balancing the moments in any point x along the beam gives:

$$-EI_x \cdot \frac{d^2w(x)}{dx^2} = P_0 \cdot w(x) + T_0 \cdot x + M_0 \tag{2.22}$$

Where T_0 and M_0 are the transversal force and moment acting on the fixed beam end respectively. Equation (2.22) is a differential equation which can be solved for the clamping boundary conditions and the relations for P_0 and T_0 with F, found in appendix A.4.2. The solution to equation (2.22) reads:

$$w(x) = \left(\tan\theta - \frac{F_v}{2k^2 EI_x \cos\theta}\right) \cdot \left(\frac{\sin kx}{k} + \frac{(\cos kL - 1) \cdot (\cos kx - 1)}{k \sin kL} - x\right) \tag{2.23}$$

Where θ is the angle between horizontal and neutral beam axis, F_v is the vertically applied force on the beam, L the half-span of the beam and the eigenvalue k is defined as $k = \sqrt{\frac{P_0}{EI_x}}$. k can be calculated from the solution to equation (2.21), after substituting equation (2.19) and (2.23). This solution gives a transcendental equation which contains the applied beam tip force F_v, the average thermal strain of the beam $\overline{\alpha\Delta T}$ and k. For each value of F_v and $\overline{\alpha\Delta T}$ can k be numerically obtained by solving the transcendental equation:

$$c(k, F_v, \overline{\alpha\Delta T}) = 0 \tag{2.24}$$

The complete equation (2.24) can be found in appendix A.4.3.

The tip displacement δ of the beam can be calculated by dividing the transversal displacement on $x = L$ by $\cos\theta$, giving:

$$\delta = \frac{w(L)}{\cos\theta} = \left(\tan\theta - \frac{F_v}{2k^2 EI_x \cos\theta}\right) \cdot \left(\frac{2\tan\left(\frac{kL}{2}\right) - kL}{k\cos\theta}\right) \tag{2.25}$$

A typical result from the Thermo-mechanical model of the tip displacement in air and vacuum is shown in figure 29.

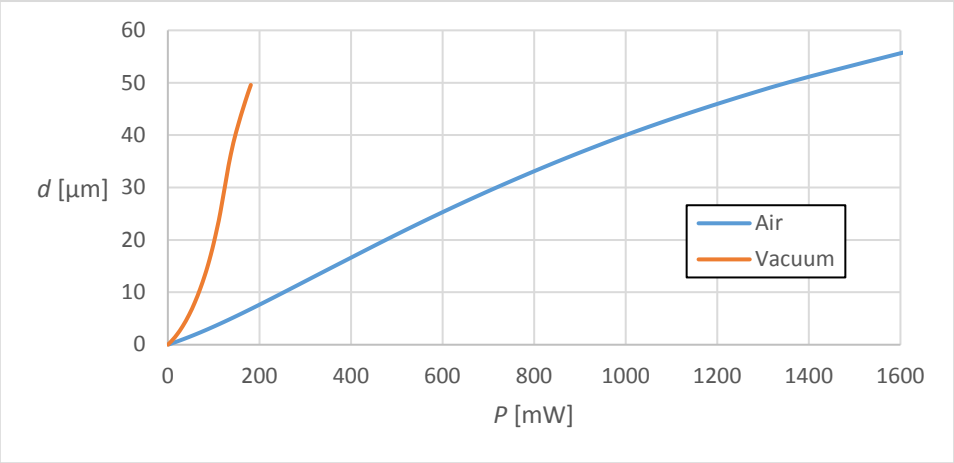

Figure 29. A typical result from the Thermo-mechanical model. The figure shows the tip displacement as function of power.

2.5 Material properties

As described do the models require $k_s(T)$, $k_{air}(T)$, $\alpha(T)$, $\rho(T)$ and $E(T)$ (presented in appendix B). All of these symbols except $\rho(T)$, for highly doped silicon, is found in literature. The resistivity of the used silicon is specified to be between $0{,}005\ \Omega\text{cm}$ and $0{,}02\ \Omega\text{cm}$ [8] at room temperature. For the wafers used at Nikhef, the resistivity at room-temperature is measured. However, the resistivity at elevated temperatures is not precisely known in this doping regime. $\rho(T)$ can be roughly guessed based on known curves at neighboring carrier concentrations, see figure 30.

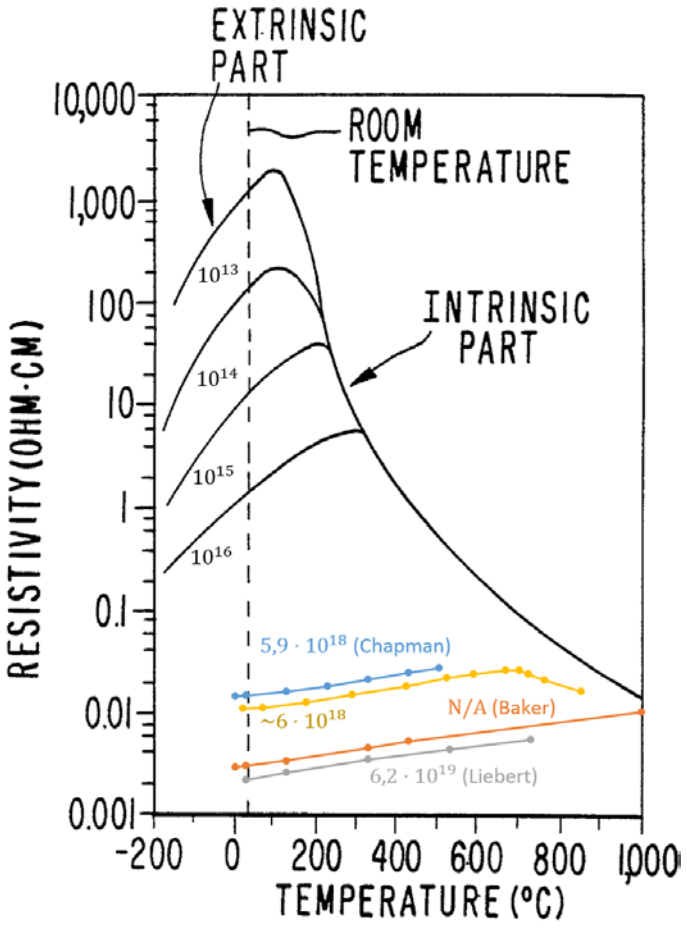

Figure 30. Resistivity of doped silicon versus temperature at different concentrations of carriers/cm^3 (10^{13} to $6{,}2 \cdot 10^{19}$). [13] [14] [15] [16]

When the temperature increases, it is expected that the resistivity of the silicon will rise until it 'hits' the intrinsic part after which the resistivity will drop. In this project it is tried to indirectly measure $\rho(T)$, by matching the Electro-thermal model with the measured resistance. (The measured $\rho(T)$ is already present in figure 30 as the yellow line at doping concentration $\sim 6 \cdot 10^{18}$ carriers/cm^3)

3 Measurement setup and methods

This chapter will describe the measurement methods used for measuring the resistance and displacement of the ETAs of both MEMS designs. It contains a few electrical schemes and explains the operation of the Python photo processing module. Also, this chapter gives a small rundown of the used vacuum setup.

3.1 Quasi-static ETA resistance measurement

The ETAs are designed to compress the curved cantilever springs when they expand. The required expansion is obtained by electrically heating the ETA from a voltage source. The power is obtained from a source voltage and current, U_s and I_s respectively, according to:

$$P_{ETA} = U_s \cdot I_s \tag{3.1}$$

A voltage source is used to actuate all the ETAs, during this project. The total ETA resistance, R_{ETA}, can be calculated according to Ohm's law by $\frac{U_s}{I_s}$.

To connect the MEMS chip to an electrical source or meter, the chip is placed in a chip carrier. The chip carrier has 84 connection, with 21 on each side. To bond each end of the ETA to the carrier, a small aluminum wire is wringed on an ETA bonding pad and on a golden connector on the carrier, using a MechEL/MEI 907 wedge bonder [17]. On the edge of the chip, carrier wires can be soldered to the corresponding connectors.

During the bonding of the aluminum wires a contact resistance, R_c, is introduced, because the wires are wringed on the native insulating silicon oxide layer with a thickness of several nanometer. This layer prevents full electrical contact between the wire and the bonding pad, thus creating a resistance. This contact resistance is not negligible and will add up to the measured resistance. The values of contact resistances vary mutually. Also does the resistance change when a current flows through it (see chapter 4.1.3). Therefore, it is difficult to find an exact value for R_c.

The Back ETA bonding pad on the G1.4 MEMS design, has an extra silicon piece to extend the length of the bonding pad (anchor), on account of the possibility of separate ETA actuation, see figure 8 and figure 31. Due to this added piece of silicon, the total measured resistance of the Back ETA will go up. The resistance of this piece at room temperature, R_p, can be estimated according to:

$$R_p = \rho(T_\infty) \cdot \frac{L_p}{A_p} \tag{3.2}$$

Where L_p and A_p are the length and cross-section area of the silicon piece respectively.

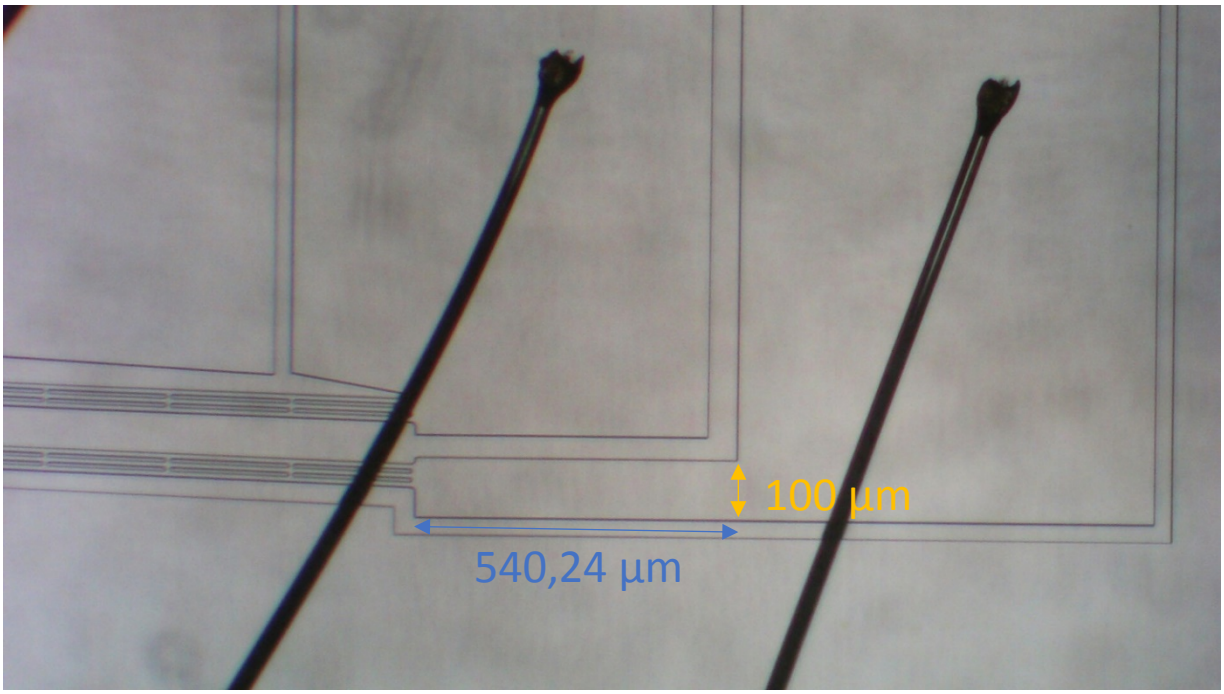

Figure 31. Microscope picture of the lengthened G1.4 Back ETA bonding pad, with dimensions.

An electrical scheme of the ETAs of both MEMS designs can be set up. Though the G1.5 MEMS design only has two bonding pads, it is bonded with three aluminum wires (two on one pad and one on the other). The electrical schemes are presented in figure 32.

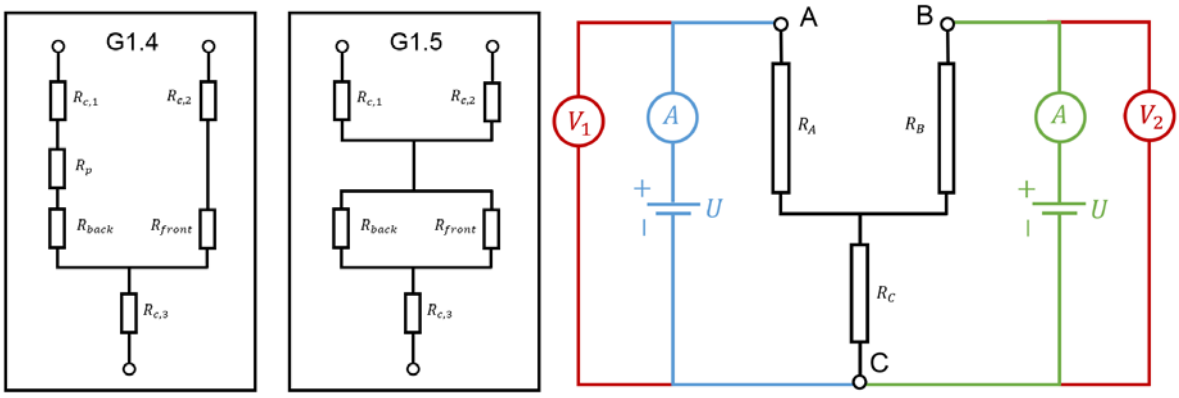

	G1.4	G1.5
$R_A =$	$R_{c,1} + R_p + R_{back}$	$R_{c,1}$
$R_B =$	$R_{c,2} + R_{front}$	$R_{c,2}$
$R_C =$	$R_{c,3}$	$R_{c,3} + \frac{R_{front} \cdot R_{back}}{R_{front} + R_{back}}$

Figure 32. The electrical schemes of the ETAs of both MEMS designs, accompanied with two source and meter connection possibilities.

The connection C is always the reference point during the ETA measurements and a voltage source is connected to A, B or both (depending on which ETA is being actuated in the G1.4). If the voltage source is connected between A and C (blue schematic), the following holds:

$$\frac{V_1}{I} = R_A + R_C, \qquad \frac{V_2}{I} = R_C \tag{3.3}$$

if the voltage source is connected between B and C (green schematic), the following holds:

$$\frac{V_1}{I} = R_C, \qquad \frac{V_2}{I} = R_B + R_C \tag{3.4}$$

Assuming $R_{back} = R_{front}$, $R_{c,3} = R_{c,2}$ or $R_{c,1}$ and R_p is correctly estimated at room temperature, all the resistances can be calculated from the measurements at room temperature. Unfortunately it is impossible to directly measure contact resistance $R_{c,1}$ and $R_{c,2}$ on the G1.4 MEMS, due to the fact that the ETA resistance is always in series with $R_{c,1}$ or $R_{c,2}$. $R_{c,1}$ or $R_{c,2}$ can be estimated by measuring $R_{c,3}$ and using the earlier made assumptions. $R_{c,3}$ can be measured using both schematics from figure 32. Because of the high impedance, R_V, of the voltage meter, almost no current flows through it, thus can be assumed that all the current flows through $R_{c,3}$ and $R_{c,3} \ll R_V$. Formula wise this can be shown as:

$$I_{R_{c,3}} = I \cdot \frac{R_V}{R_{c,3} + R_V} = I \cdot \frac{1}{\frac{R_{c,3}}{R_V} + 1} \approx I. \tag{3.5}$$

On the G1.5 ETA the contact resistances $R_{c,1}$ and $R_{c,2}$ can be measured directly using both schematics.

A constant voltage source, Agilent E3648A, is used for the quasi-static measurements. The voltage over and the current through the ETA is measured with a Tenma 72-2040 multimeter and a Voltcraft 98 multimeter respectively (specifications have not been found). Direct resistance measurement is also done with a Tenma 72-2040.

3.2 Pulsed ETA resistance measurement

One of the disadvantages of quasi-static actuation is the constant current through the ETA, which beside the ETA also heats up the substrate. This causes the substrate to expand, cancelling out the expansion of the ETA. Second, the ETA could melt, because after the required tip displacement there is still a power being dissipated. If the dissipated power is too much, the ETA melts. These disadvantages can be avoided by pulsed actuation. This limits the time a current goes through the ETA, so it heats up till the required tip displacement is reached and deactivates after. The pulse time and height needs to be taken into account, for a too long/high pulse could still melt the ETA. The pulse time needs be larger than the mechanical and thermal time constant, but shorter than the time it takes for the thermal-runaway effect (see figure 42). The thermal time constant both in air and vacuum is estimated in appendix C. To measure the ETA resistance the voltage over the total system and the voltage over a shunt resistance is measured using an oscilloscope. The electrical circuit is drawn schematically in figure 33.

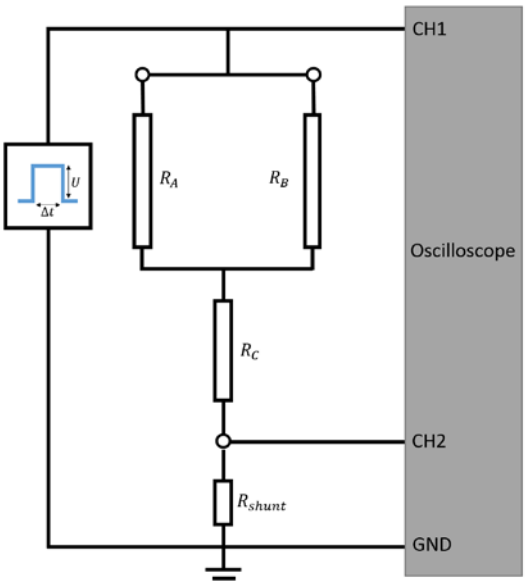

Figure 33. Schematic of the electrical circuit for pulsed actuation measurement.

Channel 1 measures the total voltage over the system, $U_{tot}(t)$, and channel 2 measures the voltage over the shunt resistance, $U_{shunt}(t)$. These can be used to calculate the voltage over and the current through the ETA:

$$U_{ETA}(t) = U_{tot}(t) - U_{shunt}(t), \qquad I_{ETA}(t) = \frac{U_{shunt}(t)}{R_{shunt}} \tag{3.6}$$

Subsequently, Ohm's law and equation (3.1) can be used to calculate the resistance of and power dissipated in the ETA as function of time.

The pulses are given using the Tabor Electronics 50MHz Single / Dual Channel Pulse Generator model 8500 [18]. The pulsed voltage signals are measured with a Tektronix TDS3034 oscilloscope [19] and a $10\ \Omega \pm 5\%$ resistance is placed in series with the ETA.

3.3 ETA mechanical behavior measurement

When an ETA heats up it expands. Being fixed between two anchors (bonding pads), it will buckle into its first mode. The ETA has a slight V-shape with angle 2° to ensure the tip displacement is in the direction of the curved cantilever springs (see figure 12 and 14). It is measured with a microscope with built-in digital camera.

The microscope has 2,5x 5x and 20x objectives. The eyepiece has a magnification of 10, so the maximum microscope magnification is 200x. The camera pictures of the ETA are used to measure its shape and tip displacement during actuation and after locking. For the tip displacement a Python photo processing module is used, made by Boris Boom, which estimates the distance in pixels between two selected parallel light-dark transitions. See for instance the edges behind the red and blue vertical lines in figure 34. The module makes a fit from the average of the first derivative of the light intensity around both sides of the horizontal blue line (see bottom of figure 34). Subsequently, the maximum around the selected parallel light-dark transitions is selected by the module and subtracted, giving the distance in number pixels between the selected parallel light-dark transitions.

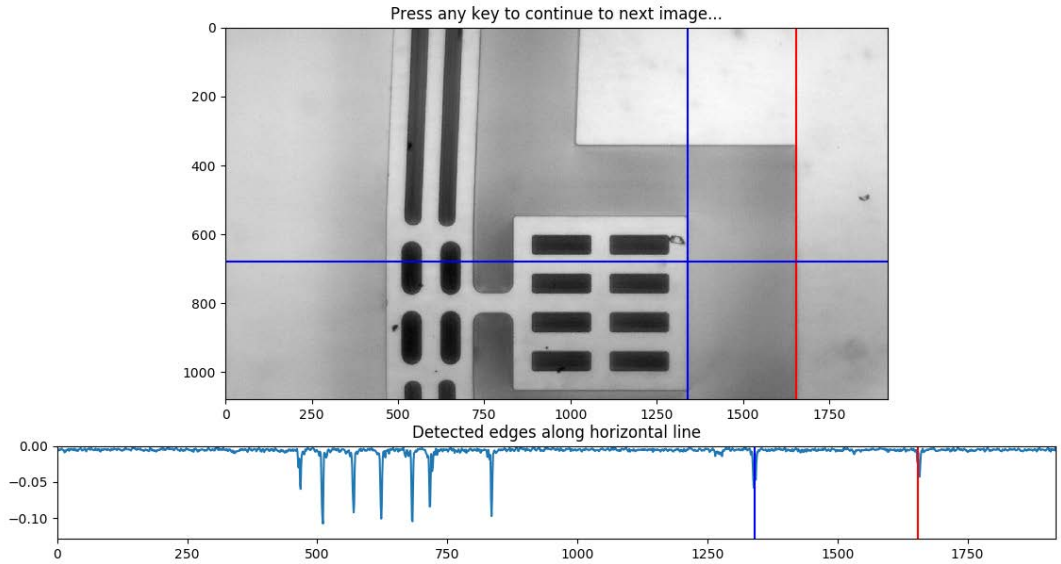

Figure 34. Layout of the photo processing module. Top: the grayscale of the taken picture with the first selected edge (blue) and the second selected edge (red). Bottom: the plot of the edges along the horizontal blue line. The module will calculate the distance in pixels between the peak closest to the blue line and the peak closest to the red line.

The resolution of the module is calculated by measuring the number pixel distance of a known width in µm. The determined transfer from pixels to µm is $0{,}14\,\frac{\mu m}{\text{pixel}}$.

The pictures of the G1.5 #11 Q2 ETA pair are taken with a Future Optics MDC2000 [20]. The rest of the pictures are taken with a Moticam BTU10 [21].

3.4 Vacuum setup

The MEMS will be operated in vacuum, for this decreases the damping of the system. When produced the MEMS will be evacuated and covered with an nontransparent lid. This means that the ETAs will be actuated in vacuum, without optical observance. To investigate the effect of vacuum on the ETAs, a vacuum setup is made. This setup consists of a pot with a hole on which the vacuum pump can be connected. The connected vacuum pump is a HiPace® 80 [22]. In the lid is a TECHSPEC® Fused Silica Window placed [23], through which can be looked with a microscope. On the bottom side of the lid screw holes are made which can be used to hang up a MEMS in front of the window. A connector is put on the lid which connects the wires from the MEMS with the sources and meters outside the vacuum system. The pressure in the vacuum system is measured with a Pfeiffer Vacuum MPT 200 AR [24], which measures pressures below $2 \cdot 10^{-3}$ mbar with $\pm$ 25 % accuracy. As the measurements in the vacuum setup will be done in the same way as described before, there will be no changes in the electrical circuit of the ETAs. Pictures of the vacuum system can be found in appendix E.

The thermal conductivity of air is not directly depended on the pressure. It depends on the mean free path of the air molecules. If the mean free path becomes longer than the distance between the ETA and the substrate, the thermal conductivity will decrease, because the molecules cannot make a successful collision with the substrate. The mean free path, l_{mfp}, is given by [25]:

$$l_{mfp} = \frac{k_B \cdot T}{\sqrt{2} \cdot \pi \cdot p \cdot {d_m}^2} \tag{3.6}$$

Where k_B is the Boltzmann constant, T is the temperature, p is the pressure and d_m is the diameter

of the molecules. Using the $l_{mfp} \cdot p$ values found in [25], the average air molecule diameter can be calculated using equation (3.6). This gives $d_{air} = 3{,}6 \cdot 10^{-10}$ m. The mean free path versus pressure is shown in figure 35.

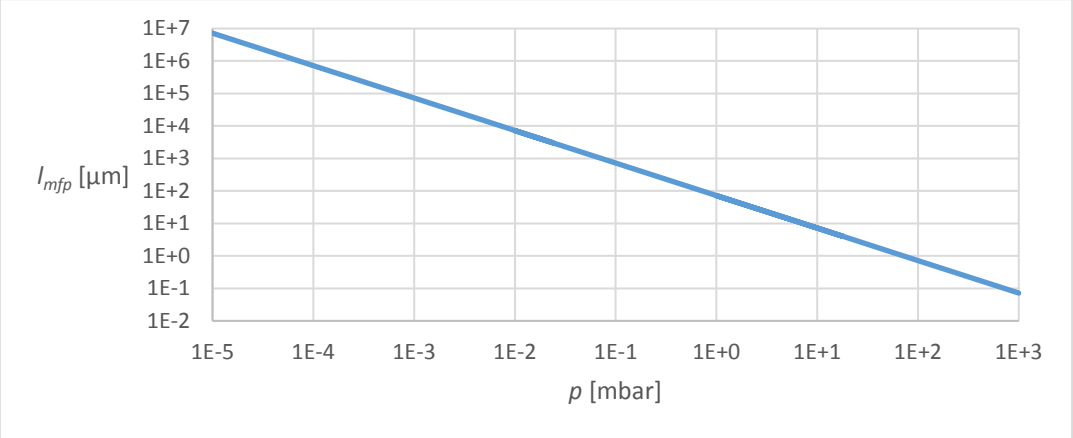

Figure 35. Mean free path of air versus pressure, at $T = 293{,}15$ K and $d_{air} = 3{,}6 \cdot 10^{-10}$ m.

At a mean free path of 4 µm, which is the gap size between the ETA and the substrate, is the required pressure 18 mbar. It is suspected that at pressures lower than 18 mbar the thermal conductivity of air drops, for the mean free path becomes longer than the gap size. The pressure at which the final MEMS design will be produced is around $2 \cdot 10^{-2}$ mbar. Figure 35 shows that the mean free path is for that pressure is about $3{,}5$ mm. It is assumed that the thermal conductivity of air can be neglected, because the mean free path is larger than the total length of the ETA.

4 Measurement results

This chapter will present the results from the measurements performed on the ETAs. It will consist of the quasi-static and dynamic actuation results of the resistance and displacement, both as a function of electrical power. Some of the results will be compared to or explained by the made models.

4.1 Resistance measurements

The resistance measurements consist of the measured resistance of the whole ETA, both quasi-statically and pulsed, and the resistance of the contacts. The resistance of the ETA is measured at atmospheric pressure and in vacuum. Measurement of the contact resistance is done only at atmospheric pressure, for it is believed that the vacuum will not affect the contact resistances.

4.1.1 Quasi-static G1.4 actuation measurement in air

The G1.4 MEMS design has the possibility to actuate both ETAs separately, so the resistance as function of power of both G1.4 #01 Q1 ETAs is measured. These results are presented in figure 36.

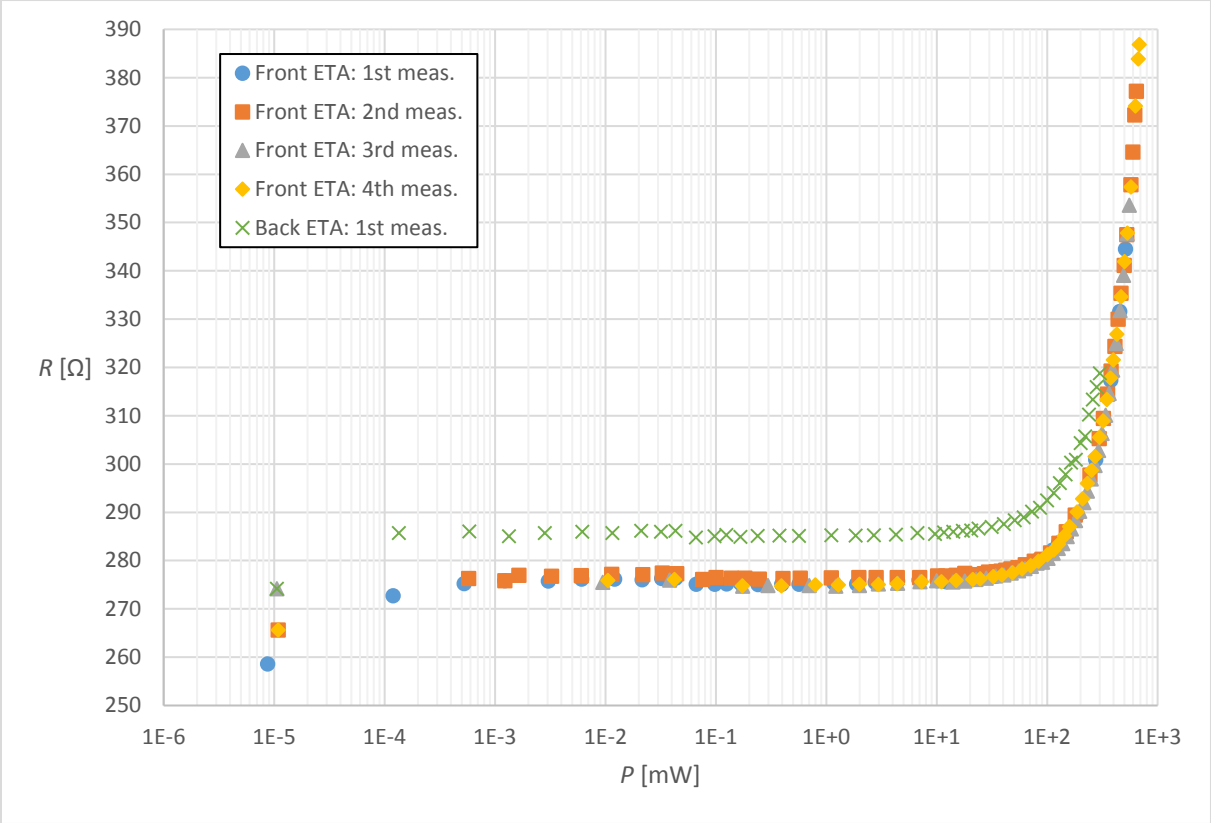

Figure 36. G1.4 #01 Q1 Front and Back ETA resistance versus power.

The resistance behavior as function of power of both the Front and Back ETA is as expected. As shown in figure 26, at low power is the ETA still at room temperature, thus there is no change in resistance until the temperature of the ETA increases significantly. Above $20\ \mathrm{mW}$ the Front ETA resistance rises till $385\ \Omega$ at $650\ \mathrm{mW}$. As earlier predicted in chapter 3.1, the Back ETA resistance is higher than the Front ETA resistance. The difference in resistance is approximately $10\ \Omega$ over the whole power range.

The resistance at room temperature of the Front and Back ETA of all the quadrants is measured directly. The results are presented in table 1.

Table 1. Data from the direct resistance measurement of the G1.4 #01 MEMS.

G1.4 #01	Q1	Q2	Q3	Q4
Front *R* [Ω]	276,4	281,8	273,0	277,7
Back *R* [Ω]	286,7	280,3	285,4	289,3
Difference *R* [Ω]	10,3	-1,5	12,4	11,6

The resistance value of Q2 has not been used, due to the plastic deformation of the Front ETA beam before the measurement. The average difference, $11{,}4\ \Omega$, can be ascribed to the anchor extension of the Back ETA, whose resistance is predicted to be $11{,}8\ \Omega$, using equation (3.2).

4.1.2 Quasi-static G1.5 actuation measurement in air

The total resistance of the G1.5 #11 Q2 ETA pair versus power is presented in figure 37.

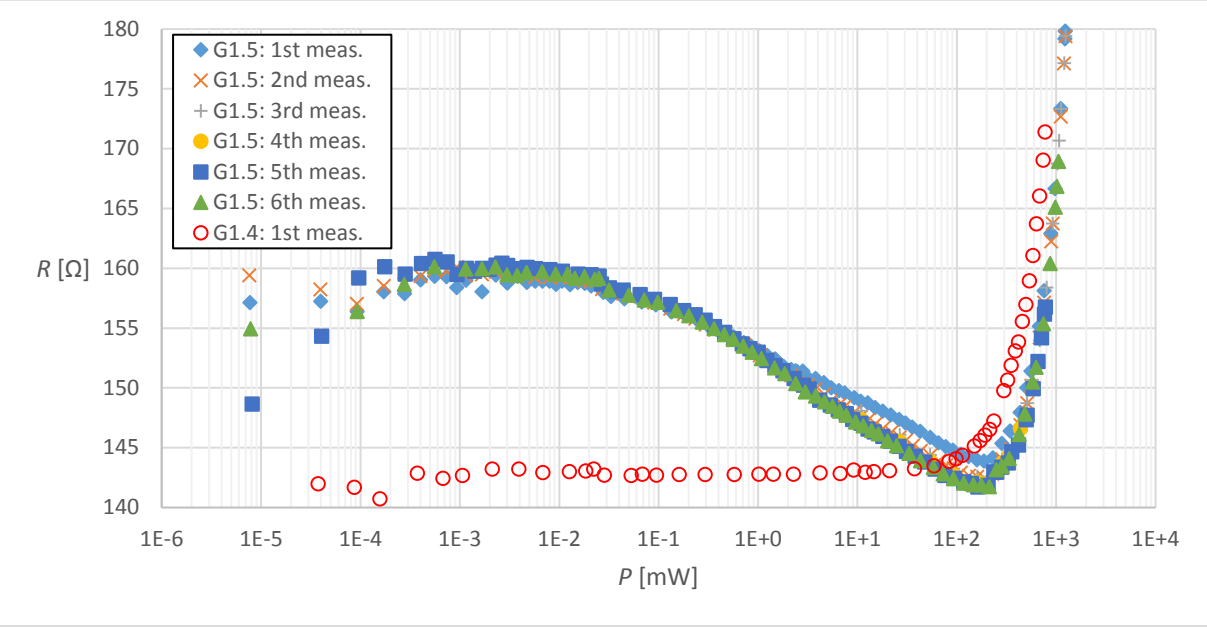

Figure 37. G1.5 #11 Q2 ETA pair total resistance versus power. For comparison, the G1.4 #01 Q1 ETA pair total resistance is added to the figure.

It shows the varying of the resistance at a power $< 10^{-4}$ mW. This is ascribed to the accuracy of the meters in combination with the very small current and voltage they had to measure. Between 10^{-4} mW and 10^{-2} mW the resistance is about constant, which is expected because the rise in temperature is negligible at this power, thus there is little to no increase in resistance. Between 10^{-2} mW and 200 mW the resistance drops by almost $20\ \Omega$. When comparing the resistance of the G1.5 to the G1.4 in this power range, it becomes clear that the resistance drop is an effect from the contact resistance, because the G1.4 and G1.5 ETAs are identical. Apparently the constant resistance decreases reversibly with the power, for all six measurements show the same drop. The drop in constant resistance is even higher than the drop of the G1.5 ETAs resistance, because the ETAs should already be increasing its resistance from 40 mW, but instead it increases from 200 mW. Above 200 mW the G1.5 ETAs resistance rises till $180\ \Omega$ at 1200 mW, which is a rise of approximately $37\ \Omega$. This would suggest a rise in $74\ \Omega$ for a single ETA at 600 mW. Comparing this to figure 36 the suggested rise results is $350\ \Omega$, which does not correspond with the measurement. There is a possibility that the G1.4 MEMS is bonded earlier than the G1.5 MEMS, causing the silicon oxide layer between the bonding pad and wire to be thinner on the G1.4 MEMS in comparison to the

G1.5 MEMS. Therefore, the contacts on the G1.5 have a higher resistance, which could explain the difference in resistance in figure 37.

4.1.3 Measurement of contact resistance

The contact resistances $R_{c,1}$ and $R_{c,2}$ of the G1.5 #11 Q1 ETA are measured for increasing power. This measurement is done three times and the results are presented in figure 38.

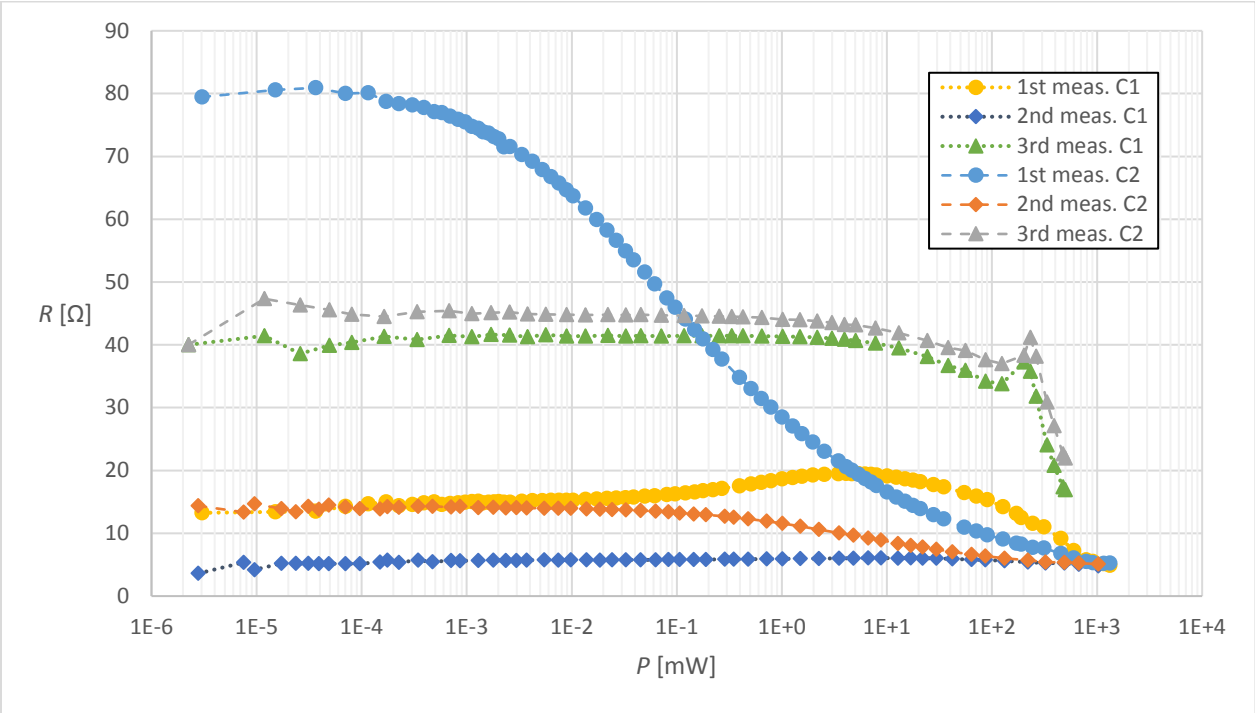

Figure 38. G1.5 #11 Q1 ETA pair contact resistance $R_{c,1}$ and $R_{c,2}$ versus power.

The initial values for the contact resistances are $R_{c,1} = 14\ \Omega$ and $R_{c,2} = 80\ \Omega$. This could indicate that the G1.5 #11 Q1 ETA pair is actuated before this measurement, because when power is dissipated in a contact, it lowers its resistance. When two bonding wires are connected to the same electric source, the most current flows through the contact with the least resistance causing the resistance to go down, due to power dissipation. Therefore, the current flow through this contact increases, lowering the resistance even more. Eventually, this ends with one low resistance contact and one (relatively) high resistance contact. After $1300\ \mathrm{mW}$ power dissipation in the contacts their resistances $R_{c,1}$ and $R_{c,2}$ drop to $5\ \Omega$ and $14\ \Omega$ respectively. This shows that high power dissipation in the contacts lowers their resistance irreversibly. Another power dissipation of $1300\ \mathrm{mW}$ partially destroyed/melted the contacts, because the resistance of both contacts increases. Red glowing of the contacts is observed at $200\ \mathrm{mW}$ during the last measurement. This probably completely destroyed/melted the contacts, because the resistance drops fast above $200\ \mathrm{mW}$.

It is possible that the contact resistance is reversible if the power dissipated in the contact is much lower than $1300\ \mathrm{mW}$, which is the case during the ETA actuation. For example, the resistance of $R_{c,2}$ drops from $80\ \Omega$ to $60\ \Omega$ during ETA actuation and rises back to $80\ \Omega$ again when the ETA is deactivated. This could be an explanation for the resistance drop in figure 37. No measurement has been done of the contact resistance at lower dissipated power to find the power till the contact resistances have reversible behavior.

The characteristic of the G1.4 #01 Q1 Front and Back ETA indicate that their contact resistances are constant. So, the value of $R_{c,3}$ at room temperature of the G1.4 #01 Q1 can be measured directly, see table 2.

Table 2. Data from the $R_{c,3}$ measurement of the G1.4 #01 Q1.

Measurement	1	2	3	4	5	6
$R_{c,3}$ [Ω]	5,22	5,22	5,20	5,21	5,21	5,20

The average value, $R_{c,3} = 5{,}21\ \Omega$, is approximately the same value $R_{c,1}$ has during the 2nd measurement shown in figure 38. So, it is likely that the G1.4 #01 Q1 ETA pair is actuated earlier and the contact resistances have been decreased to the lowest resistance without destroying them.

4.1.4 Unloaded quasi-static G1.4 actuation measurement in air and vacuum

For the complete electrical behavior of an ETA beam, at atmospheric pressure and vacuum, are the G1.4 #01 Q3 and Q2 Back ETA measured until they melted, see figure 39. This measurements shows that the maximum resistance for $p = 1000$ mbar and $p = 1{,}8 \cdot 10^{-5}$ mbar is at 1230 mW and 131 mW respectively.

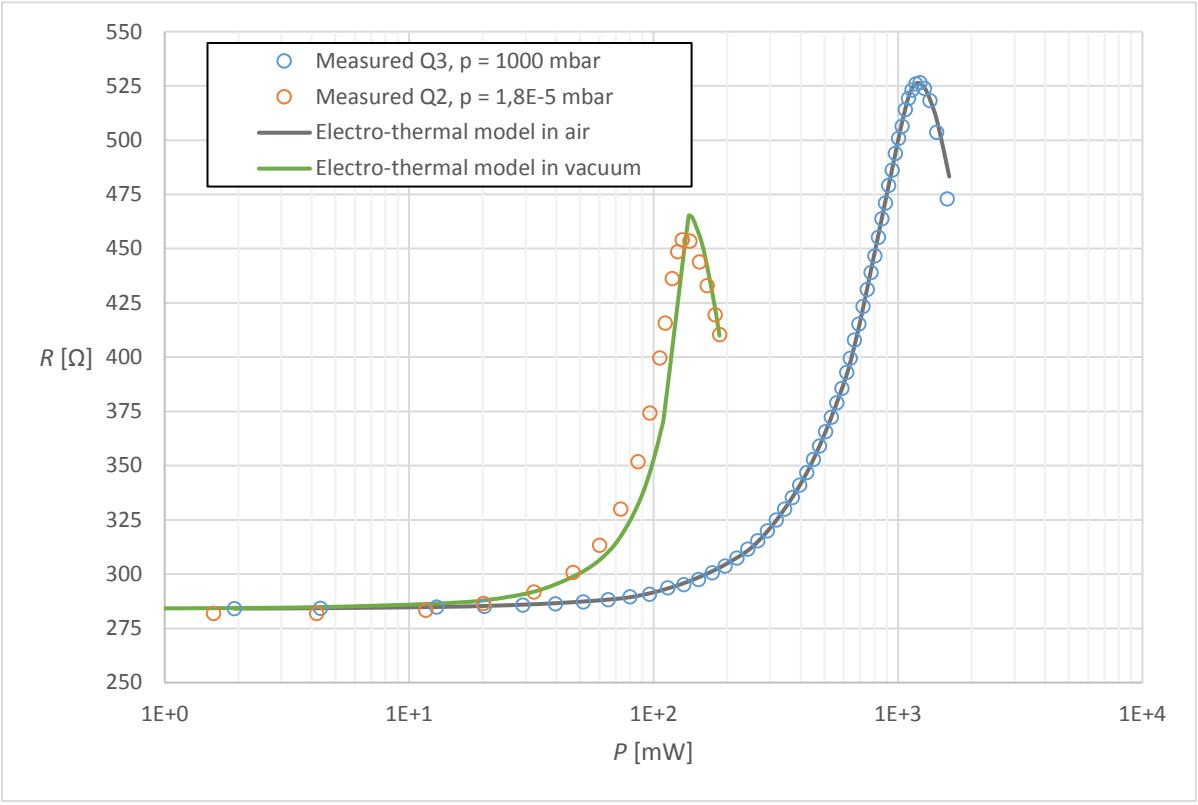

Figure 39. G1.4 #01 Q3 and Q2 Back ETA resistance versus power at different pressures, accompanied with the Electro-thermal model results for a single ETA at atmospheric pressure and in vacuum.

The resistance behavior as function of power is the same at different pressures, as it is constant at low power, will rise until the maximum is reached and drop after the maximum, due to the intrinsic wall. The resistance in vacuum rises faster than at atmospheric pressure. This can be explained by the fact that an ETA in vacuum loses no heat through air to the substrate, thus it gets hotter at lower power, meaning a higher resistance at lower power. The difference in maximum resistance can be explained by the temperature profile of the ETA beam, which is dependent on the presence of air. The Electro-thermal model can give an estimation of a temperature profile of a beam in air and

vacuum, at the same maximum temperature, see figure 25. The figure shows that the profile in air at the center of the beam ($x = 1{,}45$ mm) is much more flat than in vacuum. This indicates that the temperature profile in air has much more beam pieces, dx, which have a temperature that is close to the maximum temperature. As the total resistance of the beam is the sum of all small resistances, dR, which are all depended on temperature, is the maximum resistance in air always higher than in vacuum.

4.1.5 Pulsed G1.5 actuation measurement in air

During the pulsed actuation is tried to lock the shuttle in all the shuttle locks. Each time a pulse of 25 ms is used to actuate the ETA. The results of the complete shuttle locks with the G1.5 #11 Q2 ETA pair at $p = 1000$ mbar are presented in figure 40.

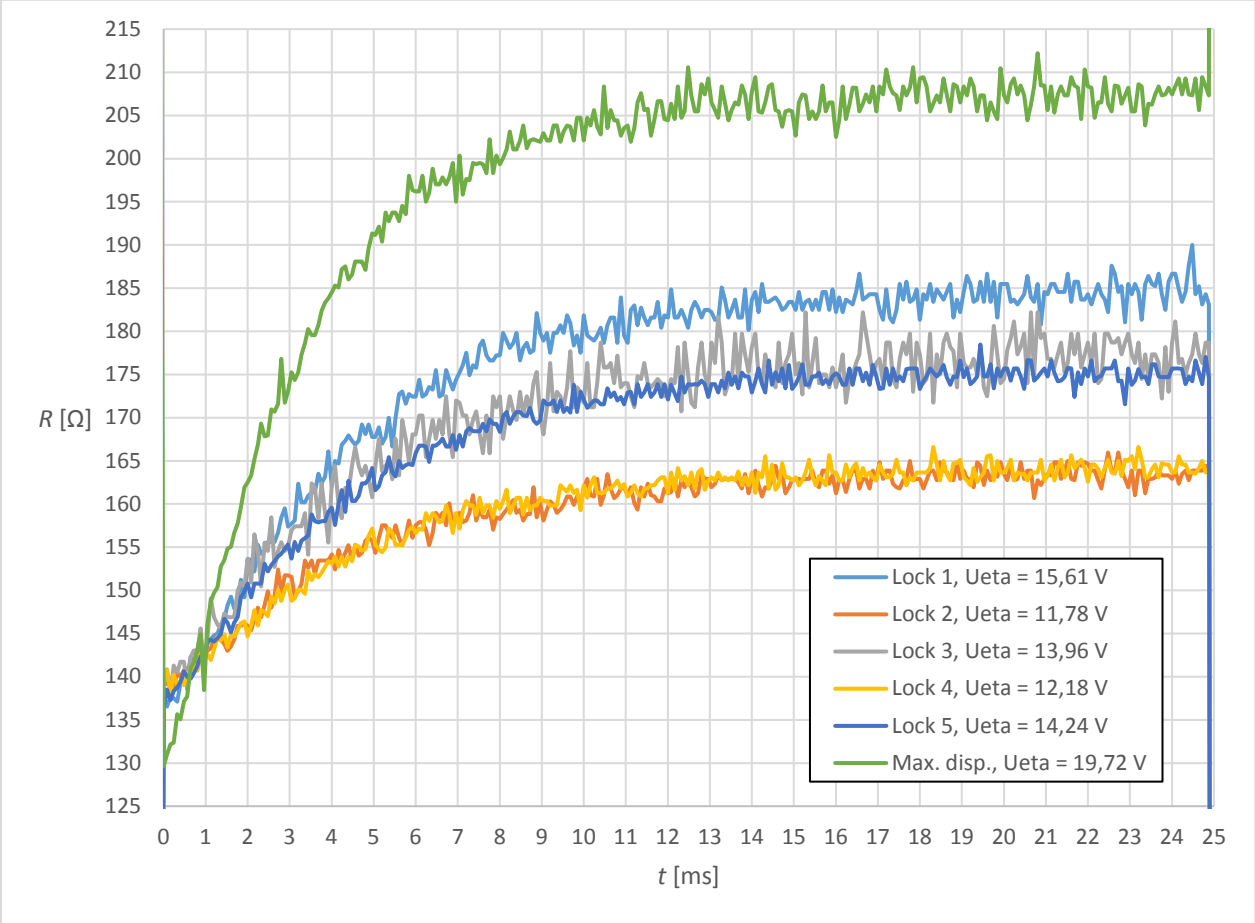

Figure 40. G1.5 #11 Q2 ETA pair, both ETA resistance vs. time (during pulse) at $p = 1000$ mbar from 1st Shuttle lock to maximum Shuttle displacement. U_{ETA} shown in the legend is the average voltage over the ETA between 15 ms and 24 ms during the pulse.

The thermal time constant, τ, can be estimated by determining the time where the resistance is $0{,}63 \cdot (R_e - R_i) + R_i$, with R_e the average resistance between $t = 15$ ms and $t = 24$ ms and R_i the resistance at $t = 0$ ms. The results of τ for the 6 pulses in air is shown in figure 41. The estimation of the time constants in air and vacuum, see appendix C, and a comparison to the estimated time constant made in [26] are also shown. The temperature of the beam is calculated by determining the

average current between $t = 15$ ms and $t = 24$ ms and using it as input for the Electro-thermal model, which gives the average temperature.

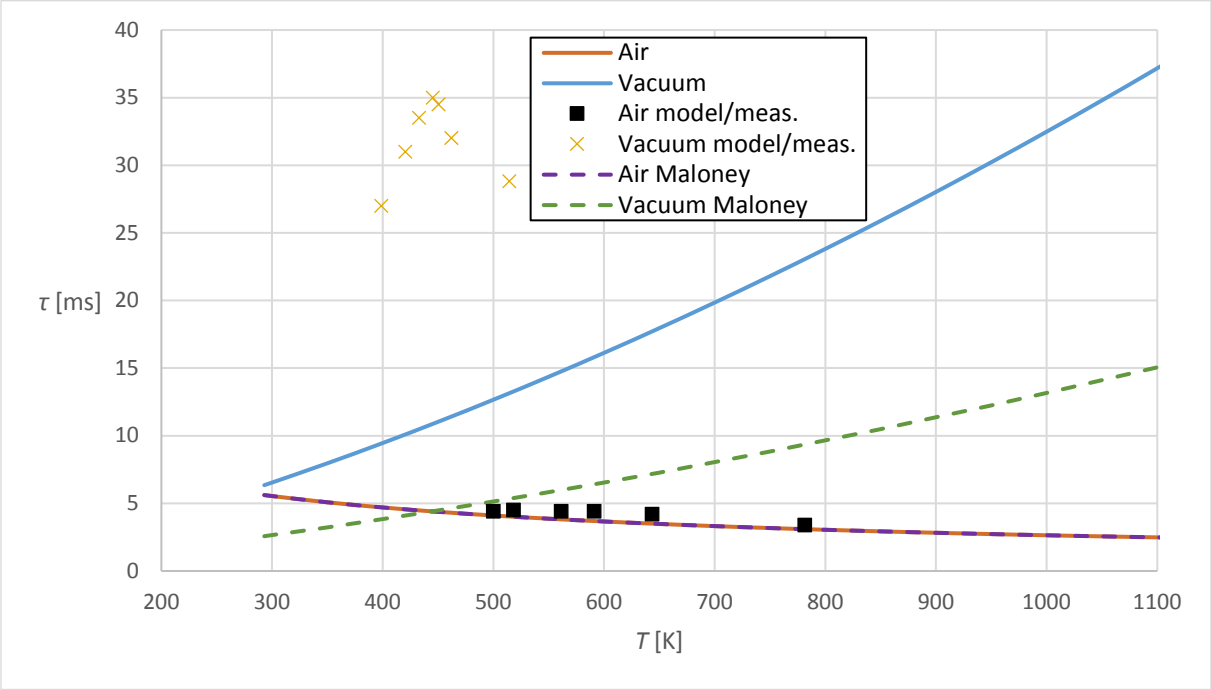

Figure 41. The measured τ as function of temperature, accompanied with the estimated τ in air and vacuum. The estimated τ is compared to the one estimated in [26].

The measured τ in air agrees with the estimated τ from appendix C and [26].

The initial resistance of the ETA at maximum shuttle displacement is $10\ \Omega$ lower in comparison to the other initial resistances. It is not understood why the resistance is less.

The power in a single ETA that is used to lock the Shuttle in all states is compared to the estimated power required for the locks (see figure 16). This is presented in table 3.

Table 3. Used and estimated power in a single ETA for Shuttle locking.

Lock	P_{used} [mW]	$P_{estimated}$ [mW]
1	662	550
2	425	400
3	555	510
4	453	440
5	579	570

It shows that the used power is higher than the estimated power, up to 20%. This indicates that the estimated stiffness of the springs is false and another equation needs to be used or that one of the models is incorrect.

The ETA beam could still be actuated after reaching the maximum shuttle displacement. The voltage over the ETA during the pulse is raised until the ETA broke to observe the reaction to a pulse of high voltage, these results are shown in figure 42.

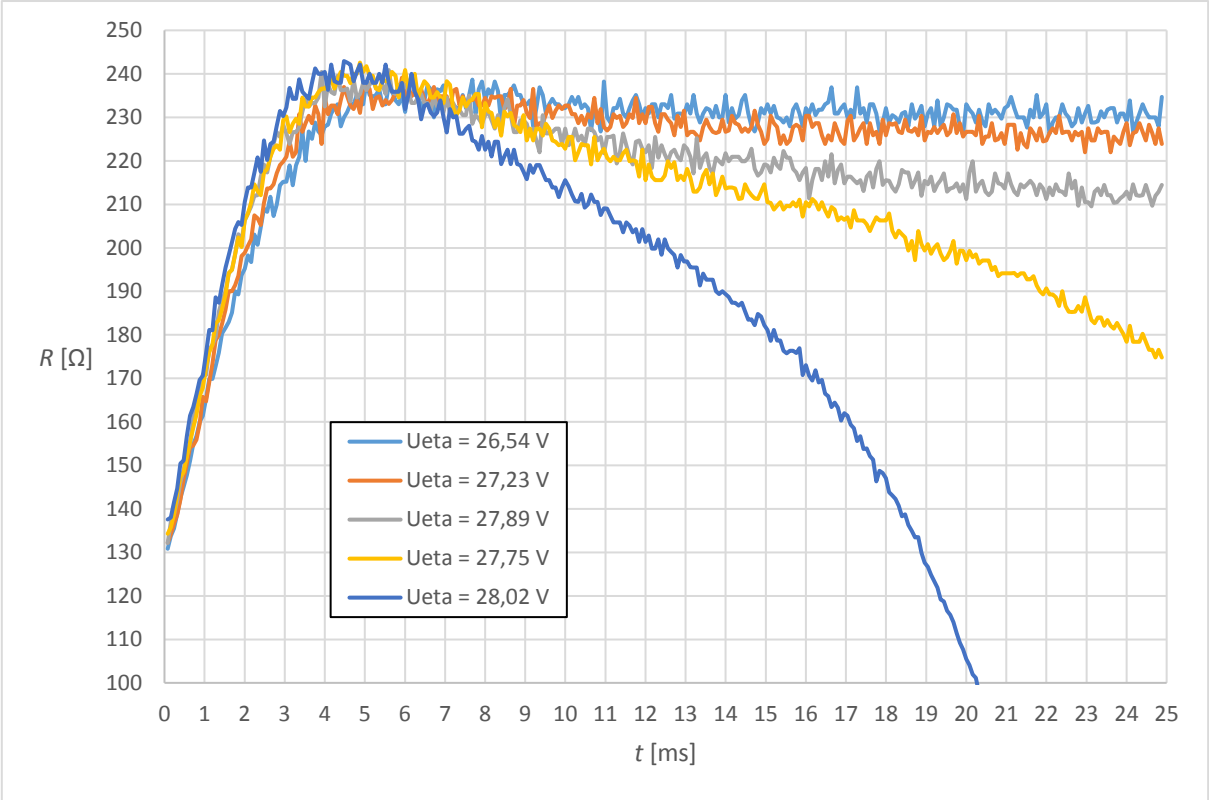

Figure 42. G1.5 #11 Q2 ETA pair, both ETA resistance vs. time (during pulse) at $p = 1000$ mbar. U_{ETA} shown in the legend is quite difficult to determine if the resistance keeps varying. This could be the explanation why U_{ETA} of the yellow line is lower than U_{ETA} of the grey line, while the opposite is expected.

It shows that at higher voltage the thermal time constant becomes less. Estimating the time constant for $U_{ETA} = 26{,}54$ V gives $\tau \approx 1{,}9$ ms. At $U_{ETA} = 26{,}54$ V the resistance slowly drops above 7 ms. By raising the voltage this effect, called Thermal-runaway, becomes stronger. The applied pulsed voltage over the ETA beam remains constant during the pulse. This means that the current through the beam must vary to maintain that voltage as the resistance of the beam varies. At a certain temperature the maximum resistivity (chapter 2.5) of the ETA beam is reached. By increasing the temperature, at the point of maximum resistivity, the resistance of the beam will drop. To maintain a constant voltage the current flowing through the beam must increase, causing the beam to heat up even more. Therefore, the resistance will drop further, which leads to an even higher current. Eventually this ends up as a vicious circle, until the ETA beam melts.
Thermal Run-away is a great example to prefer pulsed actuation over quasi-static actuation. The pulse time can restrain the Thermal Run-away. For example, the resistance of the line $U_{ETA} = 27{,}75$ V would eventually drop more, melting the ETA, if the pulse duration was longer, but is now restrained due to the pulse ending in time.

4.1.6 Pulsed G1.4 actuation measurement in vacuum

To determine the effect of lower pressure on the time constant, τ, a pulsed actuation measurement is done on the unloaded G1.4 #01 Q1 Back ETA at $p = 1{,}5 \cdot 10^{-5}$ mbar. The length of each pulse is 150 ms. The results of this measurement are presented in figure 43.

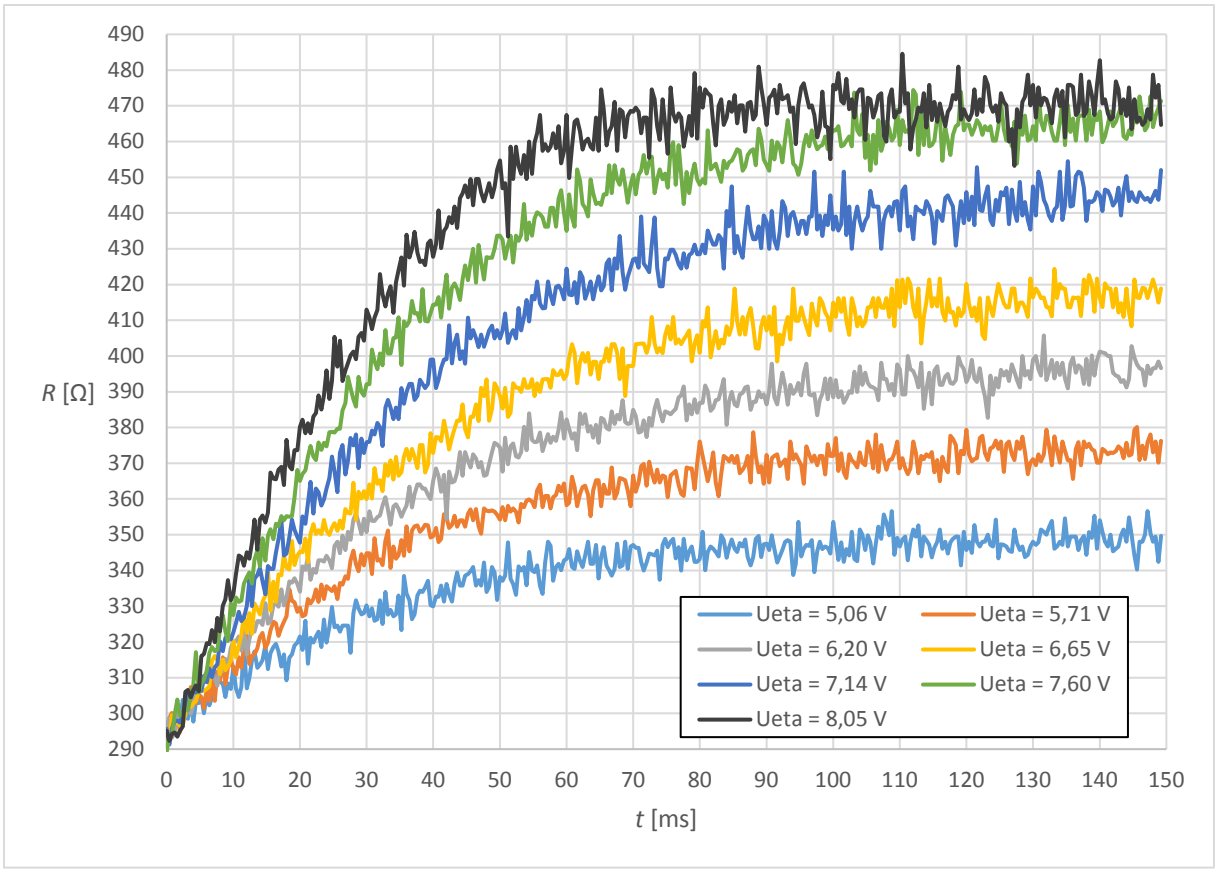

Figure 43. G1.4 #01 Q1, Back ETA resistance vs. time (during pulse) at $p = 1{,}5 \cdot 10^{-5}$ mbar. U_{ETA} shown in the legend is the average voltage over the ETA between 100 ms and 145 ms during the pulse.

The resistance shows the same dynamic behavior at low pressure and atmospheric pressure. The key difference is τ, which becomes longer at lower pressure. τ can be estimated the same way as described before, with R_e the average resistance between $t = 100$ ms and $t = 145$ ms and R_i the resistance at $t = 0$ ms. The results of τ in vacuum for the 7 pulses are shown in figure 41. The modeled/measured τ do not agree with both estimated τ. It seems as if the Electro-thermal model predicted a wrong average temperature, which could mean that the estimated resistivity does not work for vacuum modeling. Because the resistance of both the G1.5 (multiplied by 2) and G1.4 are about the same, the same temperature range is expected. Furthermore, can the deviant results be explained by a falsely estimated τ. It is quite interesting that τ drops above 450 K as both estimations predict the opposite. Lowering the pressure to $1{,}5 \cdot 10^{-5}$ mbar causes τ to be 7 times as high compared to atmospheric pressure.

4.2 Displacement measurements

The displacement measurements consist of the measured tip displacements of a single ETA, both dual and single actuation. The tip displacement is measured at atmospheric pressure and in vacuum.

4.2.1 G1.5 dual ETA, Shuttle displacement measurement without Bucket locks in air

By using all the Bucket locks the G1.5 #11 Q2 ETA pair Shuttle is locked in its 5th lock, see figure 40. To check if the Bucket locks are necessary, both ETAs of the G1.5 #11 Q4 ETA pair are actuated without turning off the voltage supply. With a constant voltage over the ETAs, they will not withdraw to the initial state, thus not locking in the Bucket locks. The results are presented in figure 44.

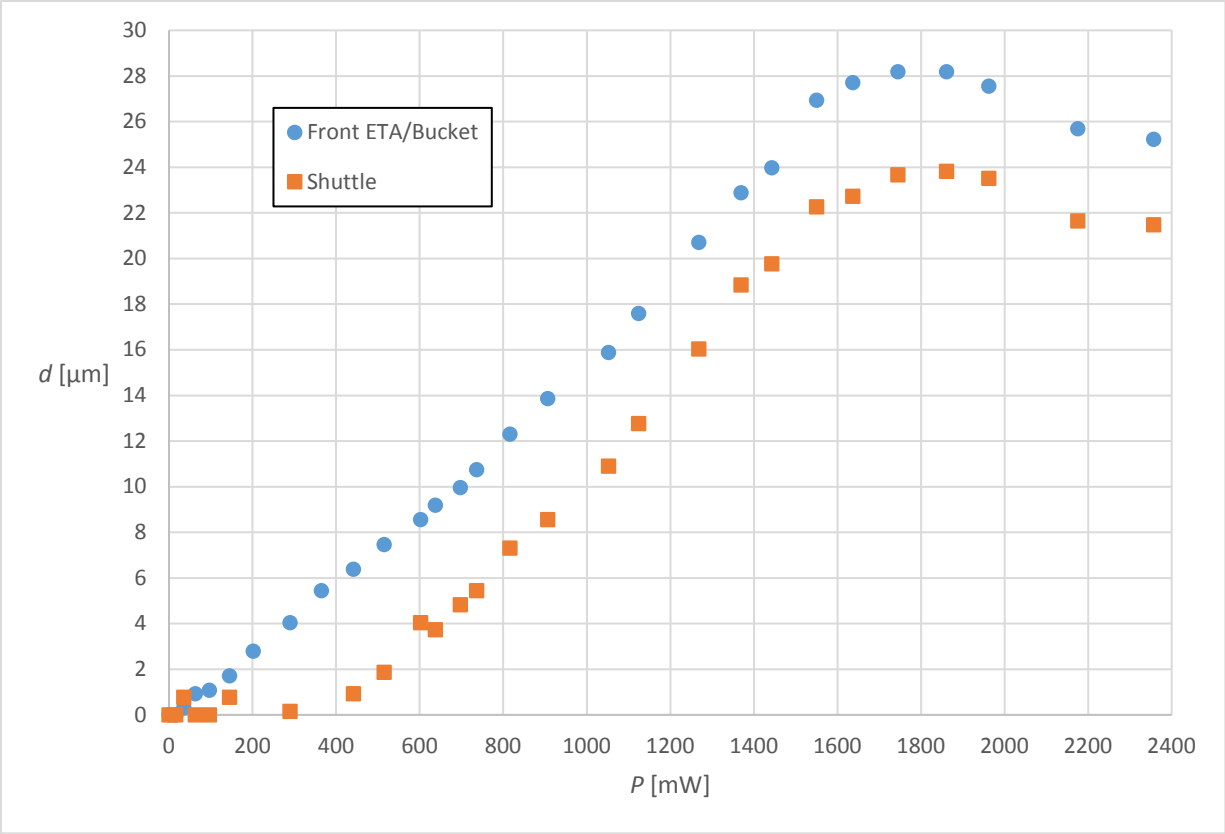

Figure 44. G1.5 #11 Q4 ETA pair, displacements versus power, with no bucket locking. The Back ETA is not photographed during this measurement and therefore not present in the graph. The maximum shuttle displacement is $23{,}84\ \mu\text{m}$, due to the buckling of the ETA beams.

It shows that it is not possible to lock the Shuttle in its 5th lock without using the Bucket locks (pumping mechanism). The maximum displacement reached by the Shuttle is $23{,}84\ \mu\text{m}$ at $1861\ \text{mW}$, locking the Shuttle in the 2nd lock. At higher power the force acting on both ETA beams becomes too high, causing the beams to buckle. The buckling is shown in figure 44 as the decrease in displacement above $1861\ \text{mW}$, for the ETA beams are deforming and pulling the Bucket back. A picture of the buckled ETA beams is shown in figure 45.

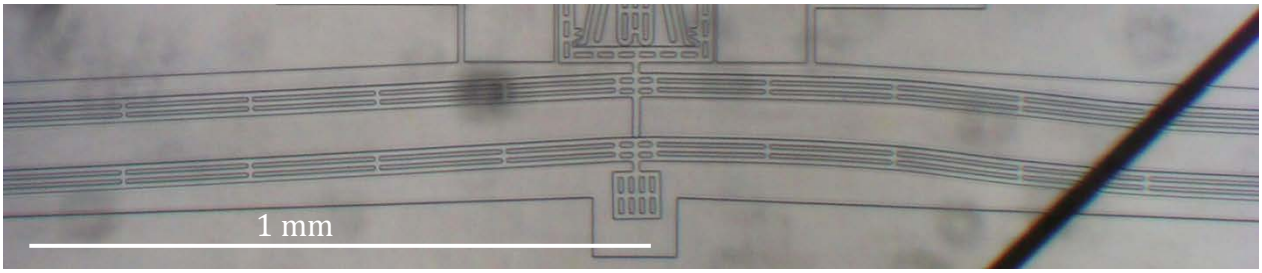

Figure 45. Buckling of the G1.5 #11 Q4 ETA pair. Without the Bucket lock do the ETA beams buckle after the 2nd Shuttle lock.

The inline force of a single ETA is calculated using the Electro-thermal and Thermo-mechanical model giving $P_0 = 141\ \text{mN}$ at $931\ \text{mW}$. This corresponds to the estimated critical load for a single ETA.

No measurement has been done while the Bucket is locked in the 1st Bucket lock. So, there could be a possibility that the curved cantilever springs can be compressed completely while using both ETA beams without the 2nd Bucket lock.

4.2.2 G1.4 Front ETA, Shuttle displacement measurement in air

The G1.4 #01 Q1 Front ETA is actuated to check if the Front ETA alone can compress the curved cantilever springs to its maximum. During this actuation all the Bucket locks are used (standard actuation). The displacement of the Front ETA is measured quasi-static until it almost locked the Shuttle in a Shuttle lock. Then, the voltage supply is turned off and the Front ETA is actuated with pulses until it locks the Shuttle. The quasi-static measurement until the Front ETA almost locks the Shuttle in the 5th Shuttle lock is presented in figure 46.

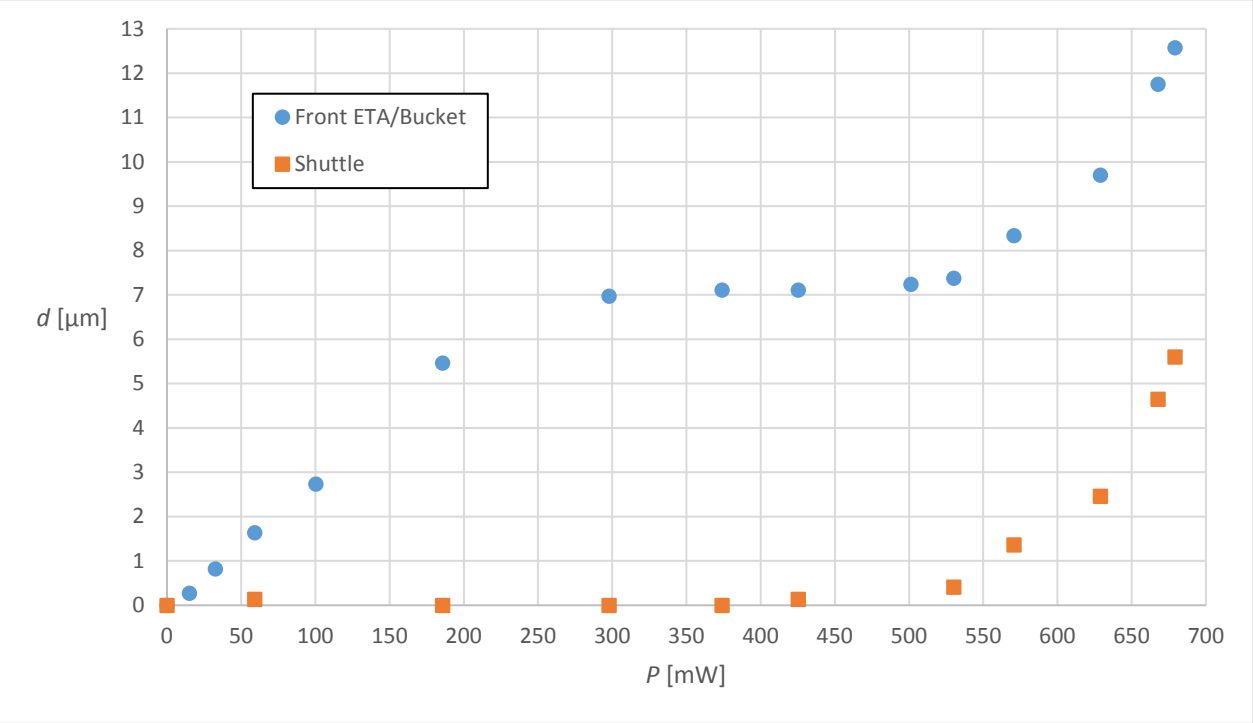

Figure 46. G1.4 #01 Q1, displacements versus power. The Bucket is locked in the 2nd Bucket lock and the Shuttle is being actuated to almost the 5th Shuttle lock.

The Shuttle is almost locked in the 5th Shuttle lock and there is no sign of buckling, meaning it could be possible to lock the Shuttle in the 5th Shuttle lock by only using the Front ETA. The Shuttle is locked in the 5th Shuttle lock using a 25 ms pulse with $U_{ETA} = 16{,}79$ V, see figure 47.

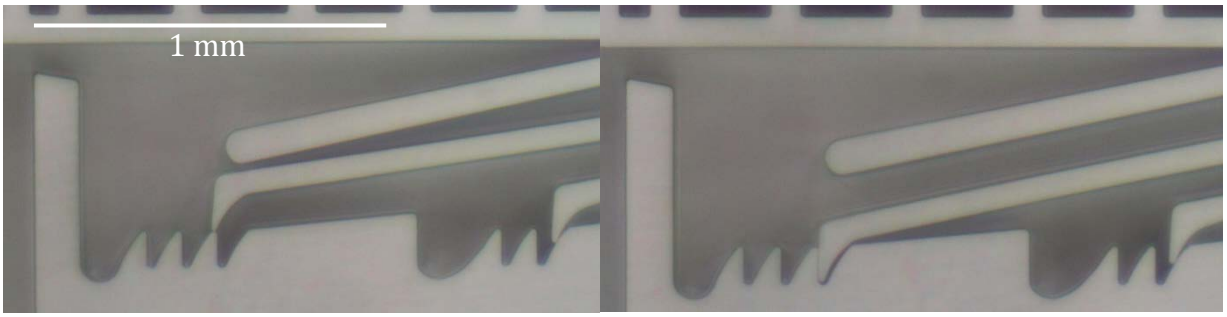

Figure 47. Locking of the Shuttle in the 5th Shuttle lock. Left: the final position of the Shuttle hooks of the quasi-static measurement shown in figure 46. Right: the Shuttle hook is locked in the 5th Shuttle lock after a 25 ms pulse with $U_{ETA} = 16{,}79$ V.

This means Back ETA is not necessary to compress the curved cantilever springs to its maximum. It can be used as a buffer so the Front ETA will not have to deal with all the force by itself. But, by removing the Back ETA there could be more space to make a firmer Front ETA that is less likely to buckle at higher forces.

As a single Front ETA is able to lock the Shuttle in the 5th Shuttle lock by using all the Bucket locks, it is interesting to know if the Front ETA can also do this by only using the 1st Bucket lock. The G1.4 #01 Q2 Front ETA is actuated quasi-statically without turning of the voltage supply. If the voltage supply is always on, the Front ETA will not withdraw and lock in the 2nd Bucket lock. The results are presented in figure 48.

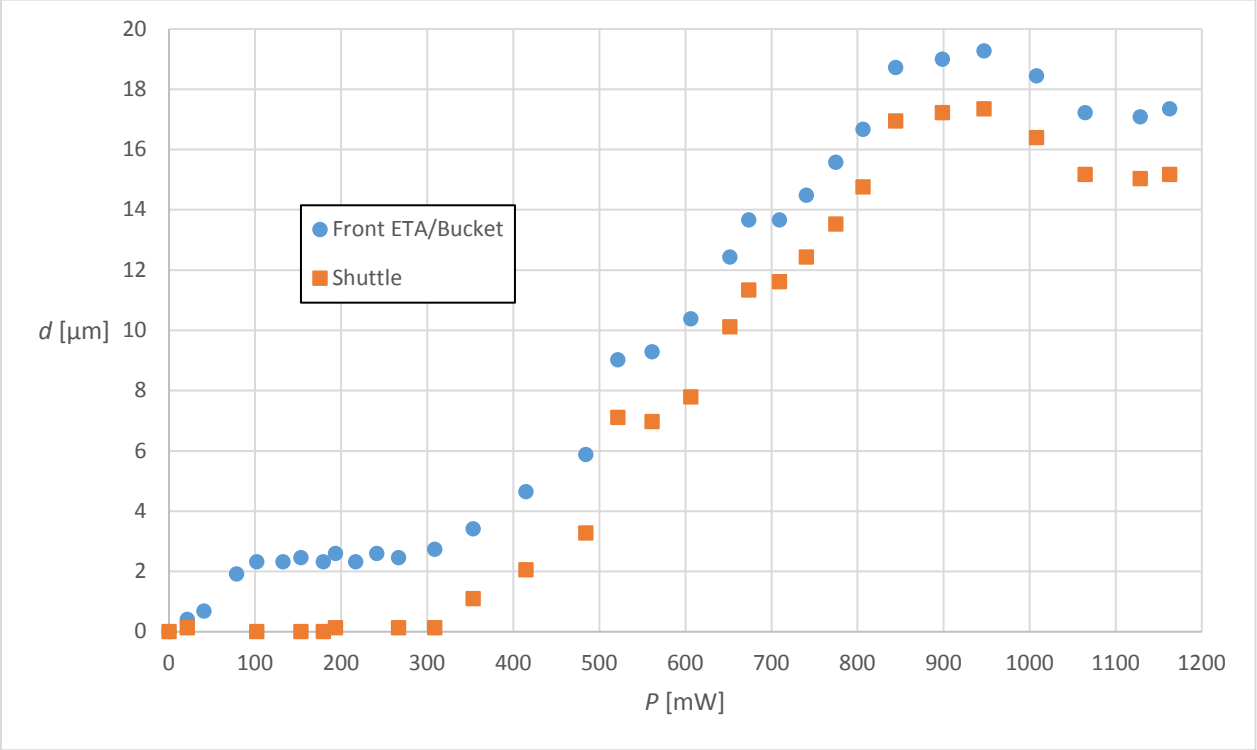

Figure 48. G1.4 #01 Q2 Front ETA, displacements versus power. The Bucket is locked in the 1st Bucket lock and the Shuttle is being actuated from the 1st to the 5th Shuttle lock. The maximum Shuttle displacement is $17{,}36\ \mu\text{m}$ from the 1st Shuttle lock, due to the buckling of the beam. The displacement 'jump' from $484\ \text{mW}$ to $521\ \text{mW}$ is caused by "stick slip". Due to the rough surface of silicon do the Shuttle hooks have friction when touching the Shuttle locks. Sometimes this causes the Shuttle to get stuck. When enough force is applied the Shuttle will be pushed over the rough surface until the friction becomes less. At that point does the Shuttle suddenly 'jumps' to a new position.

Without the 2nd Bucket lock it is not possible lock the Shuttle in the 5th Shuttle lock. The Front ETA buckled after the 4th Shuttle lock. The maximum Shuttle displacement reached, from the 1st Shuttle lock, is $17{,}36\ \mu\text{m}$ at $947\ \text{mW}$. The inline force is calculated using the Electro-thermal and Thermo-mechanical model giving $P_0 = 142\ \text{mN}$. This corresponds to the estimated critical load for a single ETA. Comparing to the in chapter 4.2.1 calculated inline force, both values are about the same. This gives an average inline force of $P_0 = 142\ \text{mN}$, rounded up, at $939\ \text{mW}$.

4.2.3 G1.4 Back ETA displacement measurement in air and vacuum

Buckling of the ETA beams occurs when a force acts upon them. The force from the curved cantilever springs, the Shuttle suspension and Bucket suspension (see chapter 2.2.1) all contribute to the force acting on the Beams. By destroying the Front ETA, the Back ETA has no external force acting upon it. This means the Back ETA can expand to its maximum until it melts. The displacement as function of power of the G1.4 #01 Q3 and Q2 Back ETA is measured at atmospheric pressure and in vacuum respectively. These results are presented in figure 49.

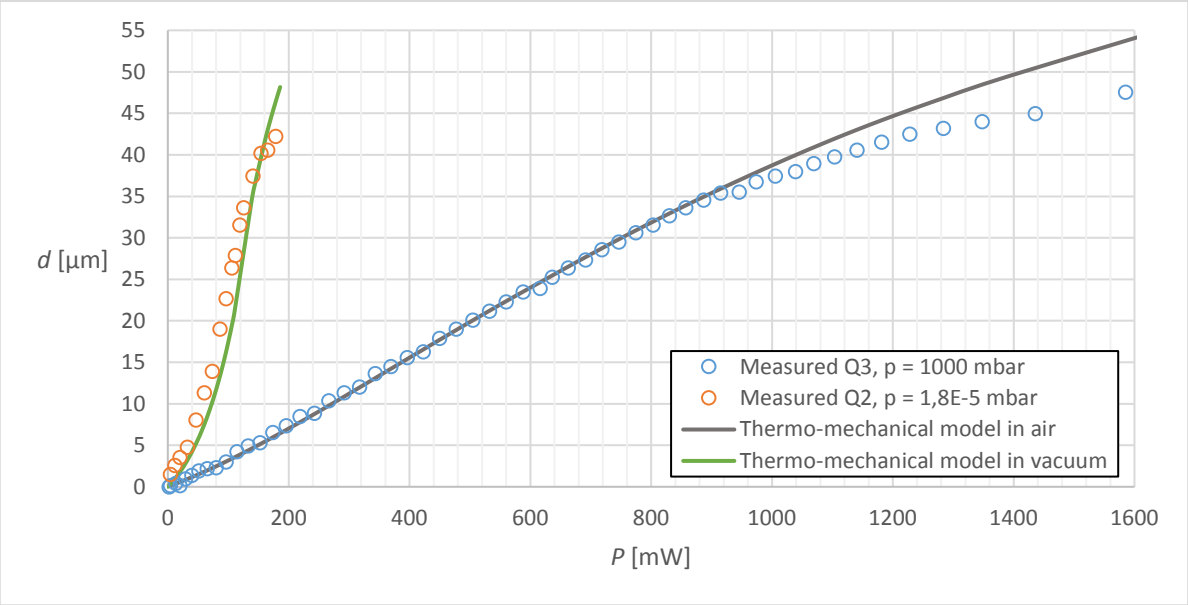

Figure 49. G1.4 #01 Q3 and Q2 Back ETA displacement versus power at different pressures, accompanied with the Thermo-mechanical model results for a single ETA at atmospheric pressure and in vacuum.

The displacement in vacuum needs significantly less power (about 10 times less) than at atmospheric pressure. The low power requirement come with the disadvantage that a slight offset in the power effects the displacement more than it would at atmospheric pressure.

4.3 Model comparison

The measurements from figure 39 and figure 49 compared to the model, because these are the most complete quasi-static measurements of a single ETA. It is required to know the resistivity of the silicon for the Electro-thermal model, because this is crucial for the heat generation inside the beam. Because there is no information on the resistivity of the used silicon, figure 39 is used to estimate the resistivity of the used silicon. The measured contact and extra silicon piece resistance are subtracted from the total measured Back ETA resistance. It is assumed that these small resistances do not depend on temperature and will therefore negatively influence the resistivity estimation. It is attempted to match the Back ETA resistance, after subtraction, as function of power as good as possible, with the data at $p = 1000$ mbar, using the Electro-thermal model in Excel.

The estimated resistivity of the used silicon is shown in figure 50 and table 6 in appendix B.1.4.

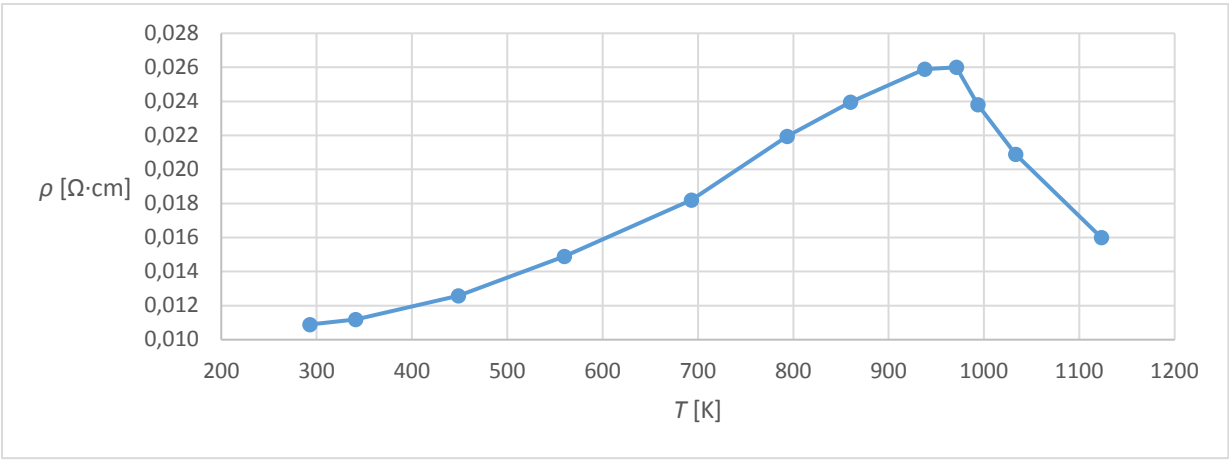

Figure 50. Estimated silicon resistivity versus temperature. The resistivity is estimated by matching the resistance as much as possible in the model with figure 39.

The resistance as function of power that is obtained from the model is shown in figure 39. It shows that the modeled values are in agreement with the measured results. The resistance obtained from the model holds better for the measurement in air than in vacuum, as is expected due to the matching operation done to find the temperature dependence of the resistivity. The maximum difference between modeled resistance and measurement in vacuum is about $40\ \Omega$. It is possible that the heat conduction through air in the Electro-thermal model has effected the estimated resistivity. A better model could be made if the resistivity is estimated for an ETA in vacuum instead of air.

The Thermo-mechanical model requires an average temperature increase as input, if the thermal expansion coefficient is constant. This is not the case for the used silicon, see appendix B.1.3, so, the average of the thermal expansion coefficient multiplied with the temperature increase at point x $\left(\overline{\alpha(T)\cdot\Delta T(x)}\right)$ on the beam is used as input. The model results in the tip displacement of the Back ETA versus power at $p = 1000\ \mathrm{mbar}$ and $p = 1{,}8\cdot 10^{-5}\ \mathrm{mbar}$, shown in figure 49. The models and the measurement data show that the displacement is a S-shape curve. The Thermo-mechanical model in air agrees with the measurement results till $35{,}4\ \mu\mathrm{m}$ at $915\ \mathrm{mW}$. At powers above $915\ \mathrm{mW}$ and in vacuum does the model not completely agreement with the measurement results. Nevertheless, does the model give a good estimation of the displacement as function of power and do the modeled results show the same curve as the measured values. The deviant modeled results could possibly be a result of an incorrect estimated resistivity and/or chosen $I_{x,eff}$. At $p = 1000\ \mathrm{mbar}$ could the Back ETA have lost some of its heat to the remains of the Front ETA when coming closer to it, see figure 51, resulting in less displacement.

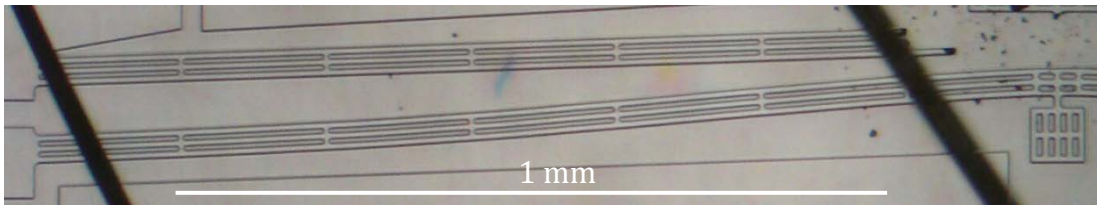

Figure 51. G1.4 #01 Q3 ETA pair. The Back ETA comes closer to the Front ETA, which causes heat transfer from the Back ETA to the remains of the Front ETA. Picture taken at $P = 1{,}35$ W.

The used thermal conductivity of silicon is for silicon without doping. It could be possible that the doped silicon has a different thermal conductivity than non-doped silicon, which could explain the deviating model results. Besides this, an unknown factor that has an effect on the displacement could have been absent from the Thermo-mechanical model.

5 Further observations

This chapter presents any further observations that are done during the resistance and displacement measurements.

5.1 ETA beam vibration

The Front ETA, from the G1.4 #01 Q1 ETA pair, is actuated with pulses, till it could not push the Shuttle any further, after it reached the 5th Shuttle lock. At $U_{ETA} = 17{,}39$ V the Front ETA vibrated, see figure 52.

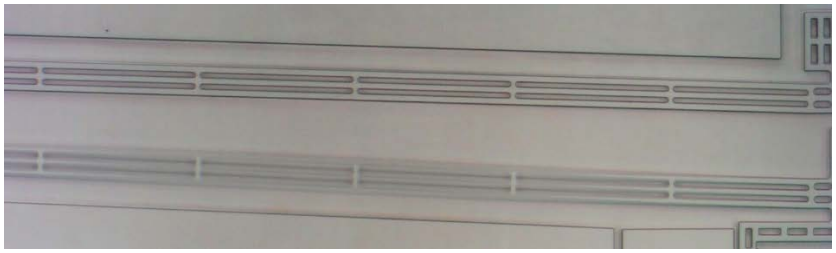

Figure 52. Vibration of the Front ETA at $U_{ETA} = 17{,}39$ V.

It seems as if the Front ETA is at the point where it begins to buckle. The high temperature of the ETA causes it to expand, as it comes closer to the substrate more heat is transferred from the ETA to the substrate causing it to cool down and compress. Therefore less heat can be transferred to the substrate, so the ETA heats up again. This process is continued till the power dissipated in the ETA is changed by a lower or higher voltage. At higher voltage the Front ETA buckles in the 2nd mode, see figure 53. It is possible that the vibration of the Front ETA is the indication for the beginning of the buckling. The connection point between the Front ETA and the Bucket is rotating due to the buckling. By adding two extra connection points to the Front ETA, the rotation could be prevented, making the ETA more able to withstand the 2nd mode buckling.

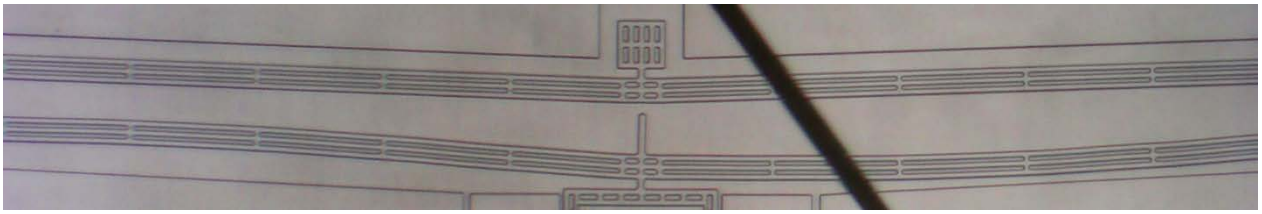

Figure 53. The 2nd mode buckling of the Front ETA at $U_{ETA} = 21{,}06$ V.

5.2 Local buckling

The silicon ETA beams plastically deform at temperatures above 900 K [27]. These deformations cannot be reversed and makes the ETAs not function anymore. Part of plastic deformation is the local buckling of the beam. This is observed at the G1.5 #11 Q2 ETA pair, when the ETAs were being actuated till they broke, see figure 54.

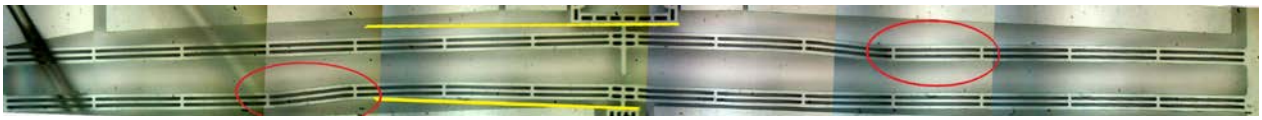

Figure 54. The local buckling in both ETAs at $U_{ETA} > 27\ V$.

The critical local buckling load on a single sub-beam can be calculated using the critical load equation for a beam shown in figure 55, which is:

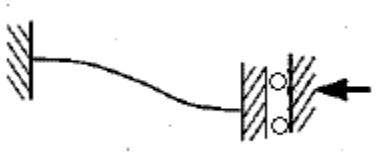

Figure 55. Schematic of the beam fixed on one end and translation free on the other [28].

$$P_0 = \frac{\pi^2 E I_x}{{L_b}^2} \tag{5.1}$$

For a single sub-beam at room temperature with $L_b = 206\ \mu\text{m}$ and $I_x = 2{,}1 \cdot 10^{-21}\ \text{m}^4$, gives equation (5.1): $P_0 = 84\ \text{mN}$. Meaning that for three sub-beams $P_0 = 253\ \text{mN}$, which is higher than the critical second mode buckling load, so local buckling will happen after second mode buckling. To reduce the local buckling effect, the support beams could be placed under an angle, see figure 56. The force acting upon the support beams will be better distributed, reducing the effect of local buckling.

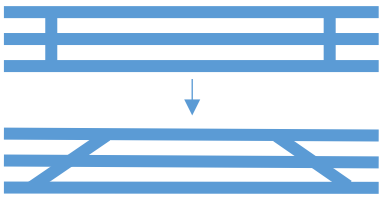

Figure 56. Possible support beam design to prevent local buckling.

5.3 Unactuated Back ETA displacement

During the quasi-static actuation of the G1.4 #01 Q1 Front ETA, the Back ETA displaced $1{,}50\ \mu\text{m}$ at a dissipated power in the Front ETA of $572\ \text{mW}$. This indicates that heat is transferred from the Front ETA to the Back ETA. During dual ETA actuation this is very beneficial, due to the reduced (electrical) power that is needed to displace the Back ETA.

5.4 ETA beam glowing

The G1.4 #01 Q2 Back ETA, is measured in vacuum till it reached its maximum displacement. At $P_{ETA} = 186\ \text{mW}$ the ETA has a red glow, shown in figure 57.

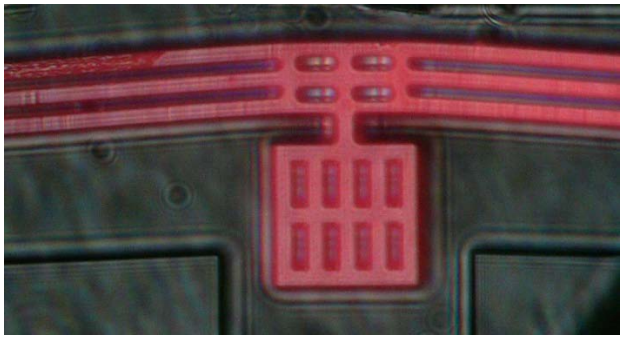

Figure 57. Red glowing of the Back ETA in vacuum at $P_{ETA} = 186\ \text{mW}$.

At this point the displacement of the Back ETA became less, which indicates that the ETA is buckling. Because of the high temperature of the ETA the buckling resulted in the plastic deformation of the ETA

6 Conclusions

Measurement of the ETA resistance as a function of the electrical power combined with the Electro-thermal quasi-static numerical model in air, allows estimation of the highly boron doped silicon ($\sim 6 \cdot 10^{18}$ atoms/cm^3) as a function of temperature up to 1123 K. The resulting resistivity curve shows a peak at 971 K, and fits well within corresponding curves for other doping levels. The modeled and measured resistance in vacuum have a maximum difference of about $40\ \Omega$.

From the voltage step response, τ as function of temperature in air and vacuum are obtained. Measurements in air agreed with the estimated τ. The order of magnitude for the measurements in vacuum agree with the estimated τ. The measured τ in vacuum are higher than in air, which is expected. The calculated temperature dependency of τ in vacuum does not agree with the estimated τ as function of temperature.

The contact resistance measurement as function of power shows a decreasing resistance when increasing the power. This nonreversible effect can decrease the contact resistance from $80\ \Omega$ to $5\ \Omega$ over a power range up to 1300 mW. The resistance varies mutually between the contest resistances. The average measured contact resistance at room temperature on the G1.4 MEMS device is $5{,}21\ \Omega$. It is thought that the difference in contact resistance at room temperature of the G1.4 and G1.5 is due to the time between arrival and bonding is shorter for the G1.4, causing the G1.5 to have thicker insulating layer.

Quasi-static and dynamic actuation measurements provide the tip displacement of both single and dual (parallel) actuated ETA systems as a function of applied power, both for mechanically unloaded ETAs and a range of increasing spring-loaded ETAs, up to the plasticity and buckling limits. This has shown that the complete Shuttle locking procedure can be done with only a single ETA, if the complete pumping system is used. This means that dual ETA actuation is not necessary for complete curved cantilever spring compression.

The results of the Thermo-mechanical quasi-static analytical model in air agree with the measurements for an unloaded single ETA, up to a maximum tip displacement of $35{,}4$ μm at 915 mW.

The measured power for spring-loaded ETAs needed to reach each Shuttle lock, were measured to be up to 20% higher than estimated.

The critical buckling load of a single ETA is calculated for the power at which buckling is observed to be 142 mN at 939 mW. This corresponds to the estimated value of 149 mN. Similarly, it is estimated that the local buckling will occur at 252 mN inline force. It is assumed that this estimation is correct, because the calculated critical load for second mode buckling corresponds to the estimated one. The critical local buckling load is higher than the critical buckling load, so local buckling will happen after second mode buckling.

It is observed that a Back ETA receives heat from an actuated Front ETA. When a power of 572 mW is dissipated in only the Front ETA, the Back ETA displaced $1{,}5$ μm.

7 Discussion and suggestions

All the future ETAs should be bonded with two bonding wires on every bonding pad. By doing this, the ETAs can be measured using 'Four-terminal sensing'. This technique is used to measure resistance accurately without the resistances of the wires and contact resistances (if constant and mutually the same) effecting the measurement.

The contact resistance as function of all its dependencies should be understood. It should be measured at what power the irreversible effect of the contact resistances appears and when the contact resistances have the lowest value. Then, the required power can be applied over the contacts to reduce the contact resistance, so it will have less effect on the ETA resistance. Beside this, could the information gathered from those measurement possibly describe deviant ETA resistance phenomena.

The Back ETA actuation is effected by the remains of the Front ETA. To have a complete unaffected measurement of the resistance and the displacement of the Back ETA, a MEMS design should be made with only one ETA to push the Shuttle or one separate unloaded ETA. Such a design would decrease the amount of heat that is lost to the surroundings, thus giving a better characterization of a single ETA only.

The resistivity temperature dependence of highly doped silicon is estimated indirectly using the Electro-thermal model. This estimation is a matching operation between the model and the measured values and comes with inaccuracies, because the assumed to be correct material properties could be false. This could explain the $40\ \Omega$ difference in modeled and measured resistance of vacuum. This encourages a direct measurement of the resistivity, which can be done by placing a MEMS device in a temperature controlled oven and measure its resistance using Four-terminal sensing. The challenge of this measurement is connecting a suitable wire that does not melt before silicon melts.

The Back ETA design has a heat sink at the tip. The models are made for a simple uniform beam. For a more accurate estimation of the behavior of a single ETA should the heat sink be added to the model.

An ETA exchanges heat to the surroundings (other ETA, Bucket, etc.), besides the substrate. The Electro-thermal model should be improved by adding an extra heat loss factor, which takes the heat exchange to the surroundings into account.

The current model for thermal time constant estimation has some deviancies when modeling for a vacuum situation. Therefore, a better, more complete model of the thermal time constant of a beam should be made.

8 References

[1] A. Einstein, "Näherungsweise Integration der Feldgleichungen der Gravitation," *Sitzungsberichte der Königlich Preussischen Akademie der Wissenschaften Berlin,* pp. 688-696, 22 June 1916.

[2] "Special Breakthrough Prize for detection of gravitational waves," 3 May 2016. [Online]. Available: https://www.nikhef.nl/nieuws/special-breakthrough-prize-for-detection-of-gravitational-waves/.

[3] B. P. Abbott et al., "Observation of Gravitational Waves from a Binary Black Hole Merger," *Physical Review Letters,* 11 February 2016.

[4] Aspera, [Online]. Available: http://www.aspera-eu.org/images/stories/Media/MEDIAPICTURES/HR/virgo.jpg. [Accessed 11 July 2017].

[5] Virgo, "The Virgo interferometer," [Online]. Available: http://www.ego-gw.it/virgodescription/pag_4.html.

[6] M. G. Beker, Low-frequency sensitivity of next generation gravitational wave detectors, Amsterdam: Ipskamp Drukkers, 2013.

[7] W. R. Thurber, R. L. Mattis, Y. M. Liu and J. J. Filliben, "Semiconductor Measurement Technology: The Relationship Between Resistivity and Dopant Density for Phosphorus- and Boron-Doped Silicon," National Bureau of Standards, Washington, DC, 1981.

[8] R. A. Brookhuis, "Big mass accelerometer - G5 process document and fabrication results," University Of Twente, Twente, 2016.

[9] E. Hennes, A. Bertolini and J. F. Van Den Brand, "MEMS Sensor Structure Comprising Mechanically Preloaded Suspension Springs". The Netherlands Patent 185222 Al, 6 June 2014.

[10] V. Amit, "First three modes of buckling loads," 17 June 2016. [Online]. Available: https://en.wikipedia.org/wiki/Euler%27s_critical_load#/media/File:FIG4.png. [Accessed 20 April 2017].

[11] J. M. Maloney, D. L. DeVoe and D. S. Schreiber, "Analysis and Design of Electrothermal Actuators Fabricated from Single Crystal Silicon," *Proc. MEMS 2000,* pp. 233-240, 2000.

[12] E. T. Enikov, S. S. Kedar and K. V. Lazarov, "Analytical and Experimental Analysis of Folded Beam and V-shaped Thermal Microactuators," University of Arizona, Tucson, 200X.

[13] R. A. Powell and S. B. Felch, "Semiconductor Wafer Temperature Measuring Device and Method". United States of America Patent 0252697A2, 1988.

[14] P. W. Chapman, O. N. Tufte, J. D. Zook and D. Long, "Electrical Properties of Heavily Doped Silicon," *Journal of Applied Physics,* vol. 34, no. 11, pp. 3291-3295, 1963.

[15] M. S. Baker, R. A. Plass, T. J. Headley and J. A. Walraven, "Compliant Thermo-Mechanical MEMS Actuators LDRD #52553," Sandia National Laboratories, Albuquerque, 2004.

[16] C. H. Liebert and R. D. Thomas, "Spectral Emissivity Of Highly Doped Silicon," NASA, Washington, 1968.

[17] MECH-EL INDUSTRIES, INC., "MECH-EL / MEI 907," MECH-EL INDUSTRIES, INC., 2009. [Online]. Available: http://www.mech-el.com/907.htm. [Accessed 19 June 2017].

[18] Tabor Electronics, "Model 8500," Tabor Electronics, 2017. [Online]. Available: http://www.taborelec.com/8500. [Accessed 8 July 2017].

[19] Tektronix, "TDS3000 Series Digital Phosphor Oscilloscopes," [Online]. Available: http://web.mit.edu/6.101/www/reference/TDS3000Manual.pdf. [Accessed 19 June 2017].

[20] Future Optics, "MDC2000 multi-purpose LCD microscope camera with relay lens," Future Optics, 2014. [Online]. Available: http://www.future-optics.com/product/html/43.html. [Accessed 19 June 2017].

[21] Motic, "Moticam BTU10," Motic, 2017. [Online]. Available: http://www.motic.com/Am_MoticamTablet/product_772.html. [Accessed 19 June 2017].

[22] Pfeiffer Vacuum, "HiPace® 80 with TC 110, DN 63 ISO-K," Pfeiffer Vacuum, 2017. [Online]. Available: https://www.pfeiffer-vacuum.com/en/products/turbopumps/hybrid-bearing/hipace-80/?detailPdoId=4512. [Accessed 21 June 2017].

[23] Edmund Optics, "50mm Dia. UV-VIS Coated, 1λ Fused Silica Window," Edmund Optics, 2017. [Online]. Available: https://www.edmundoptics.eu/optics/windows-diffusers/visible-windows/50mm-dia.-uv-vis-coated-1lambda-fused-silica-window/. [Accessed 21 June 2017].

[24] Pfeiffer Vacuum, "MPT 200 AR, DN 25 ISO-KF, RS-485, analog," Pfeiffer Vacuum, 2017. [Online]. Available: https://www.pfeiffer-vacuum.com/en/products/measurement/digiline/gauges/?detailPdoId=13250. [Accessed 21 June 2017].

[25] "Mean free path," Pfeiffer, April 2013. [Online]. Available: https://www.pfeiffer-vacuum.com/en/know-how/introduction-to-vacuum-technology/fundamentals/mean-free-path/. [Accessed 16 June 2017].

[26] J. M. Maloney, D. S. Schreiber and D. L. DeVoe, "Large-force electrothermal linear mircromotors," *Journal of Micromechanics and Microengineering,* vol. 14, no. 2, pp. 226-234, 2004.

[27] C. J. Gallagher, "Plastic Deformation of Germanium and Silicon," *Physical Review,* vol. 88, no. 4, pp. 721-722, 1952.

[28] J. Doshi, "Why does buckling occur in columns?," 12 November 2015. [Online]. Available: https://www.quora.com/Why-does-buckling-occur-in-columns. [Accessed 11 July 2017].

[29] S. Pemberton, "Bending moments and beam curvatures," April 2008. [Online]. Available: https://www.doitpoms.ac.uk/tlplib/beam_bending/bend_moments.php. [Accessed 14 June 2017].

[30] efunda, "Thermal Conductivity: Silicon," efunda, 2017. [Online]. Available: http://www.efunda.com/materials/elements/TC_Table.cfm?Element_ID=Si. [Accessed June 2017].

[31] N. Ono, K. Kitamura, K. Nakajima and Y. Shimanuki, "Measurement of Young's modulus of silicon single crystal at high temperature and its dependency on boron concentration using the flexural vibration method," *Japanese Journal of Applied Physics, Part 1: Regular Papers and Short Notes and Review Papers,* vol. 39, no. 2A, pp. 368-371, 2000.

[32] R. Hull, Properties of Crystalline Silicon, London: INSPEC, 1999.

[33] J. H. Lienhard and J. H. Lienhard, A Heat Transfer Textbook, 4th ed., Cambridge, Massachusetts: Phlogiston Press, 2017.

[34] E. E. Shpilrain, "Air (Properties of)," 3 February 2011. [Online]. Available: http://www.thermopedia.com/content/553/. [Accessed June 2017].

[35] F. P. Incropera and D. P. DeWitt, Introduction to heat transfer, 2nd ed., New York: J. Wiley, 1990.

[36] R. Kojima Endo, Y. Fujihara and M. Susa, "Calculation of density and heat capacity of silicon by molecular dynamics simulation," Tokyo Institute of Technology, Tokyo, 2003.

A Appendix: Derivations

This appendix will describe the derivations of some of the used equations in this report.

A.1 Accelerometer response derivation

A schematic representation of an accelerometer is shown in figure 58.

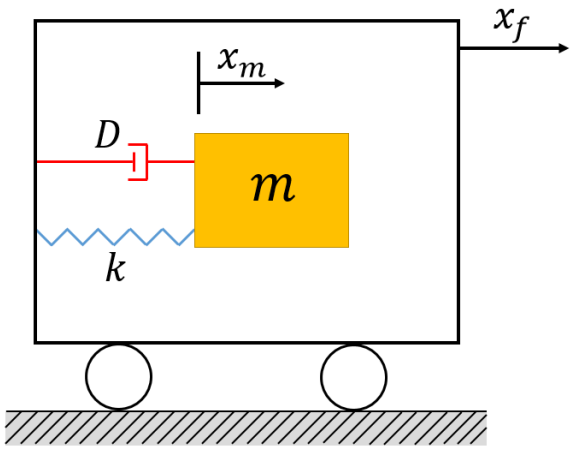

Figure 58. Schematic representation of an accelerometer.

The mass inside the frame will be moved by an acceleration of the frame. The relative displacement x_{rel} of the mass can be described as the displacement of the frame x_f subtracted from the displacement of the mass x_m: $x_{rel} = x_m - x_f$. Newton's law of motion

$$ma = \Sigma F \tag{A.1}$$

shows that the acceleration of the mass is due to the damping force and the spring force, giving:

$$m_a \ddot{x}_m = -k_a x_{rel} - D_a \dot{x}_{rel} \tag{A.2}$$

Rewriting equation (A.2) gives:

$$m_a \cdot \left(\ddot{x}_{rel} + \ddot{x}_f\right) = -k_a x_{rel} - D_a \dot{x}_{rel} \tag{A.3}$$

Solving differential equation (A.3) for harmonic motion, $x = \hat{x} \cdot e^{i\omega t}$, gives:

$$m_a \cdot \left(-\omega^2 \cdot \hat{x}_{rel} + \hat{\ddot{x}}_f\right) \cdot e^{i\omega t} = -k_a \hat{x}_{rel} \cdot e^{i\omega t} - i\omega D_a \hat{x}_{rel} \cdot e^{i\omega t} \tag{A.4}$$

Dividing equation (A.4) by m_a and $e^{i\omega t}$, gives:

$$-\omega^2 \cdot \hat{x}_{rel} + \hat{\ddot{x}}_f = -{\omega_0}^2 \cdot \hat{x}_{rel} - i\omega \cdot \Delta\omega \cdot \hat{x}_{rel} \tag{A.5}$$

Factorizing equation (A.5) gives:

$$\hat{\ddot{x}}_f = \hat{x}_{rel} \cdot (-{\omega_0}^2 - i\omega \cdot \Delta\omega + \omega^2) \tag{A.6}$$

Rewriting equation (A.6) gives:

$$\frac{\hat{x}_{rel}}{\hat{\ddot{x}}_f} = \frac{1}{(\omega^2 - {\omega_0}^2) - i\omega \cdot \Delta\omega} \tag{A.7}$$

Equation (A.7) can be multiplied by $\frac{-\frac{1}{{\omega_0}^2}}{-\frac{1}{{\omega_0}^2}}$, giving:

$$\frac{\hat{x}_{rel}}{\hat{\ddot{x}}_f} = -\frac{1}{{\omega_0}^2} \cdot \frac{1}{\left(1 - \frac{\omega^2}{{\omega_0}^2}\right) + \left(\frac{i\omega \cdot \Delta\omega}{{\omega_0}^2}\right)} \tag{A.8}$$

Absolute values of equation (A.8) give the response of the accelerometer:

$$\left|\frac{\hat{x}_{rel}}{\hat{\ddot{x}}_f}\right| = \frac{1}{{\omega_0}^2} \cdot \frac{1}{\sqrt{\left(1 - \frac{\omega^2}{{\omega_0}^2}\right)^2 + \left(\frac{\omega \cdot \Delta\omega}{{\omega_0}^2}\right)^2}} \tag{A.9}$$

A.2 Spring profile derivation

The forces acting upon a curved cantilever spring are shown in figure 59.

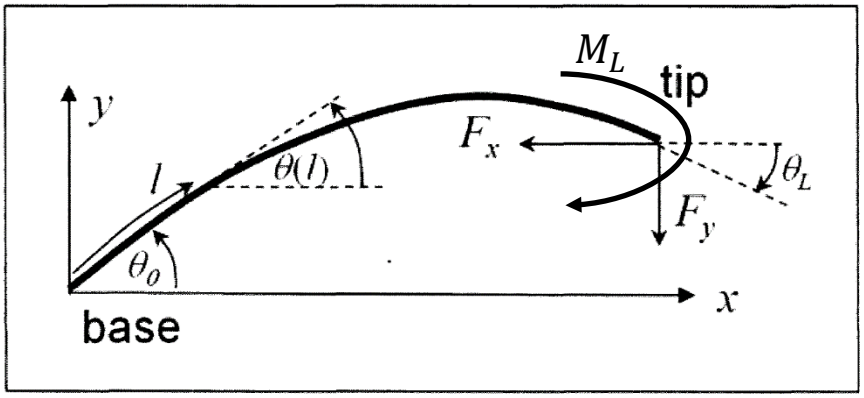

Figure 59. Schematic of a curved cantilever spring. [9]

A profile of a single curved cantilever spring can be set up by an expression for the moment along a curvilinear axis, l, on the spring, see figure 59. The expression for the moment along the l-axis is:

$$M(l) = -F_y \cdot \big(x_L - x(l)\big) + F_x \cdot \big(y_L - y(l)\big) - M_L \tag{A.10}$$

The Euler beam theory gives the total moment along the l-axis:

$$M(l) = EI_x \cdot \frac{d^2 w(l)}{dl^2} \tag{A.11}$$

For small angles the spring makes with the x-axis, is the angle approximately equal to the slope, $\frac{dw}{dl}$, of the spring. Applying this to equation (A.11) gives:

$$M(l) = EI_x \cdot \left(\frac{d\theta(l)}{dl} - \frac{d\theta_0}{dl}\right) \tag{A.12}$$

Combining equation (A.12) and (A.10) give a differential equation:

$$EI_x \cdot \frac{d\theta(l)}{dl} - EI_x \cdot \frac{d\theta_0}{dl} = -F_y \cdot \big(x_L - x(l)\big) + F_x \cdot \big(y_L - y(l)\big) - M_L \tag{A.13}$$

Differentiating equation (A.13) removes the constants, giving:

$$EI_x \cdot \frac{d^2\theta(l)}{dl^2} = F_y \cdot \frac{dx(l)}{dl} - F_x \cdot \frac{dy(l)}{dl} \tag{A.14}$$

The relation between the y-axis and x-axis to the l-axis are:

$$\begin{aligned} dx &= dl \cdot \cos\big(\theta(l)\big) \\ dy &= dl \cdot \sin\big(\theta(l)\big) \end{aligned} \tag{A.15}$$

Combining equation (A.14) and (A.15) give:

$$\frac{d^2\theta(l)}{dl^2} = \frac{F_y \cdot \cos(\theta(l)) - F_x \cdot \sin(\theta(l))}{EI_x} \tag{A.16}$$

A.3 Electro-Thermal model derivation

A.3.1 Numerical

The heat transfer of a clamped-clamped beam is described schematically in figure 60. Heat loss by radiation is neglected, because heat loss to the substrate has more contribution to the heat transfer than radiation.

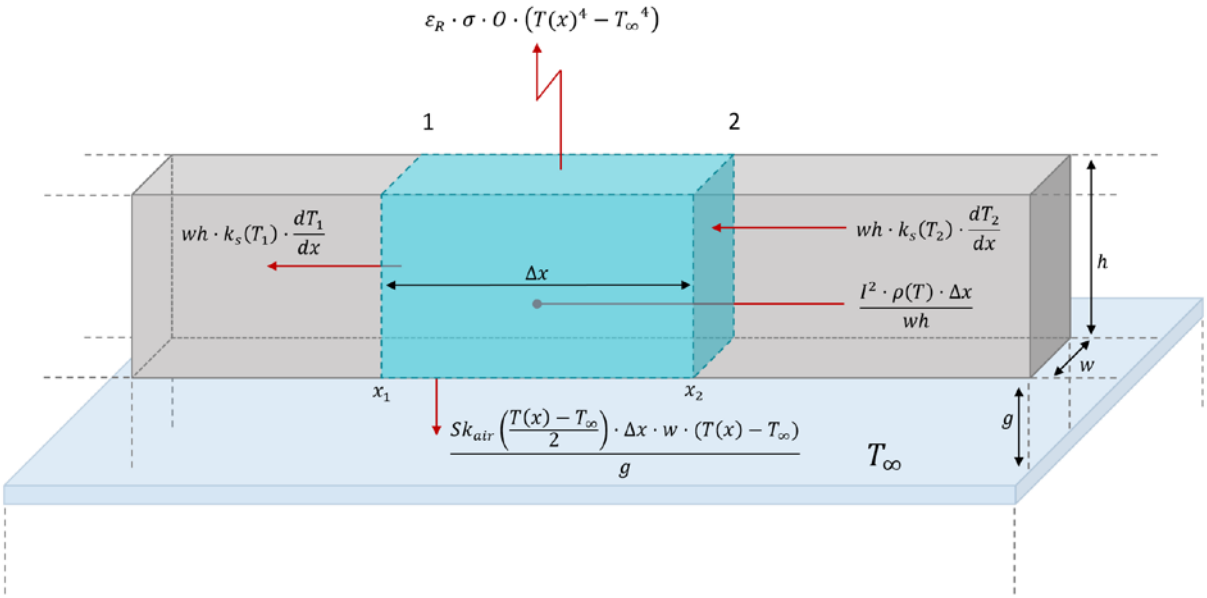

Figure 60. Heat transfer of a clamped-clamped beam.

The equation for the heat transfer situation in figure 60 is:

$$wh\left(k_s(T_2)\frac{dT_2}{dx} - k_s(T_1)\frac{dT_1}{dx}\right) + \Delta x\left[\frac{I^2\rho(T)}{wh} - wSk_{air}\left(\frac{T(x)+T_\infty}{2}\right)\frac{T(x)-T_\infty}{g} - \varepsilon_R\sigma O\left(T(x)^4 - T_\infty{}^4\right)\right] = 0 \tag{A.48}$$

Equation (A.48) must first be dived by Δx:

$$\frac{wh\left(k_s(T_2)\frac{dT_2}{dx} - k_s(T_1)\frac{dT_1}{dx}\right)}{\Delta x} + \frac{I^2\rho(T)}{wh} - wSk_{air}\left(\frac{T(x)+T_\infty}{2}\right)\frac{T(x)-T_\infty}{g} - \varepsilon_R\sigma O\left(T(x)^4 - T_\infty{}^4\right) = 0 \tag{A.49}$$

By taking the limit of Δx to 0 gives the derivative of $k_s(T) \cdot \frac{dT}{dx}$:

$$\frac{d}{dx}\left[k_s(T) \cdot \frac{dT(x)}{dx}\right] + J^2\rho(T) - Sk_{air}(T) \cdot \frac{T(x)-T_\infty}{gh} - \varepsilon_R\sigma O\left(T(x)^4 - T_\infty{}^4\right) = 0 \tag{A.50}$$

Differentiating equation (A.50) using the chain rule gives:

$$\frac{dT(x)}{dx} \cdot \frac{dk_s(T)}{dx} + k_s(T) \cdot \frac{d^2T(x)}{dx^2} + J^2\rho(T) - Sk_{air}(T) \cdot \frac{T(x)-T_\infty}{gh} - \varepsilon_R\sigma O\left(T(x)^4 - T_\infty{}^4\right) = 0 \tag{A.51}$$

As $k_s(T)$ is as function of temperature and not position, $k_s(T)$ should be differentiated to temperature:

$$\frac{dT(x)}{dx}\cdot\left(\frac{dk_s(T)}{dT}\cdot\frac{dT(x)}{dx}\right)+k_s(T)\cdot\frac{d^2T(x)}{dx^2}+J^2\rho(T)-Sk_{air}(T)\cdot\frac{T(x)-T_\infty}{gh}-\varepsilon_R\sigma O\left(T(x)^4-{T_\infty}^4\right)=0 \tag{A.52}$$

Rewriting equation (A.52) gives an expression for the second derivative of $T(x)$:

$$\frac{d^2T(x)}{dx^2}=\frac{1}{k_s(T)}\cdot\left(\frac{(T(x)-T_\infty)\cdot Sk_{air}(T)}{gh}-J^2\rho(T)-\left(\frac{dT(x)}{dx}\right)^2\cdot\frac{dk_s(T)}{dT}\right)-\varepsilon_R\sigma O\left(T(x)^4-{T_\infty}^4\right) \tag{A.53}$$

A.3.2 Analytical

By assuming k_s, k_{air} and ρ are constant, in absence of radiation ($\varepsilon_R=0$), equation (A.53) will give the equation set up by [11]:

$$\frac{d^2T(x)}{dx^2}k_s-\frac{(T(x)-T_\infty)\cdot Sk_{air}}{gh}+J^2\rho=0 \tag{A.54}$$

The solution to differential equation (A.54) is [11]:

$$T(x)=T_\infty+\frac{J^2\rho}{k_sb^2}+z_1e^{bx}+z_2e^{-bx} \tag{A.55}$$

In equation (A.55) the substitution $b^2=\frac{Sk_{air}}{k_sgh}$ is made. Using the boundary conditions $T(0)=T(2L)=T_\infty$, z_1, z_2 can be solved:

$$\begin{aligned}z_1&=\frac{J^2\rho}{k_sb^2}\cdot\frac{e^{-2bL}-1}{e^{2bL}-e^{-2bL}}\\ z_2&=-\frac{J^2\rho}{k_sb^2}\cdot\frac{e^{2bL}-1}{e^{2bL}-e^{-2bL}}\end{aligned} \tag{A.56}$$

Substituting equations (A.56) in equation (A.55) gives the analytic solution:

$$T(x)=T_\infty+\frac{J^2\rho}{k_s\,b^2}\cdot\left(1+\frac{e^{-2bL}-1}{e^{2bL}-e^{-2bL}}\cdot e^{bx}-\frac{e^{2bL}-1}{e^{2bL}-e^{-2bL}}\cdot e^{-bx}\right) \tag{A.57}$$

A.4 Thermo-mechanical model derivation

A.4.1 Strains

A.4.1.1 Bending strain

When a beam is exposed to a moment, M, on both sides, it will bend. While bending, the beam will get a circular arc shape, shown in figure 61.

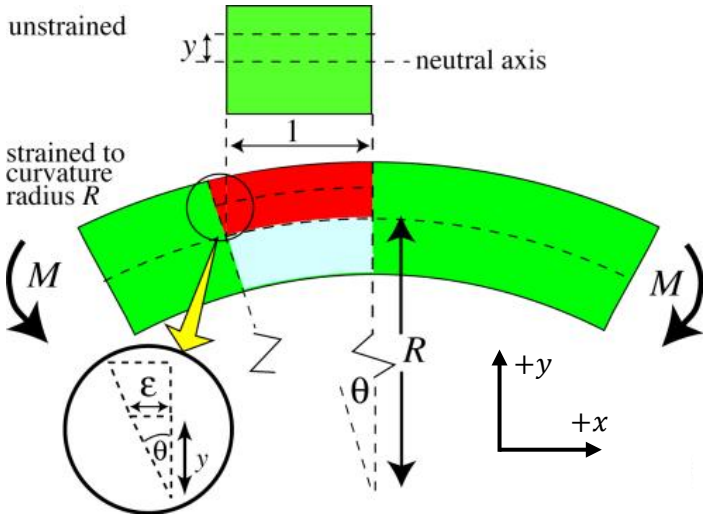

Figure 61. Schematic representation of a bending beam piece. [29]

The length at the neutral axis of the beam, L_R, stays the same length when the beam bends. The arc length of a circle is per definition:

$$L_R = R_R \cdot \theta_R \tag{A.17}$$

Using equation (A.17) gives an expression for the arc length of the red piece in figure 61:

$$L(y) = (R_R + y) \cdot \theta_R \tag{A.18}$$

Combining equation (A.17) and (A.18) gives:

$$L(y) = (R_R + y) \cdot \frac{L_R}{R_R} = L_R \cdot \left(1 + \frac{y}{R_R}\right) \tag{A.19}$$

The local strain is defined as the expansion or compression divided by the initial length:

$$\varepsilon = \frac{\Delta L_\varepsilon}{L_\varepsilon} \tag{A.20}$$

An expression for the bending strain can be set up by combining equation (A.19) and (A.20):

$$\varepsilon_b = \frac{\Delta L_\varepsilon}{L_\varepsilon} = \frac{L(y) - L_R}{L_R} = \frac{L_R + L_R \cdot \frac{y}{R_R} - L_R}{L_R} = \frac{y}{R_R} \tag{A.21}$$

A small bent beam piece, dL, can be described by equation (A.17) as:

$$dl = R_R \cdot d\theta_R \rightarrow \frac{1}{R_R} = \frac{d\theta_R}{dl} \tag{A.22}$$

For small values of dl can the estimation $dl \approx dx$ be made, giving:

$$\frac{1}{R_R} = \frac{d\theta_R}{dl} \approx \frac{d\theta_R}{dx} \tag{A.23}$$

A beam has a transversal displacement, w, when the beam bends. For a small piece of a beam dw can be described as:

$$dw = dx \cdot \tan(\theta_R) \tag{A.24}$$

At small values for θ_R the estimation $\tan(\theta_R) \approx \theta_R$ can be made, giving:

$$\frac{dw}{dx} = \tan(\theta_R) \approx \theta_R \tag{A.25}$$

Combining equation (A.22) and (A.25) gives the relation between R and w:

$$\frac{1}{R_R} = \frac{d\theta_R}{dx} = \frac{d^2w}{dx^2} \tag{A.26}$$

Substituting equation (A.26) in equation (A.21) gives:

$$\varepsilon_b = y \cdot \frac{d^2w}{dx^2} \tag{A.27}$$

A.4.1.2 Stretching strain

The stretching of a small piece, dx, of a beam clamped on both sides is shown in figure 2.

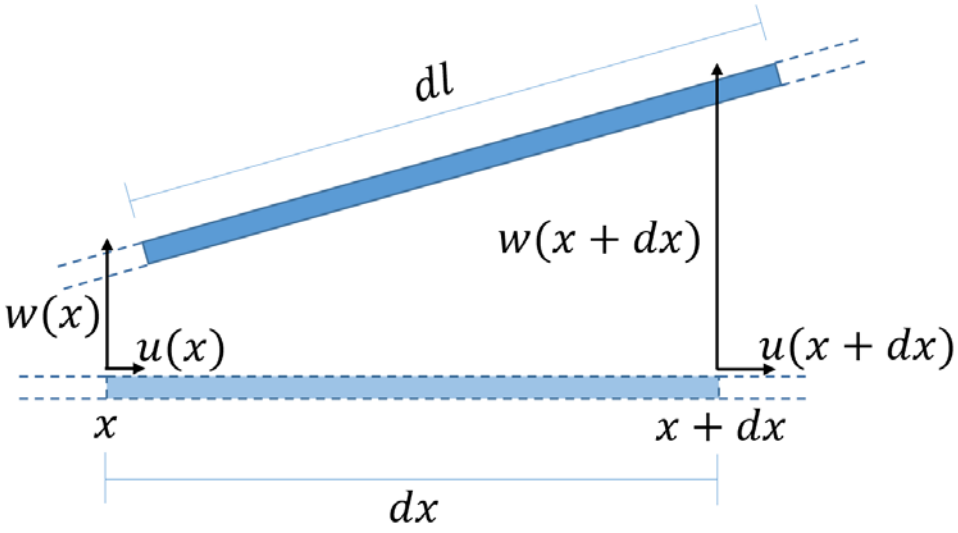

Figure 62. Schematic representation of the stretching of a small beam piece, dx, of a beam clamped on both sides.

The length of resulting beam piece, dl, can be described using Pythagoras theorem:

$$dl = \sqrt{\big(dx + u(x+dx) - u(x)\big)^2 + \big(w(x+dx) - w(x)\big)^2} \tag{A.28}$$

Combining equation (A.20) and (A.28) gives an expression for the stretching strain:

$$\varepsilon_s = \frac{\Delta L_\varepsilon}{L_\varepsilon} = \frac{dl - dx}{dx} = \frac{\sqrt{\big(dx + u(x+dx) - u(x)\big)^2 + \big(w(x+dx) - w(x)\big)^2}}{dx} - 1 \tag{A.29}$$

If the dx in equation (A.29) is brought within the square root, the derivate of $u(x)$ and $w(x)$ appear:

$$\varepsilon_s = \sqrt{\left(1 + \frac{u(x+dx) - u(x)}{dx}\right)^2 + \left(\frac{w(x+dx) - w(x)}{dx}\right)^2} - 1 \tag{A.30}$$

Rewriting equation (A.30) gives:

$$\varepsilon_s = \sqrt{\left(1 + \frac{du(x)}{dx}\right)^2 + \left(\frac{dw(x)}{dx}\right)^2} - 1 \tag{A.31}$$

Expanding equation (A.31) gives:

$$\varepsilon_s = \sqrt{1 + \left(\frac{du(x)}{dx}\right)^2 + 2\frac{du(x)}{dx} + \left(\frac{dw(x)}{dx}\right)^2} - 1 \tag{A.32}$$

As both $\frac{du(x)}{dx}$ and $\frac{dw(x)}{dx} \ll 1$, a first order Taylor series ($\sqrt{1+\gamma} \approx 1 + \frac{1}{2}\gamma$) of equation (A.32), gives:

$$\varepsilon_s = \frac{du(x)}{dx} + \frac{1}{2} \cdot \left(\left(\frac{du(x)}{dx}\right)^2 + \left(\frac{dw(x)}{dx}\right)^2\right) \tag{A.33}$$

The effect of stretching is much more significant for the transversal displacement as for the longitudinal displacement, thus $\frac{du(x)}{dx} \ll \frac{dw(x)}{dx}$, giving:

$$\varepsilon_s = \frac{du(x)}{dx} + \frac{1}{2} \cdot \left(\frac{dw(x)}{dx}\right)^2 \tag{A.34}$$

A.4.1.3 Thermal strain

The thermal strain in a beam is given by:

$$\varepsilon_T = \alpha \cdot \overline{\Delta T} \tag{A.35}$$

A.4.1.4 Total strain

The stretching strain (or total strain) of the beam can be described by combining all the strains acting on the beam and accounting for the reaction for P_0 that compensated the expansion of the beam:

$$\varepsilon_s = \alpha \cdot \overline{\Delta T} - y \cdot \frac{d^2w}{dx^2} - \frac{P_0}{EA} \tag{A.36}$$

A.4.2 Transversal displacement

The beam model used by [12] to describe the Thermo-Mechanical behavior of the V-shaped ETA is shown in figure 63. Because of the geometric symmetry, only half the beam is modeled.

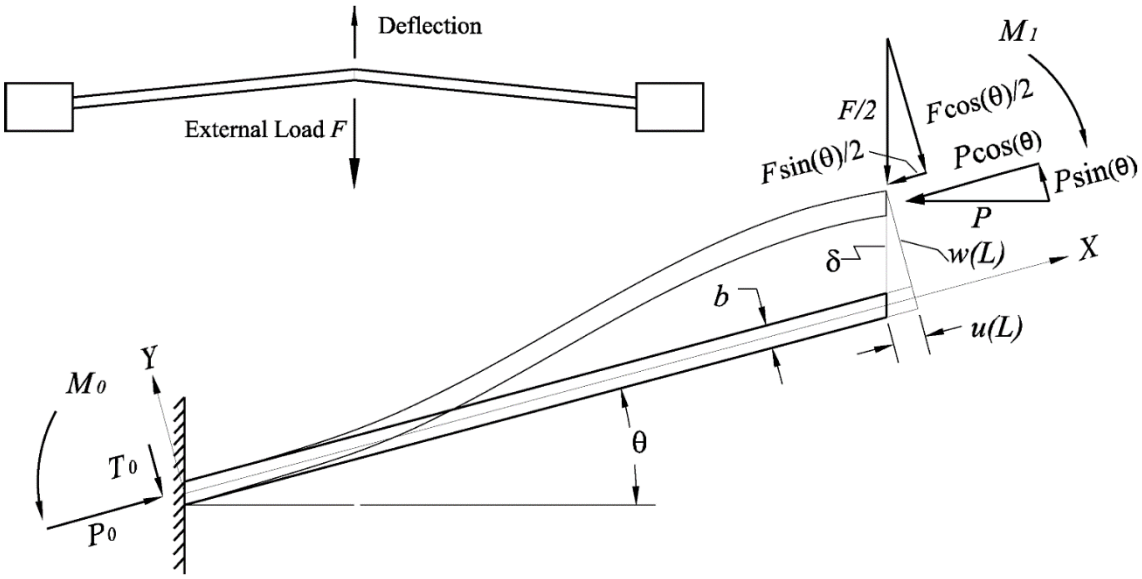

Figure 63. The geometry and loads of a V-shaped beam actuator. [12]

The use of the Euler beam theory results in an equation for all the moments acting on the beam:

$$-EI \cdot \frac{d^2w(x)}{dx^2} = P_0 \cdot w(x) + T_0 \cdot x + M_0 \tag{A.37}$$

The solution to equation (A.37) is:

$$w(x) = C_1 \cdot (\cos(kx) + i \cdot \sin(kx)) + C_2 \cdot (\cos(kx) + i \cdot \sin(kx)) - \frac{T_0}{P_0} \cdot x - \frac{M_0}{P_0} \tag{A.38}$$

Five boundary conditions are needed to solve the complete Thermo-mechanical model [12]:

$$\begin{gathered} w(0) = 0 \\ \frac{dw(0)}{dx} = 0 \\ \frac{dw(L)}{dx} = 0 \\ u(0) = 0 \\ u(L) = w(L) \cdot \tan(\theta) \end{gathered} \tag{A.39}$$

Combining equation (A.38) with the first three boundary conditions from equation (A.39) gives:

$$C_1 = \frac{1}{2} \cdot \frac{T_0 \cdot (\cos(kL)\, i + \sin(kL) - i)}{\sin(kL) \cdot kP_0 i}$$
$$C_2 = -\frac{1}{2} \cdot \frac{T_0 \cdot (-\cos(kL)\, i + \sin(kL) + i)}{\sin(kL) \cdot kP_0 i} \tag{A.40}$$
$$M_0 = \frac{T_0 \cdot (\cos(kL) - 1)}{\sin(kL) \cdot k}$$

The reaction forces acting at the fixed beam end can be expressed as [12]:

$$P_0 = P \cdot \cos(\theta) + \frac{F_v}{2} \cdot \sin(\theta)$$
$$T_0 = P \cdot \sin(\theta) - \frac{F_v}{2} \cdot \cos(\theta) \tag{A.41}$$

Substituting equation (A.41) and (A.40) in equation (A.38) gives the expression for the transversal displacement of the beam:

$$w(x) = \left(\tan\theta - \frac{F_v}{2k^2 EI \cos\theta}\right) \cdot \left(\frac{\sin kx}{k} + \frac{(\cos kL - 1) \cdot (\cos kx - 1)}{k \sin kL} - x\right) \tag{A.42}$$

A.4.3 Transcendental equation

The first order differential equation which results in the transcendental equation, $c(k, F_v, \overline{\Delta T})$, can be set up from equation (A.34) and (A.36) for $y = 0$:

$$\frac{du(x)}{dx} + \frac{1}{2} \cdot \left(\frac{dw(x)}{dx}\right)^2 - \alpha \cdot \overline{\Delta T} + \frac{P_0}{EA} = 0 \tag{A.43}$$

Integrating along the half-span, L, of the beam gives:

$$\big(u(L) - u(0)\big) + \int_0^L \frac{1}{2} \cdot \left(\frac{dw(x)}{dx}\right)^2 - \alpha \cdot \overline{\Delta T} \cdot L + \frac{P_0}{EA} \cdot L = 0 \tag{A.44}$$

Applying the last two boundary conditions of equation (A.39) gives:

$$w(L) \cdot \tan(\theta) + \int_0^L \frac{1}{2} \cdot \left(\frac{dw(x)}{dx}\right)^2 - \alpha \cdot \overline{\Delta T} \cdot L + \frac{P_0}{EA} \cdot L = 0 \tag{A.45}$$

Solving the integral in equation (A.45) after substituting equation (A.42) gives the transcendental equation:

$$\begin{aligned} c(k, F_v, \overline{\Delta T}) = {} & \frac{k^2 I_x L}{A} + \alpha \overline{\Delta T} L + \frac{1}{2}\left(\tan\theta - \frac{F_v}{2k^2 EI_x \cos\theta}\right)^2 \\ & \cdot \left\{ L\left(1 + \frac{1}{\cos(kL) + 1}\right) - \frac{3\tan\left(\frac{1}{2}kL\right)}{k} \right\} + \tan\theta \cdot \left(\frac{2}{k}\tan\left(\frac{kL}{2}\right) - L\right) \\ & \cdot \left(\tan\theta - \frac{F_v}{2k^2 EI_x \cos\theta}\right) \end{aligned} \tag{A.46}$$

or,

$$c(k, F_v, \overline{\Delta T}) = \frac{k^2 I_x L}{A} + \alpha \overline{\Delta T} L + \frac{1}{2}\left(\tan\theta - \frac{F_v}{2k^2 E I_x \cos\theta}\right)^2 \cdot \left\{L + \frac{kL - 2\sin kL}{k \cdot (\cos kL + 1)}\right\} + \tan\theta \cdot \left(\frac{2}{k}\tan\left(\frac{kL}{2}\right) - L\right) \cdot \left(\tan\theta - \frac{F_v}{2k^2 E I_x \cos\theta}\right) \quad \text{(A.47)}$$

Equation (A.46) and equation (A.47) are equal to the transcendental equation given by [12].

B Appendix: Material properties

This appendix will show the required material properties of silicon and air.

B.1 Silicon properties

B.1.1 Thermal conductivity

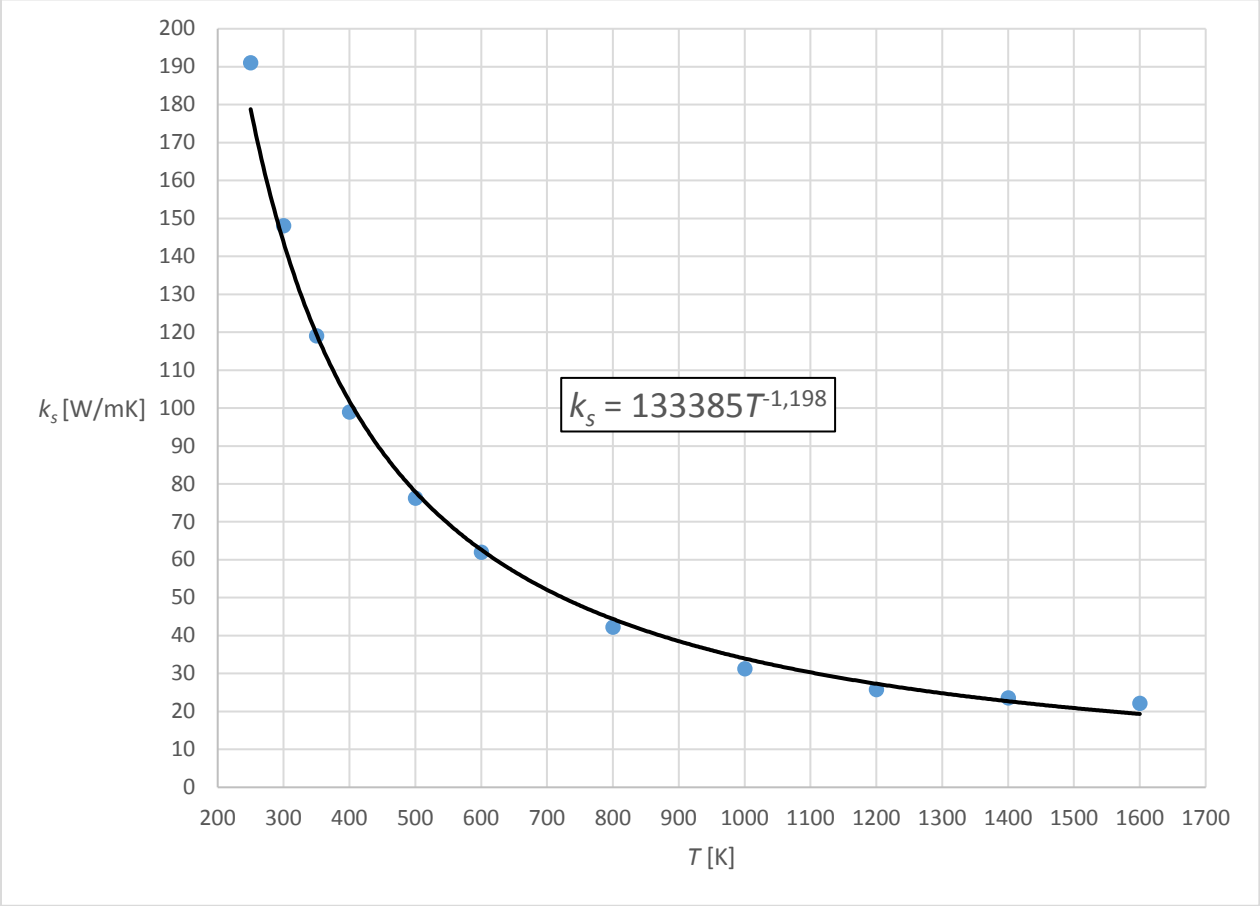

Figure 64. Thermal conductivity of silicon versus temperature at 101325 Pa.

Thermal conductivity data obtained from: [30]

Table 4. Thermal conductivity of silicon data at 101325 Pa.

T [K]	k_s [W/mk]
250	191
300	148
350	119
400	98,9
500	76,2
600	61,9
800	42,2
1000	31,2
1200	25,7
1400	23,5
1600	22,1

B.1.2 Young's modulus

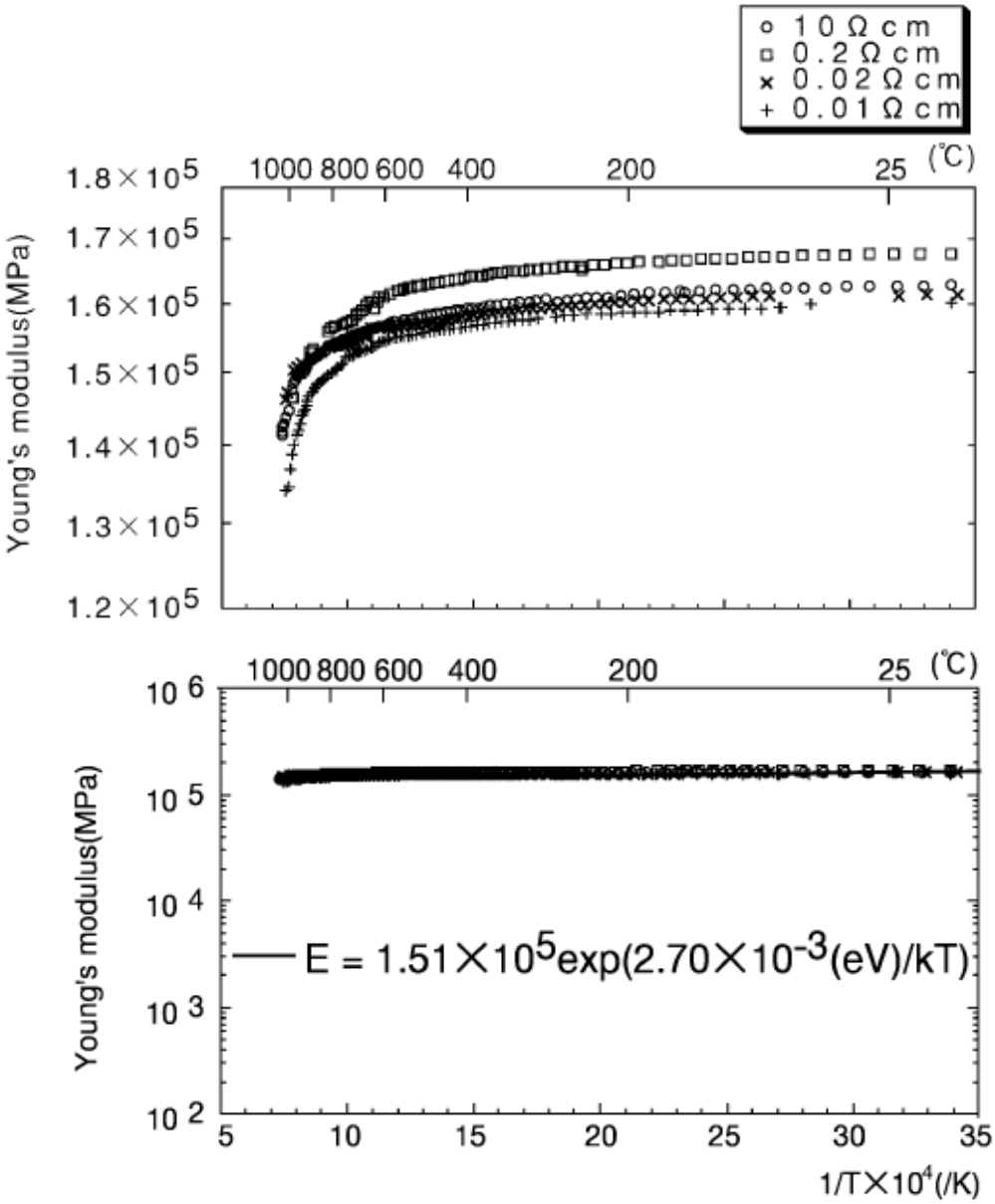

Figure 65. Young's moduli of silicon at different resistivity. [31]

Young's moduli Data obtained from: [31]

B.1.3 Thermal expansion coefficient

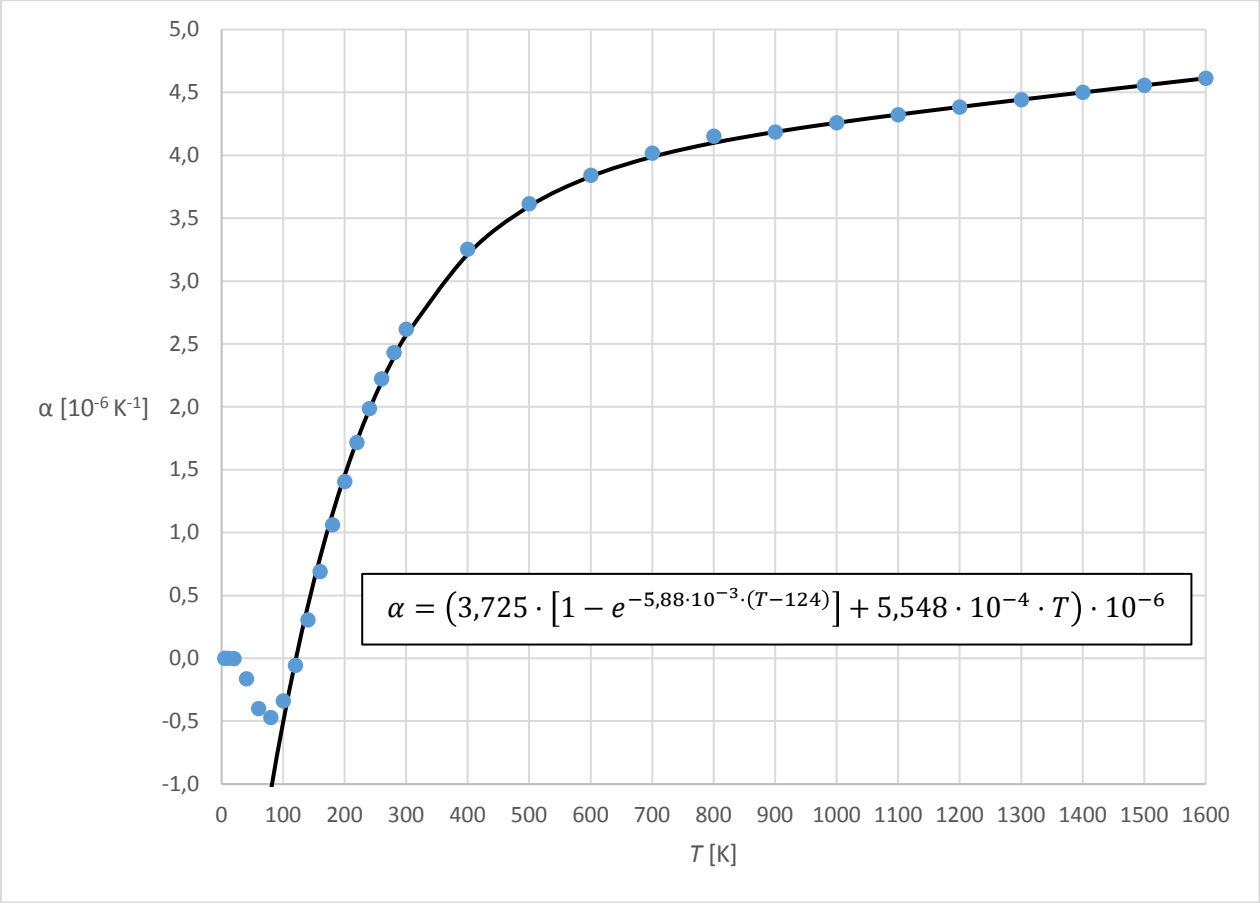

Figure 66. Thermal expansion coefficient of silicon versus temperature.

The equation presented in figure 66 (black line) holds between 120 K and 1500 K.

Thermal expansion data obtained from: [32]

Table 5. Thermal expansion coefficient of silicon. [32]

T [K]	α [$\cdot 10^{-6}$ K^{-1}]	T [K]	α [$\cdot 10^{-6}$ K^{-1}]
5	$0{,}6 \cdot 10^{-4}$	280	2,432
10	$0{,}48 \cdot 10^{-3}$	300	2,616
20	$-0{,}29 \cdot 10^{-2}$	400	3,253
40	$-0{,}164$	500	3,614
60	$-0{,}400$	600	3,842
80	$-0{,}472$	700	4,016
100	$-0{,}399$	800	4,151
120	$-0{,}057$	900	4,185
140	0,306	1000	4,258
160	0,689	1100	4,323
180	1,061	1200	4,384
200	1,406	1300	4,442
220	1,715	1400	4,500
240	1,986	1500	4,556
260	2,223	1600	4,612

B.1.4 Resistivity

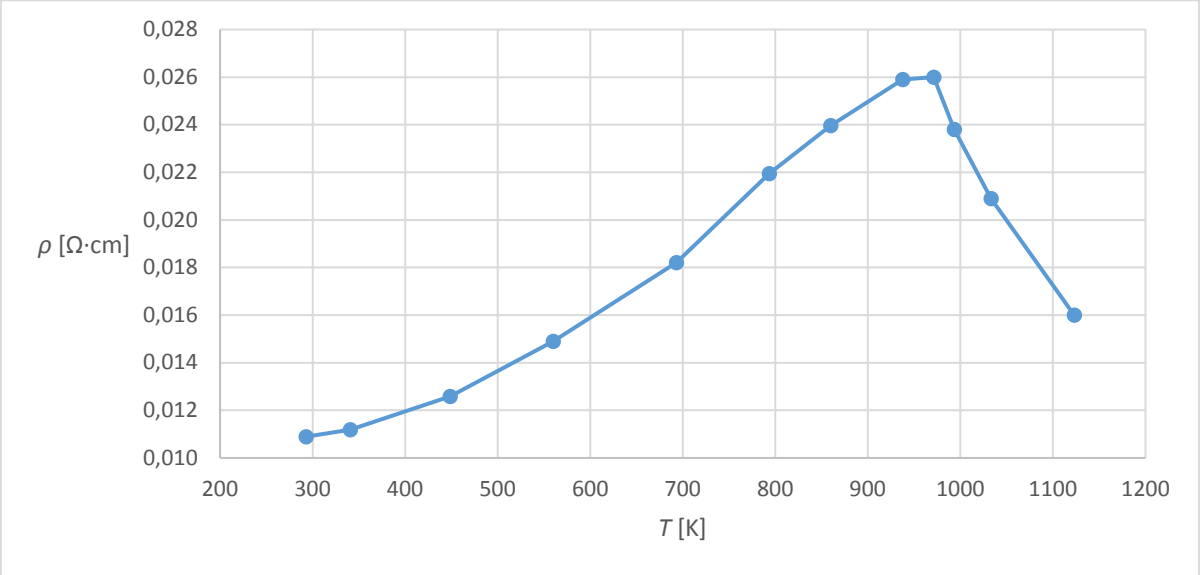

Figure 67. Estimated silicon resistivity versus temperature.

The estimation of the resistivity is done by iteratively changing the resistivity at a certain temperature till the resistance obtained from the Electro-thermal model matched the measured resistance of the G1.4 Back ETA in air and in vacuum. Before the resistance is matched R_p and $2 \cdot R_c$ are subtracted from the Back ETA resistance, because it is assumed that these do not depend on temperature and will negatively influence the resistivity estimation.

Table 6. Estimated silicon resistivity data.

T [K]	ρ [$\cdot 10^{-2}$ Ωcm]
293,00	1,09
340,77	1,12
448,64	1,26
559,81	1,49
693,22	1,82
793,27	2,12
859,97	2,40
937,79	2,59
971,14	2,60
993,38	2,38
1033,00	2,09
1123,00	1,60

B.1.5 Specific heat

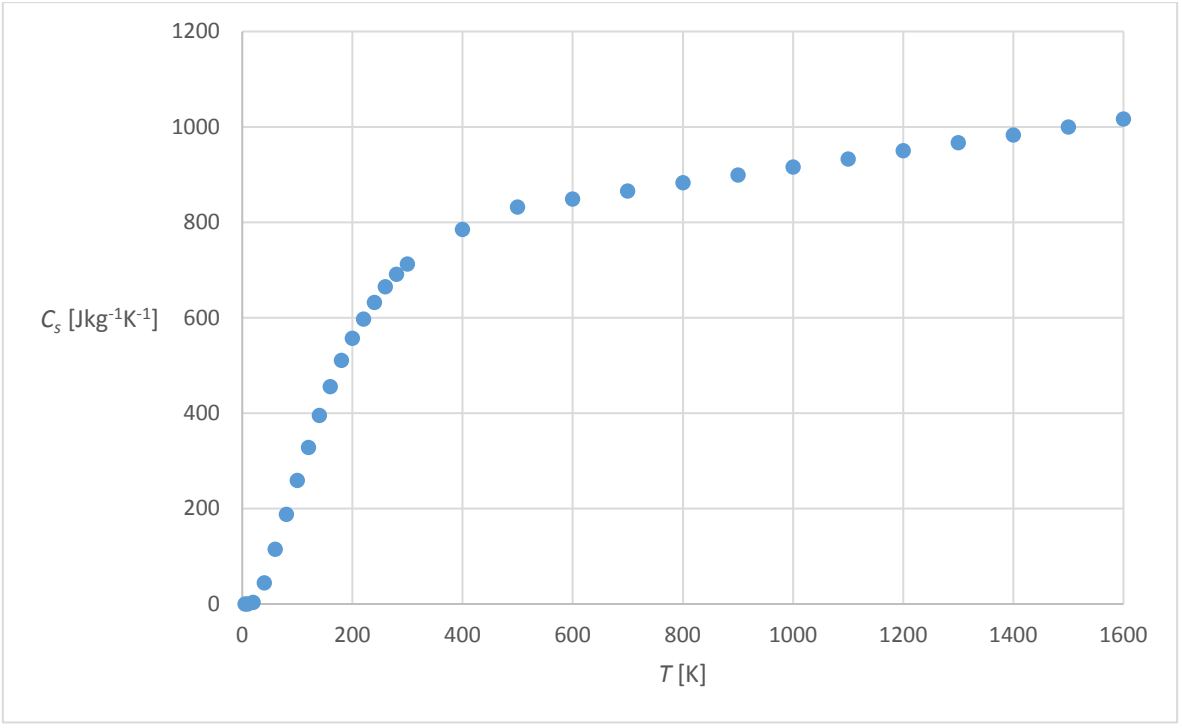

Figure 68. Specific heat of silicon as function of temperature.

Specific heat data obtained from: [32]

B.2 Thermal conductivity air

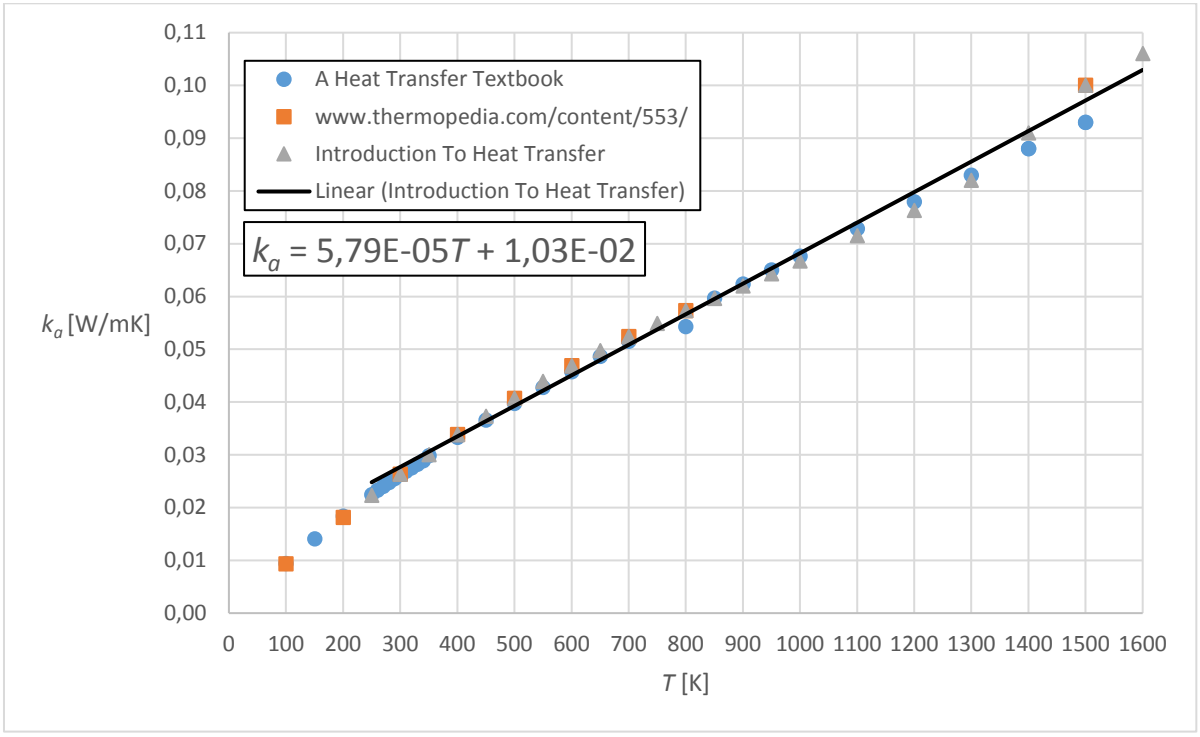

Figure 69. Thermal conductivity of air versus temperature.

Data obtained from: [33], [34], [35]

C Appendix: Thermal time constant estimation

This appendix will explain how the thermal time constant of the beam is estimated using a simple model, both in air and in vacuum.

C.1 Air

The time constant in air of a beam can be estimated using the beam schematic presented in figure 70.

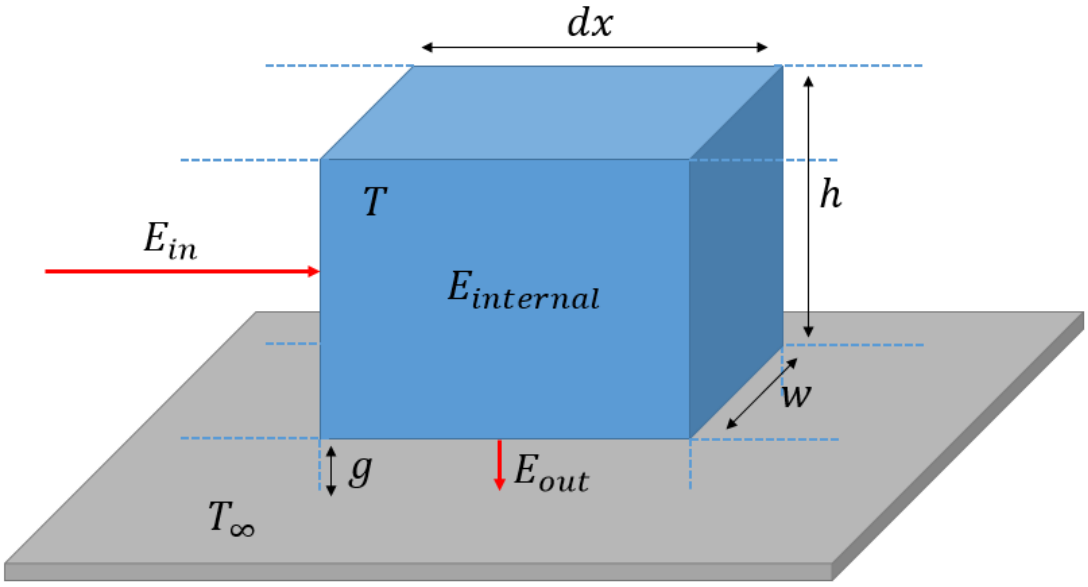

Figure 70. Schematic of the energy flow in a beam part of length dx in air.

Formula wise the energy flow can be described as:

$$E_{in} - E_{out} = E_{internal} \tag{C.1}$$

The beam is heated by an electric current and assuming all the heat is transferred to the substrate through air, gives an expression for the heat transfer at time interval dt:

$$\frac{I^2\rho \cdot dx}{wh} \cdot dt - \frac{Sk_{air}w \cdot dx \cdot \Delta T}{g} \cdot dt = C_s\rho_d wh \cdot dx \cdot \Delta T \tag{C.2}$$

Where C_s is the specific heat of silicon and ρ_d is the density of silicon. Equation (C.2) can be divided by $dx \cdot dt$ giving:

$$\frac{I^2\rho}{wh} - \frac{Sk_{air}w \cdot \Delta T}{g} = C_s\rho_d wh \cdot \frac{dT}{dt} \tag{C.3}$$

Assuming $T_\infty \ll T$, ΔT can be written as T, giving:

$$\frac{I^2\rho}{wh} - \frac{Sk_{air}w \cdot T}{g} = C_s\rho_d wh \cdot \frac{dT}{dt} \tag{C.4}$$

A first order differential equation appears. Rewriting equation (C.4) gives:

$$c_c \cdot \frac{dT}{dt} + b_c \cdot T - a_c = 0 \tag{C.5}$$

with

$$a_c = \frac{I^2\rho}{wh}$$
$$b_c = \frac{Sk_{air}w}{g} \tag{C.6}$$
$$c_c = C_s\rho_d wh$$

The solution to equation (C.5) is:

$$T(t) = \frac{a_c}{b_c} + z_c \cdot e^{-\frac{b_c}{c_c}t} \tag{C.7}$$

Equation (C.7) has the standard form of exponential function $e^{-\frac{t}{\tau}}$, thus giving:

$$\tau = \frac{c_c}{b_c} = \frac{C_s\rho_d hg}{Sk_{air}} \tag{C.8}$$

τ is estimated for room temperature till $T = 1400$ K (ρ_d obtained from [36]). This is shown in figure 41.

C.2 Vacuum

The time constant in vacuum of a beam can be estimated by describing half the beam where a quarter of the beam contains temperature T and the other quarter temperature T_∞, see figure 71.

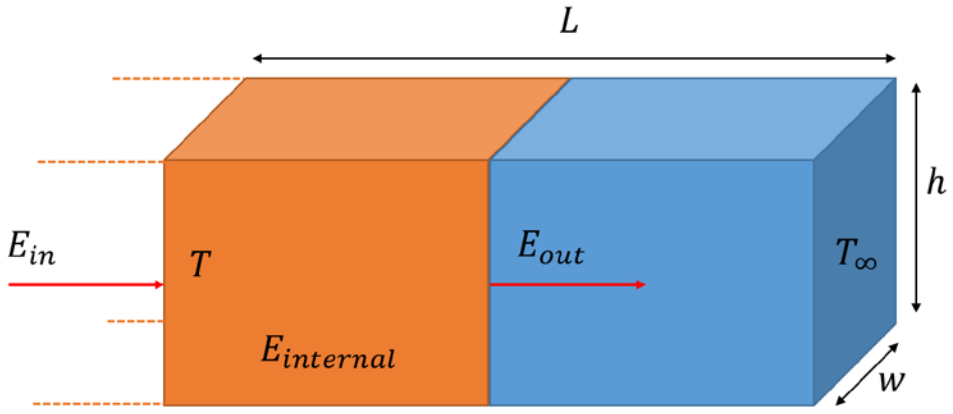

Figure 71. Schematic of the energy flow in a beam with length L in vacuum, dived in two halves.

Using Formula (C.1) a description for the heat transfer in figure 71 can be made:

$$\frac{I^2\rho \cdot \frac{1}{2}L}{wh} \cdot dt - \frac{k_s w \cdot h \cdot \Delta T}{\frac{1}{2}L} \cdot dt = C_s\rho_d wh \cdot \frac{1}{2}L \cdot \Delta T \tag{C.9}$$

Dividing by dt and assuming $T_\infty \ll T$, equation (C.9) can be written as:

$$\frac{I^2\rho \cdot \frac{1}{2}L}{wh} - \frac{k_s w \cdot h \cdot T}{\frac{1}{2}L} = C_s\rho_d wh \cdot \frac{1}{2}L \cdot \frac{dT}{dt} \tag{C.10}$$

A first order differential equation appears. Rewriting equation (C.10) gives:

$$f_c \cdot \frac{dT}{dt} + e_c \cdot T - d_c = 0 \tag{C.11}$$

with

$$\begin{aligned} d_c &= \frac{I^2 \rho}{wh} \cdot \frac{1}{2} L \\ e_c &= \frac{k_s w \cdot h}{\frac{1}{2} L} \\ f_c &= C_s \rho_d wh \cdot \frac{1}{2} L \end{aligned} \tag{C.12}$$

The solution to equation (C.11) is:

$$T(t) = \frac{d_c}{e_c} + z_c \cdot e^{-\frac{e_c}{f_c} \cdot t} \tag{C.13}$$

Equation (C.13) has the standard form of exponential function $e^{-\frac{t}{\tau}}$, thus giving:

$$\tau = \frac{f_c}{e_c} = \frac{C_s \rho_d}{k_s} \cdot \frac{1}{4} L^2 \tag{C.14}$$

τ is estimated for room temperature till $T = 1400$ K. This is shown in figure 41.

Table 7. Modeling parameters.

Object	Description	Symbol	Value/expression	Unit
General	Distance between beam and substrate	g	4	µm
	Device layer height	h	50	µm
	Substrate temperature	T_∞	293	K
Silicon	Thermal conductivity	$k_s(T)$	$133385 \cdot T^{-1,198}$	$\mathrm{Wm^{-1}K^{-1}}$
	Young's modulus	$E(T)$	$1{,}51 \cdot 10^5 \cdot e^{\frac{4{,}33 \cdot 10^{-22}}{1{,}38 \cdot 10^{-23} \cdot T}}$	MPa
	Thermal expansion coefficient	$\alpha(T)$	$\left(3{,}725 \cdot \left[1 - e^{-5{,}88 \cdot 10^{-3} \cdot (T-124)}\right] + 5{,}548 \cdot 10^{-4} \cdot T\right) \cdot 10^{-6}$	$\mathrm{K^{-1}}$
	Specific heat	$C_s(T)$	See figure 67, appendix B.1.5	$\mathrm{Jkg^{-1}K^{-1}}$
	Resistivity	$\rho(T)$	See table 6, appendix B.1.4	Ωm
Air	Thermal conductivity	$k_{air}(T)$	$5{,}79 \cdot 10^{-5} \cdot T + 1{,}03 \cdot 10^{-2}$	$\mathrm{Wm^{-1}K^{-1}}$
ETA	Half-span length	L	1450	µm
	Effective width	w_e	24,1	µm
	Effective second moment of area	I_{eff}	$1{,}89 \cdot 10^{-19}$	$\mathrm{m^4}$
	Shape factor	S	2,33	–
Curved cantilever spring	Length	L_R	1762,53	µm
	Width	w_s	8,66	µm
	Radius of curvature	R_R	1762,53	µm
	Initial starting angle	α_0	0,5	–

E Appendix: Vacuum setup pictures

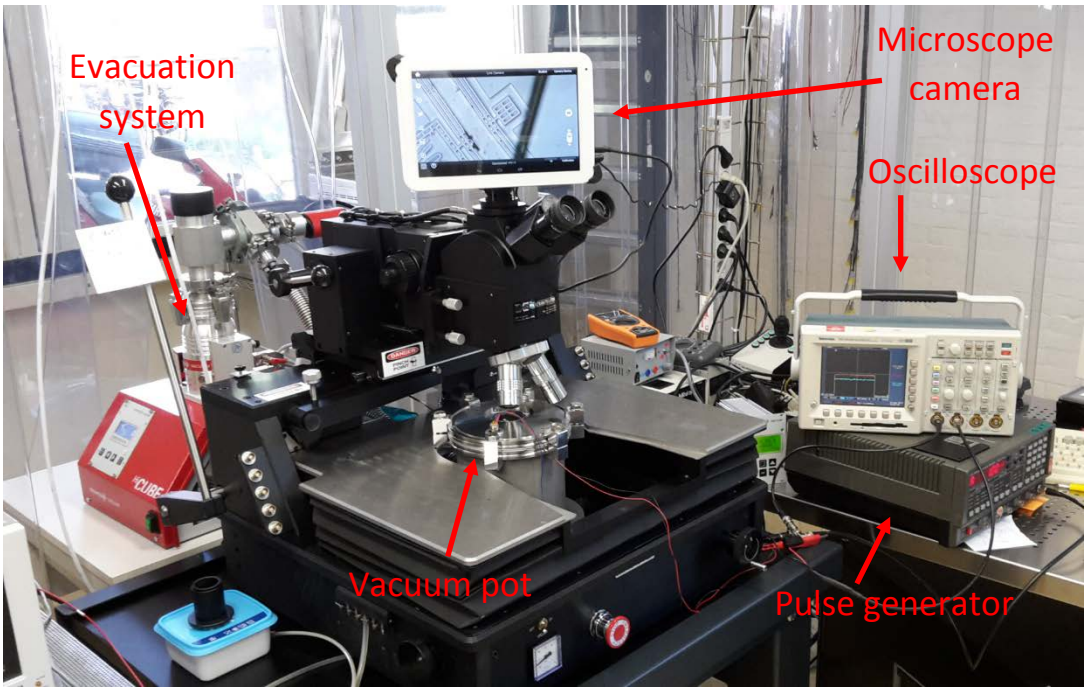

Figure 72. Picture of the vacuum measurement setup.

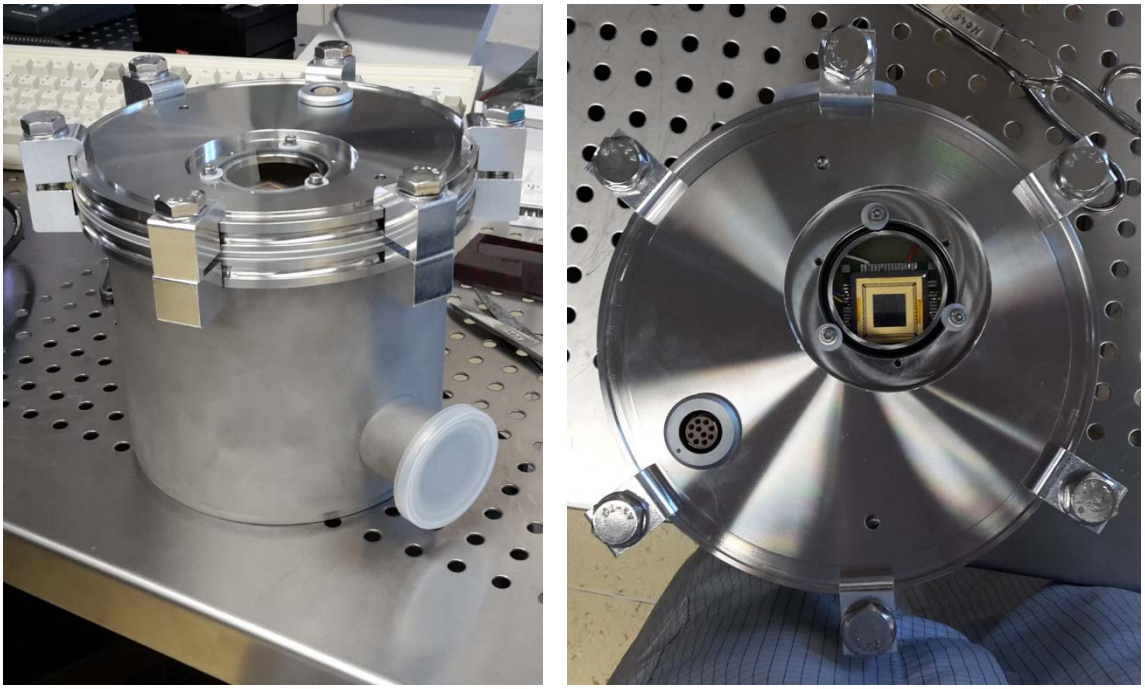

Figure 73. Picture of the vacuum pot. Left: side view. Right: top view. The MEMS inside the carrier can be seen through the window.

F Appendix: Shuttle locking pictures

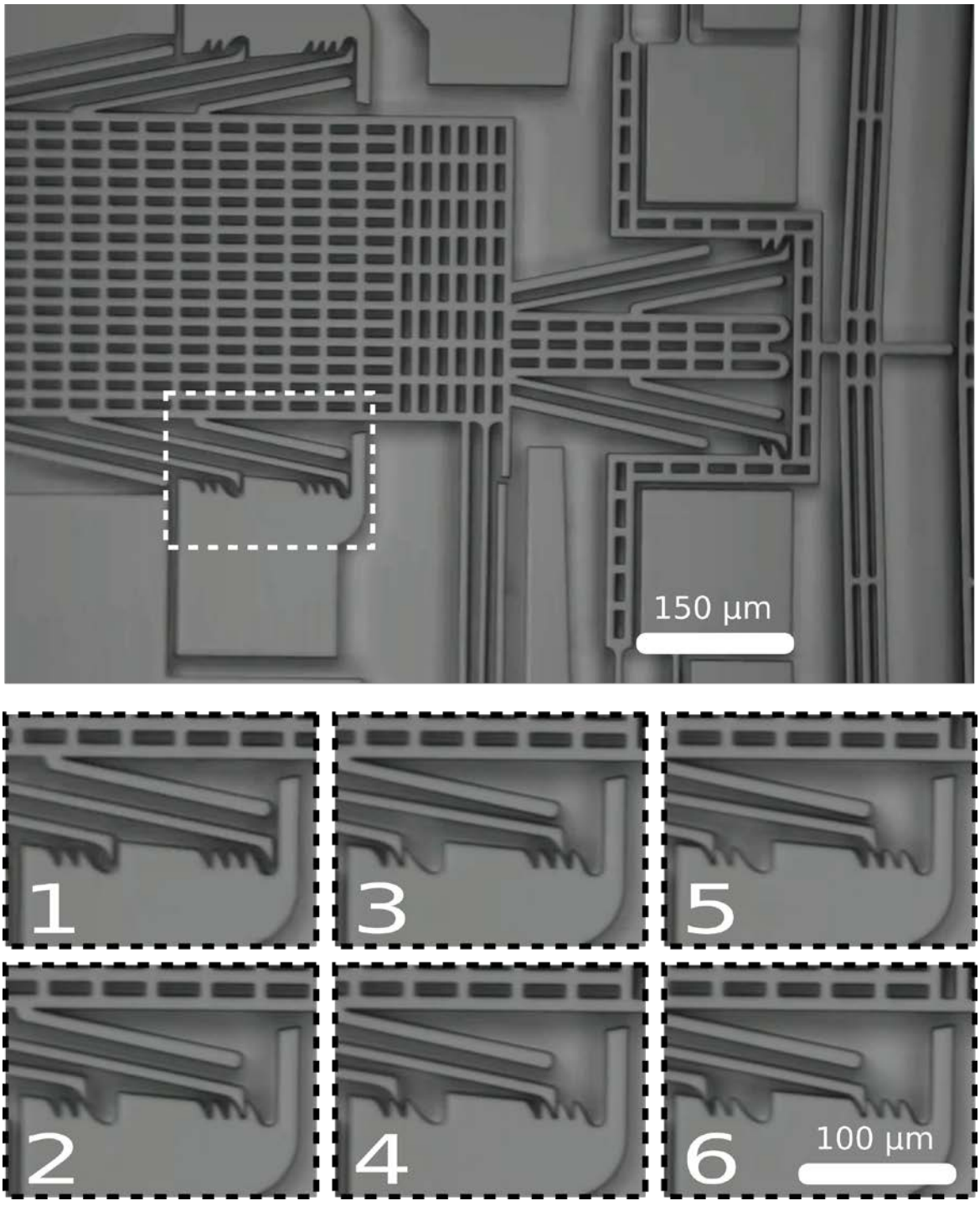

Figure 74. Microscope picture of the five shuttle locks.

1 Shows the Shuttle hooks and teeth without any lock;
2 Shows the first Shuttle lock;
3 Shows the second Shuttle lock;
4 Shows the third Shuttle lock;
5 Shows the fourth Shuttle lock;
6 Shows the fifth Shuttle lock.

G Appendix: Model operation

In this appendix is explained how the models operate in Excel and what formulas and codes are used for the three models used in this report. For every model the same cell colors are used to point out if a value in a cell can be changed or if it needs to be untouched, indicated by orange and yellow respectively.

G.1 Spring profile model

The force on the spring tip in x- and y-direction can be calculated for certain x- and y-displacements of the spring tip using equation (2.12). This equation can only be solved numerically. The numerical solution can be described formula wise as:

$$\theta_i = \theta_{i-1} + \theta'_{i-1} \cdot dl \qquad \theta'_i = \theta'_{i-1} + \theta''_{i-1} \cdot dl \tag{F.1}$$

With $i = 2,3,\dots,n$. This is illustrated in figure 75.

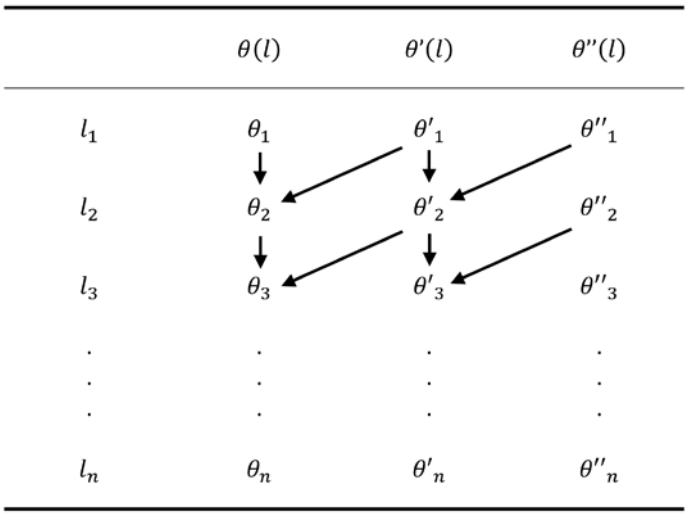

Figure 75. Illustration of the working principle of the numerical spring profile model.

The initial conditions θ_1, θ'_1 and θ''_1 are required to use equation (F.1). θ_1 can be chosen in this model and θ''_1 is acquired from equation (2.12) at l_1. θ'_1 must be calculated using the solver capabilities of Excel, for the boundary conditions $\theta_1 = -\theta_n = \alpha_0$. The following Macro is used to determine θ'_1:

```
Sub Calc_sp_pf()
    SolverReset
    SolverOk SetCell:="$B$29", MaxMinVal:=3, ValueOf:=0, ByChange:= _
    "$F$4,$B$34,$B$35", Engine:=1, EngineDesc:="GRG Nonlinear"
    SolverAdd CellRef:="$B$30", Relation:=2, FormulaText:="0"
    SolverAdd CellRef:="$B$31", Relation:=2, FormulaText:="0"
    SolverOptions AssumeNonNeg:=False
    SolverSolve Userfinish:=True
End Sub
```

The cells B29, B30 and B31 are the error of the input and the data from the model for θ_n, x_n and y_n respectively. F4 is θ'_1 and B34 and B35 are F_x and F_y respectively. The solver in Excel tries to get the error values as closely to zero as possible, by trying different values for F_x, F_y and θ'_1. If the error values are almost zero, Excel places the values for F_x, F_y and θ'_1 in their respective cells and numerically calculates the spring profile.

The variable input cells are presented in figure 76. θ_1 can be changed by altering the number behind α_0. Dimensions and other properties of the spring can be set by altering the numbers in the orange cells. In the "Input" table in figure 76 can θ_n, x_n and y_n be set, which are used in the calculation of the spring profile. The "Data" table show the current θ_n, x_n and y_n of the spring. The "Error" table subtracts the "Data" from the "Input". If all the orange cells are set, the "Calculate spring profile" button can be pushed. If this button is pushed, Excel calculates the spring profile. The "Output" table shows F_x, F_y, k_x and k_y. The spring profile of the spring can be determined from the angles along the axis by using formula (A.15). In figure 77 are the results presented for a compression the x-direction of 10 µm.

	A	B
2	Amount of spring beam pieces	
3	N [-] (max:3000)	3000
4	dl [µm^{-1}]	0,59
6	Dimensions	
7	L [µm]	1762,53
8	h [µm]	50
9	b [µm]	8,66
10	α_0 [rad]	0,5
11	I [µm^4]	2,71E+03
12	$x_j(L)$ [µm]	1690,00
14	Properties	
15	E [MPa]	1,68E+05
16	m [mg]	30
18	Input	
19	$\theta(L)$ [rad]	-0,50
20	$x(L)$ [µm]	0,00
21	$y(L)$ [µm]	0,40

	A	B
23	Data	
24	$\theta(L)$ [rad]	-0,50
25	$x(L)$ [µm]	0,00
26	$y(L)$ [µm]	0,40
28	Error	
29	$\theta(L)$ [rad]	1,52E-08
30	$x(L)$ [µm]	-3,77E-07
31	$y(L)$ [µm]	-3,47E-06
33	Output	
34	F_x [µN]	4,54E-03
35	F_y [µN]	4,19E-01
36	k_x [Nm^{-1}]	12030,293
37	k_y [Nm^{-1}]	1,048
38	$f_{x,0}$ [s^{-1}]	6374,228061
39	$f_{y,0}$ [s^{-1}]	118,9721172
43	Calculate spring profile	

Figure 76. Input and output cells of the spring profile model, in Excel.

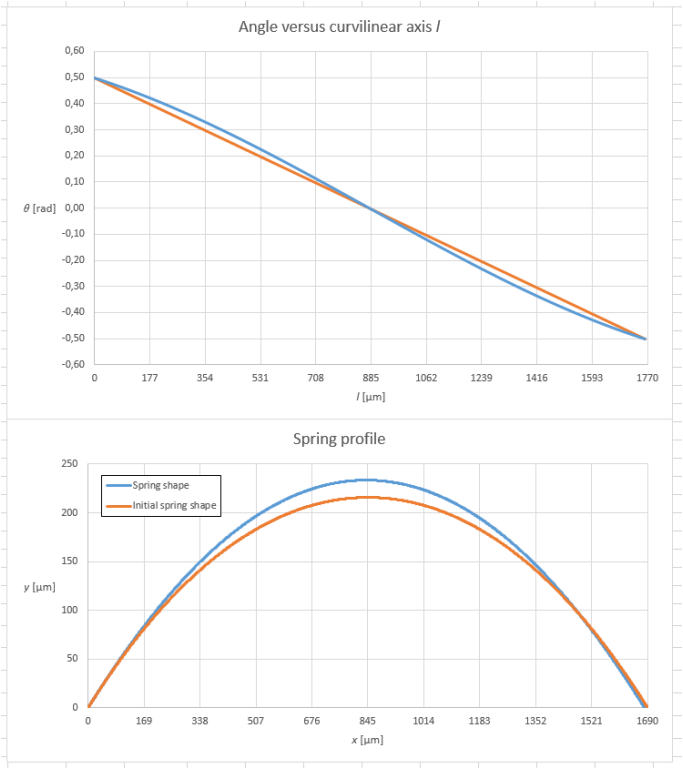

Figure 77. Spring profile model results for a compression in the x-direction of 10 µm.

The spring profile can be calculated for several compressions an different angles. If the spring constant in the y-direction is extracted from the model at certain displacements, it will show the decrease of the spring constant at larger displacements.

G.2 Electro-thermal model

The temperature profile of a beam, $T(x)$, can be determined for certain currents using equation (2.15). This equation can only be solved numerically. The working principle of this numerical model is the same as described for the Spring profile model (see figure 75), but now the required initial conditions are T_1, T'_1 and T''_1. T_1 is the substrate temperature and T''_1 is acquired from equation (2.15). Using the solver for boundary conditions $T_1 = T_\infty, T''_n = 0$, T'_1 can be calculated. The variable input cells of the model are presented in figure 78.

	A	B
2	Amount of beam pieces	
3	N [-] (max: 3000)	3000
4	dx [m]	4,83333E-07
6	Dimensions	
7	L [m]	1,45E-03
8	h [m]	5,00E-05
9	w [m]	2,41E-05
10	g [m]	4,00E-06
11	A [m^2]	1,2050E-09
13	Properties	
14	T_∞ [K]	293
15	S [-]	2,33
16	ε [-]	0
18	Input	
19	I [mA]	17,05
20	J [Am^{-2}]	14149377,59

	A	B
18	Input	
19	I [mA]	17,05
20	J [Am^{-2}]	14149377,59
22	Target	
23	T'(L) [K]	-1,99325E-07
25	Output	
26	R [Ω]	267,95
27	U [V]	4,57
28	P [mW]	77,89
29	T_{avg} [K]	331,06
30	$(\alpha \cdot \Delta T)_{avg}$ [-]	1,08E-04
31	T_{max} [K]	347,02
33	Iterations	5
34	Status	Solving done.
37	Calculate beam temperature profile	

Figure 78. Input and output cells of the Electro-thermal model, in Excel.

The dimensions and properties of the beam can be changed in the first three tables. The heat transfer due to radiation is optional in this model, but has not been used for the models in this report. The only input of this model is the current flowing through the beam and the resistivity of the used material. The resistivity can be altered in the table hidden under the temperature profile graph, see figure 79. If the "Calculate beam temperature profile" button is pushed, Excel calculates T'_1 for $T''_n = 0$. The following Macro is used for the calculation:

Resistivity		
T [K]	ρ [Ωm]	ρ' [ΩmK^{-1}]
293	1,09E-04	5,98E-08
340,77	1,12E-04	1,30E-07
448,639	1,26E-04	2,09E-07
559,81	1,49E-04	2,47E-07
693,216	1,82E-04	3,75E-07
793,27	2,20E-04	3,01E-07
859,972	2,40E-04	2,49E-07
937,792	2,59E-04	3,00E-08
971,143	2,60E-04	-9,89E-07
993,377	2,38E-04	-7,32E-07
1033	2,09E-04	-5,44E-07
1123	1,60E-04	-6,55E-07
1227,878	9,13E-05	-4,94E-07
1316,29	4,76E-05	-3,74E-07
1404,71	1,46E-05	

Test		Formula
T [K]	ρ' [ΩmK^{-1}]	0,00010895
340	5,976E-08	

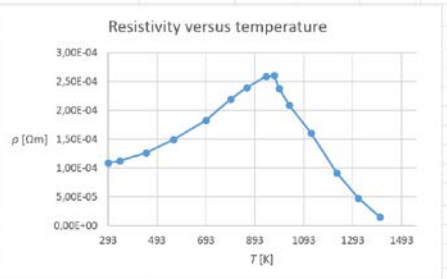

Figure 79. Resistivity table in the Electro-thermal model.

```
Sub Calc_I()
    Dim dT0    As Double
    Dim check1 As Boolean
    Dim check2 As Double
    Dim check3 As Double
    Dim n      As Integer

    Range("B34").Value = "Excel is solving."

    SolverReset

    For i = 0 To 39

      dT0 = Range("G3").Value
      SolverOk SetCell:="$B$23", MaxMinVal:=3, ValueOf:=0,
      ByChange:="$G$3", Engine:=1 _
      , EngineDesc:="GRG Nonlinear"
      SolverOptions Assumenonneg:=False
      SolverSolve UserFinish:=True

      check1 = IsNumeric(Range("B23"))
      check2 = Range("G3").Value

      If check1 = True And check2 > 0 Then

        check3 = Abs(Range("B23"))

        If check3 < 1 Then
            SolverFinish KeepFinal:=1
            Exit For
        Else
            SolverFinish KeepFinal:=2
            Range("G3").Value = dT0 * 0.99
        End If
      Else
        SolverFinish KeepFinal:=2

        If check2 < 0 Then
            Range("G3").Value = dT0 * 1.1
        Else
            Range("G3").Value = dT0 * 0.95
            End If
      End If

      Range("B33").Value = i

    Next i

    Range("B33").Value = i
    Range("B34").Value = "Solving done."

    If i > 39 Then
      MsgBox "Couldn't solve in 40 iterations" & Chr(10) & Chr(10) & "Try
      again or solve manually"
      End If
End Sub
```

Cell G3 is T'_1 and cell B23 is T''_n. The Solver in Excel often overestimates the initial value of the first derivative of the temperature at higher currents ($> 30\ \mathrm{mA}$). This overestimation causes the value of T''_n to be so large that it is too large for Excel to use it for calculation (overflow). If this is the case

the Macro discards the Solver solution and multiplies the earlier value with 1,1 or 0,95. The multiplication depends on the solution of the solver: if the Solver solution is numeric but negative (underestimation) it is required to multiply the earlier value by 1,1, if the Solver solution is numeric but positive (overestimation) it is required to multiply the earlier value by 0,95, these numbers are acquired by trial and error. By doing this T'_1 will converge to the right value, making it easier for the Solver to solve. This converge is limited to 40 iterations, because sometimes Excel cannot find a solution. If this is the case a message box will appear saying: "Couldn't solve in 40 iterations. Try again or solve manually." If trying again does not give a solution, T'_1 can be set manually, by trial and error, till T''_n is as closely to zero as possible. If the desirable value of T''_n is reached, the model outputs the resistance, voltage, power, average and maximum temperature, $\overline{\alpha \cdot \Delta T}$ and a graph of the temperature profile and resistivity profile, see figure 80.

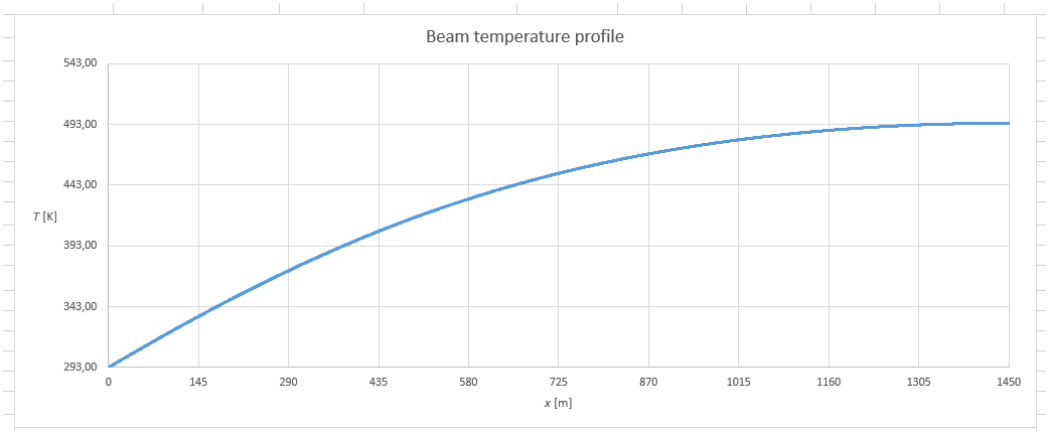

Figure 80. Beam temperature profile given by the Electro-thermal model at $I = 30$ mA.

G.3 Thermo-mechanical model

The transversal displacement of a beam can be calculated using analytic equation (2.23).

The variable input cells of the model are presented in figure 81. The dimensions and properties of the beam can be changed in the first two tables. In the "Input" table can the force acting on the beam be altered and can be chosen if only $\overline{\Delta T}$ is used as an input or $\overline{\alpha \cdot \Delta T}$, which can be extracted from the Electro-thermal model, by selecting the button behind the respective cell. If the button "Solve δ" is clicked, Excel calculates the value of k for which transcendental equation c (A.46) reaches zero as closely as possible. The following Macro is used for the calculation:

	A	B	C
1			
2	Dimensions		
3	θ [deg]	2	
4	h [m]	5,00E-05	
5	w [m]	2,41E-05	
6	L [m]	1,45E-03	
7	θ [rad]	0,034906585	
8	A [m^2]	1,21E-09	
9	I_{eff} [m^4]	1,89E-19	
10			
11	Properties		
12	E [Pa]	1,57E+11	
13	α [K^{-1}]	4,09E-06	
14	T_∞ [K]	293,15	
15			
16	Input		
17	F_v [N]	0,000000	
18	ΔT_{avg} [K]	500	○ ΔTavg
19	$(\alpha \cdot \Delta T)_{avg}$ [-]	2,23E-03	◉ (α·ΔT)avg
20			

	A	B
20		
21	Calculation	
22	k [m^{-1}]	1,59E+03
23	c [-]	4,14346E-12
24		
25	Tip displacement	
26	δ [µm]	48,16
27		
28		
29	Solve δ	
30		
31		

Figure 81. Input and output cells of the Thermo-mechanical model, in Excel.

```
Sub Solver_d__F()
    SolverOk SetCell:="$B$23", MaxMinVal:=3, ValueOf:=0, ByChange:="$B$22",
    Engine:=1, EngineDesc:="GRG Nonlinear"
    SolverSolve UserFinish:=True
End Sub
```

If the value of k is calculated by Excel, the tip displacement of the beam is calculated using equation (2.25) and shown in the "Tip displacement" table. After calculation the model also gives the shape of the beam, shown in figure 82.

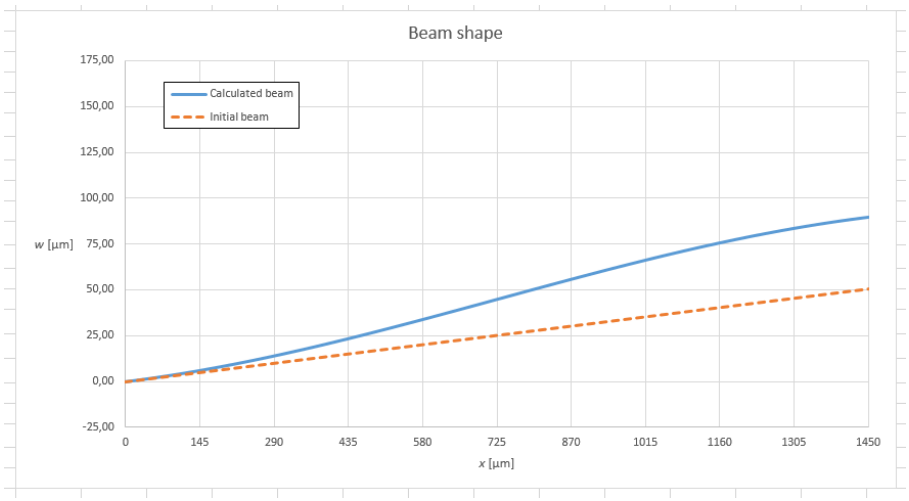

Figure 82. Beam shape given by the Thermo-mechanical model.